# Langevin model of low-energy fission

Arnold J. Sierk

Phys. Rev. C **96**, 034603 — Published 5 September 2017

DOI: 10.1103/PhysRevC.96.034603

# Langevin model of low-energy fission

Arnold J. Sierk
*Theoretical Division, Los Alamos National Laboratory,*
*Los Alamos, New Mexico 87545, USA*

(Dated: August 7, 2017)

**Background:** Since the earliest days of fission, stochastic models have been used to describe and model the process. For a quarter century, numerical solutions of Langevin equations have been used to model fission of highly excited nuclei, where microscopic potential-energy effects have been neglected.

**Purpose:** In this paper I present a Langevin model for the fission of nuclei with low to medium excitation energies, for which microscopic effects in the potential energy cannot be ignored.

**Method:** I solve Langevin equations in a five-dimensional space of nuclear deformations. The macroscopic-microscopic potential energy from a global nuclear structure model well benchmarked to nuclear masses is tabulated on a mesh of approximately $10^7$ points in this deformation space. The potential is defined continuously inside the mesh boundaries by use of a moving five-dimensional cubic spline approximation. Because of reflection symmetry, the effective mesh is nearly twice this size. For the inertia, I use a (possibly scaled) approximation to the inertia tensor defined by irrotational flow. A phenomenological dissipation tensor related to one-body dissipation is used. A normal-mode analysis of the dynamical system at the saddle point, and the assumption of quasi-equilibrium, provide distributions of initial conditions appropriate to low excitation energies, and is extended to model spontaneous fission. A dynamical model of post-scission fragment motion including dynamical deformations and separation allows the calculation of final mass and kinetic-energy distributions, along with other interesting quantities.

**Results:** The model makes quantitative predictions for fragment mass and kinetic-energy yields, some of which are very close to measured ones. Varying the energy of the incident neutron for induced fission allows the prediction of energy dependences of fragment yields and average kinetic energies. With a simple approximation for spontaneous fission starting conditions, quantitative predictions are made for some observables which are close to measurements.

**Conclusions:** This model is able to reproduce several mass and energy yield observables with a small number of physical parameters, some of which do not need to be varied after benchmarking to $^{235}$U(n,f) to predict results for other fissioning isotopes.

## I. INTRODUCTION

In the more than seventy-eight years since the recognition of the process of nuclear fission [1, 2], a comprehensive model for the process has not been presented. The scope of the difficulty may be seen by considering the array of output states which may be produced following thermal-neutron-induced fission of a fissile isotope such as $^{235}$U or $^{239}$Pu. From such an apparently simple initial state, characterized by known values of neutron number $N$, proton number $Z$, and excitation energy of the compound nucleus, several hundred different isotopes are produced, while each isotope pair identified may have a total kinetic energy (TKE) distributed over more than 30 MeV, and may emit from 0 to 5 or more prompt neutrons in the first $\approx 10^{-13}$ s after fission and will subsequently beta decay into a different array of fission-product isotopes, over time scales from milliseconds to years.

Considering the coupling between simple collective motion and various nuclear excited states, while realizing that the emission of neutrons from the fragments implies they are thermally excited, and considering dealing with a vast number of final states, leads to the conclusion that the nuclear collective motion must be dissipative. As Einstein showed for the case of Brownian motion [3], any dissipative force is necessarily accompanied by a fluctuating force. This was recognized very early, and by 1940 Kramers had presented a simple model of the effect of dissipation on fission lifetimes [4].

Once dynamical models of fission in the liquid-drop model were developed, first neglecting dissipation [5–7], followed by models incorporating dissipation, but only its damping contribution to the average motion [8, 9], studies appeared which followed up on the early work of Kramers, investigating the diffusive effects of dissipation (fluctuations) by studying solutions of the Fokker-Planck equation in the phase-space appropriate to one- or two-dimensional harmonic potentials [10–15].

It was soon realized that dealing with the multidimensional nature of fission is much more difficult if one tries to solve the Fokker-Planck equation in 2N-dimensional phase space, rather than using the Langevin equation in N-dimensional coordinate space [16]. While in principle equivalent, Langevin equations reduce the dimensionality of the dynamical system at the cost of requiring Monte-Carlo calculations with large numbers of trajectories to fully explore the diffusive nature of dissipation effects. Such calculations were begun by a number of

groups starting around 1985–1990 [17–20]. Three extensive review articles discuss the early history and some details of applying Langevin equations to nuclear scattering and fission of macroscopic nuclei [21–23]; they contain detailed discussions of the motivations and justifications for such an approach. These studies began considering the dynamics of fission with two-dimensional models of the nuclear shape [24–26]. Around 2000, three-dimensional Langevin equations began to be considered by various groups [27–29]. Later, some three-dimensional modeling was extended by including an additional angular orientation degree of freedom [30]. Except for Ref. [29] and similar work by the same group, all these investigations have exclusively used macroscopic or modified-liquid-drop potential energies. Very recently, one group has begun to model fission using the Langevin approach with microscopic potential-energy effects [31, 32]. These studies are so far limited to three shape coordinates, and to relatively high excitation energies, above the threshold for multiple-chance fission.

Not so implicitly, the foregoing discussion has assumed fission is a classical process, while obviously nuclei are quantum systems. But it is clear from the outset that it is impractical to calculate even the static properties of systems of more than 200 nucleons in a full quantum-mechanical approach, even if one actually knew the full details of the nuclear interactions to put into a Hamiltonian. So as is almost always the case in nuclear physics, one must select major simplifications of the underlying dynamics in order to explore a tractable model.

One route to model complex nuclei, which retains more of their quantum- mechanical nature, is to employ self-consistent mean-field theory or density-functional theory. Currently, these models comes in two basic flavors, either relativistic mean-field models (RMF), which usually employ meson and nucleon fields, or nucleon fields with point couplings. The other approach is to employ the non-relativistic Schroedinger equation, with effective two-nucleon potentials leading to a one-body effective potential, in the Hartree-Fock (HF) approximation, or to also include pairing effects via the Hartree-Fock-Bogoliubov (HFB) method. These approaches have the advantage that the macroscopic properties of the nuclear matter (volume and surface energies; diffuse surface, etc.) arise from the same effective-interaction parameters as are used to generate the mean-field central potential. While the RMF models also provide the spin-orbit interaction from the same parametrized fields or point couplings, the nonrelativistic approaches must employ an additional spin-orbit interaction whose strength involves additional parameters, while using a form factor defined by the gradient of the central mean field. The degree to which various features of real nuclei are suitably modeled depends upon both the assumed form of, and the parameters of the effective interaction. Beyond the simplifications needed for realistic modeling of static properties of heavy nuclei, there are a number of further approximations required to consider the dynamical aspects of fission. In any case, besides being much more calculationally intensive, to approach similar levels of reproduction of, for example global nuclear masses from these types of models requires a simiar number of parameters as does the macroscopic-microscopic approach described in the following paragraphs [33, 34].

In this paper I adopt a simpler approach based on the macroscopic-microscopic model of nuclear binding energy. This is a simplified mean-field model, whose single-particle potential is not self-consistent the way it is in microscopic mean-field models. The macroscopic properties of the nuclear matter are specified in one model, while the single-particle potential is defined by an independent set of parameters, with both being defined for the same nuclear shape. Microscopic corrections to the macroscopic model for the nuclear energy are calculated using the Strutinsky method [35], and an appropriate pairing model. This approach is many orders of magnitude faster to calculate than the microscopic self-consistent approaches, at the cost of being non-selfconsistent. The reproduction of the features of real nuclei depends upon both the parameters of the macroscopic model (volume, surface, and asymmetry energies, diffuseness of the charge and matter distribution, etc.) and the strength, diffuseness, and isospin dependence of the central and spin-orbit potentials, along with parameters of the pairing model used to calculate the microscopic energy corrections. Such approaches have achieved some success in modeling and predicting various static properties of nuclei, such as in global calculations of nuclear masses [34, 36, 37] and properties of fission barriers. [38–41]

The model I explore comprises a Monte-Carlo solution to five-dimensional Langevin equations for parameters describing the evolving shape of the nucleus during fission. The inertia is a scaled approximation to the irrotational inertia, the potential energy is calculated using a globally benchmarked macroscopic-microscopic model, the dissipation tensor is a scaled version of that for one-body dissipation, while the Langevin force is proportional to the square root of the product of the nuclear temperature and the dissipation tensor, and to the inverse square root of the time step used to integrate the stochastic differential equations. In order to avoid very long times spent randomly exploring local minima in the potential-energy surface, the starting conditions sample quasi-static equilibrium distributions near the outermost saddle point. This approach allows the modeling of distributions of fragment masses, total kinetic energies, the distribution of excitation between the fragments, and correlations among all calculated observables. Comparisons of calculated to observed distributions allow an assessment of the strengths and weaknesses of such a simplified modeling of the physics of fission.

The philosophy I adopt is to implement as simple a non-trivial model as possible, with sufficient degrees of freedom, a well-tested model for the nuclear potential energy as a function of shape, and very simple models for

the nuclear inertia, dissipation, and the thermal properties of nuclei. A comparison of predictions by the model to measured properties of fission distributions may allow an assessment of possible deficiencies and ways to improve various parts of the model.

Because it has been found that many pieces of the model need to be implemented carefully, I will outline all relevant parts of the model, so that important details are not obscured, and the approximations are clear.

The model is presented in Sec. II, with the physical parameters which are not well determined and allowed to vary discussed in Sec. III. Results are shown in Sec. IV with a discussion of the results, tentative conclusions from this preliminary study, and suggestions of possible paths forward in Sec. V.

## II. THE MODEL

The use of the Langevin equation to model fission has been implemented for a number of years [21–23, 31]. With one exception, these studies have used only macroscopic potential energies, and therefore have been applied mostly to systems formed in heavy-ion collisions with fairly high angular momenta and excitation energies, and have been limited to no more than three shape degrees of freedom [22, 28, 42, 43]. Recently a few studies have been done with an additional angular-orientation degree of freedom, but still with only a maximum of three shape degrees of freedom [30]. The one exception mentioned involves studies with a macroscopic-microscopic potential energy, still with only three shape degrees of freedom [31, 32].

This paper presents a study which differs from earlier ones in that five shape degrees of freedom are employed, and it uses a macroscopic-microscopic potential-energy model which has been benchmarked to masses, fission-barrier heights, and ground-state deformations over almost the entire nuclear chart. In addition, I study fission at low excitation energies, while all previous studies have been restricted to higher excitations.

The basic equations of motion for a classical dissipative system which include the fluctuating force necessarily accompanying damping forces are

$$\frac{dq_j}{dt} = \frac{\partial H}{\partial p_j} = \frac{\partial (K+V)}{\partial p_j} = \frac{\partial (\frac{1}{2} M^{-1}_{ik} p_i p_k)}{\partial p_j} = M^{-1}_{jk} p_k \tag{1}$$

$$\frac{dp_j}{dt} = -\frac{\partial V}{\partial q_j} + \frac{1}{2}\frac{\partial M_{kl}}{\partial q_j}\dot{q}_k\dot{q}_l - \eta_{jk}\dot{q}_k + \sqrt{\frac{2T}{\Delta t}}\gamma_{jk}\Theta_k(t). \tag{2}$$

In these equations, where here and in following equations I have assumed the summation convention for repeated indices, the coordinates $q_j$ describe the nuclear shape, $p_j = M_{jk}(q)\dot{q}_k$ is the conjugate momentum, H is the hamiltonian, V is the potential energy, K is the kinetic energy

$$K = \frac{1}{2} M_{jk}\dot{q}_j\dot{q}_k = \frac{1}{2} M^{-1}_{jk} p_j p_k,$$

$M$ is the inertia tensor, which depends upon the nuclear shape $q_i$, $\eta$ is the dissipation tensor, which is also shape dependent, $\gamma$ is the square root of $\eta$, T is the nuclear temperature, and $\Delta t$ is a single time step over which the equations are integrated. $\Theta_k(t)$ is a stochastic function satisfying $< \Theta_k(t) >= 0$, and $< \Theta_j(t)\Theta_k(t') >= \delta_{jk}\delta(t - t')$. $\Theta_j$ is found by use of a gaussian random number generator with unit variance. The rate at which energy is transferred (lost) from collective motion to internal (heat) energy is

$$\frac{dE_{\rm coll.}}{dt} = -\frac{1}{2}\eta_{jk}(q)\dot{q}_j\dot{q}_k.$$

Since by definition the dissipation tensor $\eta$ is positive definite, it is always possible to determine its square root, the tensor $\gamma$.

The assumptions which lead to the Langevin equations are discussed at length in [16, 21–23]. The momentum equation is often written in terms of the coordinate derivative of the inverse of the inertia tensor, but taking the gradient of the identity $MM^{-1} = I$, where $I$ is the identity matrix, leads to the form used here, which occurs with the opposite sign to the other form. One can easily calculate $\frac{\partial M}{\partial q}$ to much higher precision than $\frac{\partial M^{-1}}{\partial q}$, which helps to avoid problems with singularities in the inertia tensor when integrating the equations of motion. This form was pointed out by Feldmeier [21], but has very rarely been used in the extensive literature on macroscopic two- and three-parameter Langevin dynamical fission calculations which have followed his 1987 review.

I discuss the individual quantities in Eqs. 1,2 in the following subsections, followed by outlining the procedures used to determine distributions of starting conditions, and to integrate the Langevin equations.

### A. Shape coordinates

I have chosen to use the Nix three-quadratic-surface (3QS) shape parameters [7] as the coordinates for which the dynamical equations are to be solved. This choice reflects a number of considerations:

1. Extensive experience in solving deterministic dynamical equations using this shape description [7, 8, 44, 45],

2. Successful calculation and analysis of potential-energy surfaces in five shape dimensions [38–40, 46, 47].

3. The need to have a shape description with a minimum of five degrees of freedom in order to describe the most important shapes affecting the energy surface for systems approaching final binary break-up, and

4. The ability to span the range from compact (ground and isomer states) to intermediate (outer saddle point), and elongated (scission) shapes in a single shape description.

With respect to item number 3, since it has been known for a long time that the structure and ground-state masses of nuclei depend upon their deformation, it is clear that late in the fission process when the fragments are beginning to have clear identities, one needs to allow the fragments to separately have different deformations. Another important quantity is the distribution of mass between the fragments, followed by the size of the neck, and the total elongation of the shape. Thus, even before considering triaxiality, it is clear that five shape degrees of freedom are the minimum needed to try to quantitatively model the probability of various mass and kinetic energy distributions. Also, Randrup et al. [48], using a model which is similar to an infinite-dissipation limit of this approach, showed that trying to reduce the dimensionality to less than five using prescriptions previously touted as 'reasonable', causes the loss of fidelity of major properties of the results, such as an asymmetric fragment mass distributions with a width comparable to those seen experimentally. One might assert with some justification that five degrees of freedom may also be insufficient, since it is known that the inner saddle point in heavy actinides is unstable to axially asymmetric deformations. However, both for reasons of computational feasibility, and some indications that triaxiality is relatively unimportant in the region of the outer saddle point and beyond [49], I will only consider axially symmetric deformations in this initial study. This marks a significant increase of dimensionality over existing Langevin-equation dynamical fission modeling, heretofore limited to at most three shape degrees of freedom.

An alternative shape parametrization, an expansion of the surface described in cylindrical coordinates in Legendre polynomials of the scaled axial coordinate, satisfies these criteria [50, 51], but poses a great difficulty in efficiently defining an appropriate mesh, as is discussed more in II B. So although this shape description was considered carefully, and has decided advantages in not having some peculiar nonlinearities and singularities which occur for the 3QS, it turns out to be much harder to implement for dynamical studies. This is unfortunate, since in principle, a separate implementation of the model would allow a robustly quantitative discussion of the effects of constraining the shapes allowed.

In the 3QS parameterization, the shape of the nuclear surface is specified in terms of three smoothly-joined portions of quadratic surfaces of revolution. They are completely specified by [7]

$$\rho^2 = \begin{cases} {a_1}^2 - \dfrac{{a_1}^2}{{c_1}^2}(z-l_1)^2 \ , \ l_1 - c_1 \le z \le z_1 \\ {a_2}^2 - \dfrac{{a_2}^2}{{c_2}^2}(z-l_2)^2 \ , \ z_2 \le z \le l_2 + c_2 \\ {a_3}^2 - \dfrac{{a_3}^2}{{c_3}^2}(z-l_3)^2 \ , \ z_1 \le z \le z_2 \end{cases} \quad (3)$$

Here the left-hand spheroidal surface has the subscript 1, the right-hand spheroidal one 2 and the middle one, which may be a spheroid, a one-sheet hyperboloid, or a portion of a two-sheet hyperboloid, 3. For the end spheroids, the quantities $c_i$ are one-half the length of the spheroid along the symmetry axis and $a_i$ the maximum transverse extension of the $i$th spheroid. At the left and right intersections of the middle surface with the end surfaces the value of $z$ is $z_1$ and $z_2$, respectively. Surfaces 1 and 2 are also referred to as end bodies and, in the case of a well-developed neck, nascent fragments. When the center body is not a spheroid, for certain special cases the values of ${a_3}^2$, $c_3$, and $l_3$ diverge; for this reason, I utilize the equivalent form [52]

$$\rho^2 = \alpha + 2\beta z - \frac{{a_3}^2}{{c_3}^2}z^2 \ , z_1 \le z \le z_2 \quad (4)$$

There are nine numbers required to specify the expressions in Eq. (3) but the conditions of constancy of the volume and continuous first derivatives at $z_1$ and $z_2$ eliminate three of them. The introduction of an auxiliary unit of distance $u$ through

$$u = \left[\frac{1}{2}\left({a_1}^2 + {a_2}^2\right)\right]^{\frac{1}{2}} \quad (5)$$

permits a natural definition of two sets of shape coordinates. There are three symmetric coordinates $\sigma_i$ and three reflection-asymmetric coordinates $\alpha_i$, given by

$$\sigma_1 = \frac{(l_2 - l_1)}{u}$$

$$\sigma_2 = \frac{{a_3}^2}{{c_3}^2}$$

$$\sigma_3 = \frac{1}{2}\left(\frac{{a_1}^2}{{c_1}^2} + \frac{{a_2}^2}{{c_2}^2}\right)$$

$$\alpha_1 = \frac{1}{2}\frac{(l_1 + l_2)}{u}$$

$$\alpha_2 = \frac{({a_1}^2 - {a_2}^2)}{u^2}$$

$$\alpha_3 = \frac{{a_1}^2}{{c_1}^2} - \frac{{a_2}^2}{{c_2}^2} \quad (6)$$

The coordinate $\alpha_1$ is not independent, being determined implicitly by the requirement that the center of mass

remain at the origin, leaving five independent shape coordinates. This set of five coordinates will frequently be refered to with the notation $\{q_i\}$, where $i = 1, \ldots, 5$.

### B. Coordinate mesh

Since trajectories in a dynamical calculation can and will cover any point in a five-dimensional subspace, and because calculating microscopic energies and derivatives at any point encountered along a trajectory can become prohibitively time-consuming, it proves to be very efficient to define the energies on a mesh or grid in the five-dimensional space over which the nuclear system can evolve. This method was developed [38, 46] for analyzing the properties of multidimensional potential-energy surfaces.

With the potential energy and its gradient defined on an appropriate mesh, a suitable approximation to the values at any point not on the mesh may be found by employing a local five-dimensional spline approximation.

Because of the highly nonlinear connection of more physical quantities such as elongation, neck radius, etc. to the actual 3QS shape parameters, it proves valuable to define a five-dimensional mesh using auxiliary quantities more closely tied to physical properties of the shapes, such as nascent fragment deformations, the mass asymmetry of a shape with a well-defined neck, the radius or area of the neck, and an overall elongation of a nuclear shape. In general, the constraints on a mesh used for dynamical calculations are significantly more stringent than needed for static analyses. Because I need energy gradients, the continuity properties of the energy surfaces are of greater importance. The extent of the mesh needs to include all those shapes which there is a reasonable probability of reaching along a fission trajectory. In addition, it is highly desirable that there be no 'forbidden' or unphysical points inside the mesh boundaries, as occurs in the meshes employed in the static analyses of [38–40, 46]. There are also a number of regions where there is a perfectly well defined shape in the 3QS parametrization, but for which the inertia tensor can become singular.

I follow a procedure for defining a mesh closely following [40], but modify it as needed to satisfy the requirements outlined in the previous paragraph. I adopt the same definitions as in [38] for mesh coordinates $\epsilon_{f1}$, $\epsilon_{f2}$, and $\alpha_g$, corresponding respectively to the deformation of the left nascent fragment, the deformation of the right fragment, and the mesh asymmetry. Because of desiring a coordinate linear in the elongation for highly deformed shapes, which smoothly transitions to a fragment separation coordinate after scission, in lieu of the quadrupole moment used in [38], I employ a dimensionless elongation coordinate $R_1$ proportional to the separation of the centers of mass of the portions of the nucleus to the left and right of the neck. The fifth mesh coordinate is the ratio of the neck radius of a particular shape to the maximum neck radius possible for all shapes with the same values of $R_1$, $\varepsilon_{\rm f1}$, $\varepsilon_{\rm f2}$, and $\alpha_g$. These quantities are easy to visualize for shapes with a neck, but can also be generalized to shapes without necks. It is important to realize that as long as one chooses an arbitrary way to define a separator for shapes without necks, which smoothly becomes the neck location itself for shapes transitioning from a convex neck to a concave one, one can define the quantities of interest needed to generate the mesh. This complication, which has been dealt with in defining this mesh, will not be elaborated upon because is not relevant to the dynamical calculations to be presented, since the relevant fission dynamics always occurs outside the outermost saddle point, which for actinide and all lighter nuclei, always has a neck.

The mesh coordinates describing the deformations of the spheroids 1 and 2 of the 3QS shape parametrization are the Nilsson perturbed-spheroid $\epsilon_2$ parameters of each end body [53–55]: the shape of surface 1 by $\varepsilon_{\rm f1}$ and the shape of surface 2 by $\varepsilon_{\rm f2}$. The 3QS deformation parameters $\sigma_3$ and $\alpha_3$ are connected to $\varepsilon_{\rm f1}$ and $\varepsilon_{\rm f2}$ by

$$\sigma_3 = \frac{1}{2}\left[\left(\frac{3-2\varepsilon_{\rm f1}}{3+\varepsilon_{\rm f1}}\right)^2 + \left(\frac{3-2\varepsilon_{\rm f2}}{3+\varepsilon_{\rm f2}}\right)^2\right] \tag{7}$$

and

$$\alpha_3 = \left[\left(\frac{3-2\varepsilon_{\rm f1}}{3+\varepsilon_{\rm f1}}\right)^2 - \left(\frac{3-2\varepsilon_{\rm f2}}{3+\varepsilon_{\rm f2}}\right)^2\right] \tag{8}$$

In this work I use a larger range of $\varepsilon_{\rm f1}$ and $\varepsilon_{\rm f2}$ than employed in [38, 39] because of feedback from preliminary dynamical calculations which showed that dynamical fission trajectories tried to access more oblate end bodies than were needed for locating minima and saddle points on potential surfaces. I use 18 values of $\varepsilon_{\rm f1}$ and $\varepsilon_{\rm f2}$ with the values

$$\{-0.5, -0.4, -0.3, -0.2, -0.15, -0.1, 0.00, 0.1, 0.15, \\ 0.175, 0.2, 0.225, 0.25, 0.275, 0.3, 0.35, 0.4, 0.5\}. \tag{9}$$

For describing asymmetry, I use a 'grid' asymmetry, defined by

$$\alpha_{\rm g} = \frac{M_1 - M_2}{M_1 + M_2} \tag{10}$$

where $M_1$ and $M_2$ are the volumes inside the end-body spheroids,

$$\alpha_{\rm g} = \frac{a_1^2 c_1 - a_2^2 c_2}{a_1^2 c_1 + a_2^2 c_2}. \tag{11}$$

The 3QS parameter $\alpha_2$ is then completely determined by the relation

$$\alpha_2 = 2\,\frac{\left(\frac{(\,\alpha_{\rm g}+1\,)^2\,(\,2\,\sigma_3+\,\alpha_3\,)}{(\,\alpha_{\rm g}-1\,)^2\,(\,2\,\sigma_3-\,\alpha_3\,)}\right)^{1/3} - 1}{\left(\frac{(\,\alpha_{\rm g}+1\,)^2\,(\,2\,\sigma_3+\,\alpha_3\,)}{(\,\alpha_{\rm g}-1\,)^2\,(\,2\,\sigma_3-\,\alpha_3\,)}\right)^{1/3} + 1} \tag{12}$$

I have chosen a slightly different set of $\alpha_{\rm g}$ values than used previously because dynamical trajectories will encounter both positive and negative values of asymmetry, so the actual number of asymmetry points is almost doubled. I use the symmetry that a point with ($\alpha_{\rm g}$, $\varepsilon_{\rm f1}$, $\varepsilon_{\rm f2}$) has the same energy as a point with (-$\alpha_{\rm g}$, $\varepsilon_{\rm f2}$, $\varepsilon_{\rm f1}$). I use 36 values

$$\alpha_{\rm g} = 0.00(0.02)0.70, \tag{13}$$

and utilize the symmetry above to actually cover the range

$$\alpha_{\rm g} = -0.70(0.02)0.70, \tag{14}$$

In the following, I will define the size of the mesh by using the 36 distinct values of $\alpha_{\rm g}$, but utilize the symmetry to define a virtual mesh of nearly twice that size. It is important to stress that the exact definition of the asymmetry coordinate defining the mesh is not important, as long as it allows a complete coverage of the space of 'real' asymmetries which can only be unambiguously defined after the separation of the fragments or scission occurs.

For the elongation coordinate, I employ a coordinate with units of the radius of the spherical nucleus,

$$R_1 = R_2 - 0.75 \tag{15}$$

where

$$R_2 = \frac{< z >_r}{< z^0 >_r} - \frac{< z >_l}{< z^0 >_l}, \tag{16}$$

and $< z^n >_{l,r}$ is a mass moment of 'half' of the shape.

$$< z^n >_l = \int_{z_{\rm min}}^{l_3} z^n \rho^2(z) dz,$$

$$< z^n >_r = \int_{l_3}^{z_{\rm max}} z^n \rho^2(z) dz.$$

$z_{\rm min}$ and $z_{\rm max}$ refer to the leftmost and rightmost points on the shape, respectively. These expressions are strictly valid only for shapes with a well-defined neck. As mentioned earlier, the quantity $l_3$ may become undefined for compact shapes. It is possible to generalize the shape moment equations by replacing $l_3$ with the axial coordinate of a suitably defined plane of bisection for compact shapes. This is what was done for defining the mesh for small values of $R_1$, but the details are unimportant for modeling fission dynamics for the reason stated earlier. $R_1$ is defined as it is so that it is 0 for a spherical shape. Guided by preliminary dynamical calculations, I use for the mesh values of $R_1$ the 41 values

$$R_1 = 0.00, 0.10(0.05)0.90(0.10)3.20. \tag{17}$$

For the neck coordinate, I use the ratio of the neck radius to the difference between the minimum and maximum neck radii possible for a specified set of {$R_1$,$\varepsilon_{\rm f1}$, $\varepsilon_{\rm f2}$,$\alpha_{\rm g}$}.

$$d_{\rm n} = \frac{r_{\rm n} - r_{\rm min}}{r_{\rm max} - r_{\rm min}}, \tag{18}$$

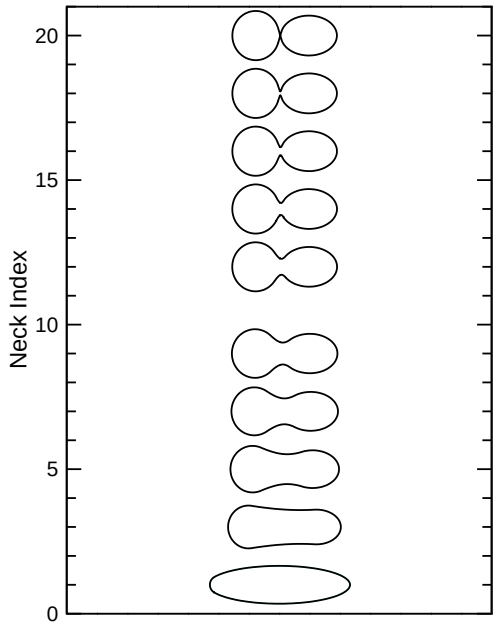


FIG. 1. A selection of shapes with different values of the neck coordinate index for shapes with $R_1 = 1.0$, $\varepsilon_{\rm f1} = -0.1$, $\varepsilon_{\rm f2} = 0.175$, and $\alpha_{\rm g} = 0.12$. The axis for each rotationally symmetric shape lies at the value of its neck coordinate index. The shape with neck index 14 lies near the bottom of the asymmetric fission valley for $^{236}$U, see Sec. II C 4.

where $r_{\rm max}$ and $r_{\rm min}$ are the maximum and minimum neck radii, respectively, possible for the specified values of the other four mesh coordinates, and $r_{\rm n}$ is the neck radius of the shape of interest. For shapes of sufficiently large $R_1$, $r_{\rm n} = a_3$, and $r_{\rm min} = 0$. I use for the mesh values of $d_{\rm n}$ the 20 values

$$d_{\rm n} = 0.00(\frac{1}{19})1.00. \tag{19}$$

In order to find specified values of $R_1$ and $d_{\rm n}$, it is necessary to iterate the values of $\sigma_1$ and $\sigma_2$ with the other three independent coordinates fixed, to achieve the desired values.

Figure 1 illustrates shapes for a selected range of neck-coordinate indices, for fixed values of $R_1$, $\varepsilon_{\rm f1}$, $\varepsilon_{\rm f2}$, and $\alpha_{\rm g}$.

The entire mesh over which I calculate the energy values and gradients contains $41 \times 20 \times 18 \times 18 \times 36 = 9,564,480$ points, which is roughly twice the size of the mesh used in [38–40]. The larger number of points reflects the need to include more oblate nascent fragments, and a closer spacing of the mesh in neck radii, demanded by the requirements of dynamical calculations. The decision on how many mesh points to use in eash dimension is made by considering preliminary dynamical calculations, and modifying the size as problems occur that may be resolved by refining the mesh.

### C. Potential energy

The potential energy is calculated in the macroscopic-microscopic model, specifically the FRLDM as defined in [34, 37], using the Wigner energy constants as defined in [47]. The actual shape-dependence of the Wigner energy is slightly modified, as discussed in the following paragraph. For the macroscopic energy calculations, I use expressions obtained from those in Appendix A of [51] by changing the definition of $\rho(z)$ to the 3QS model, and assuming axial symmetry. For z integrations, 128 gaussian quadrature points are used, while for the nuclear finite-range and the Coulomb-diffuseness energies, 16 $\phi$ integration points in the range [0,$\pi$] are used. The microscopic energy is calculated as outlined in [34, 37], with a slight modification of the definition of the deformed harmonic oscillator used to calculate the basis functions used in the Strutinsky procedure. This changed definition of the deformation of the harmonic oscillator defining the wavefunction basis gives more accurate calculations for elongated shapes like the bottom one in Fig. 1. In addition, a modified definition of the Strutinsky smoothing range more appropriate for large deformations than for the limited deformations of ground states is employed. This is discussed in more detail in Sec. III

Because of problems encountered in preliminary dynamical calculations for shapes where the neck just begins to appear, it is necessary to redefine the shape dependence of the Wigner energy. In Refs. [37, 47], the assumed shape dependence was defined as

$$B_{\rm W} = \begin{cases} \left(1 - \dfrac{S_3}{S_1}\right)^2 a_{\rm d} + 1 & , \quad \sigma_2 \le 0 \\ 1 & , \quad \sigma_2 \ge 0, \end{cases} \tag{20}$$

where $S_3$ is the area of the neck, $S_1$ is the area of the end body with the smaller maximum cross-sectional area, and $a_{\rm d}$ is a 'damping coefficient' whose value is 0.9 [37]. The problem arises because when $a_1^2$ becomes equal to $a_2^2$, especially when they are both close to $a_3^2$, this functional form has a discontinuity in some of its derivatives with respect to coordinates. The method used to estimate truncation error in the time integration of the Langevin equations does not 'like' discontinuous low-order derivatives. This problem was mitigated by slightly modifying the definition of the shape dependence of the Wigner and $A^0$ energies. The form chosen rather arbitrarily is

$$B_{\rm W} = \begin{cases} \left(1 - \dfrac{S_3}{S_{\rm av}}\right)^2 a_{\rm d} + 1 & , \quad \sigma_2 \le 0 \\ 1 & , \quad \sigma_2 \ge 0, \end{cases} \tag{21}$$

where

$$\frac{S_{\rm av}}{\pi} = \frac{a_2^2 - a_3^2}{D}\, a_1^2 + \frac{a_1^2 - a_3^2}{D}\, a_2^2$$

and

$$D = a_1^2 + a_2^2 - 2a_3^2.$$

This form gives the same limit as that in Eq. 20 when one of the end bodies is only slightly larger than the neck, and in the case when the two end bodies have the same maximum radius. There are deviations for intermediate values. With this form for the shape-dependence of the Wigner and $A^0$ energies, no further problems with dynamical integrations occur near where the neck first appears.

For the values of excitation energy encountered in low-energy induced fission and spontaneous fission discussed in this work, I assume that the potential energy is always that in the zero-temperature approximation. Generally, the average nuclear temperatures observed up to scission are well below 1 MeV. Some models of the thermodynamic properties of nuclear matter will support this approximation, and other models will suggest that one should use the proper free energy in place of the zero-temperature potential energy for such simulations. In the spirit of using the simplest assumptions possible, outlined previously, I retain this simplification, leaving it to later analysis to determine if there are quantitative indications this simplification needs to be abandoned.

#### 1. *Gradient of the potential energy*

The gradient of the macroscopic energy is calculated by numerical quadrature, again following the procedure outlined in [51]. Using a fairly ordinary Dell workstation running linux, it takes about 80 CPU hours to calculate the macroscopic energy and gradients for a single isotope over the entire mesh, while the microscopic energy takes about a CPU month, with the gradient of the microscopic energy about 10 times that long.

In principle, the gradient of the microscopic potential energy should be more efficiently calculated by utilizing the spline approximation discussed below to find the gradients in the mesh coordinates, then using a Jacobian transformation matrix to express the gradients in terms of the 3QS coordinates. The equations of motion are necessarily written in the 3QS coordinates because of the difficulty of precisely defining the inertia and dissipation tensors in terms of the mesh coordinates. Difficulties encountered in getting a calculation of the coordinate-transformation Jacobian tensor to converge for all points on the mesh led to the adoption of the less efficient expedient of separately calculating the five microscopic gradient components at each mesh point numerically. For large-scale calculations, it would be desirable to solve the problem of calculating an accurate Jacobian tensor, thus reducing the preliminary computational effort for any fissioning nuclide by a factor of 10.

#### 2. *Spline interpolation*

The trajectories which result from a Monte-Carlo solution of Eqs. 1, 2 can pass through any point inside the

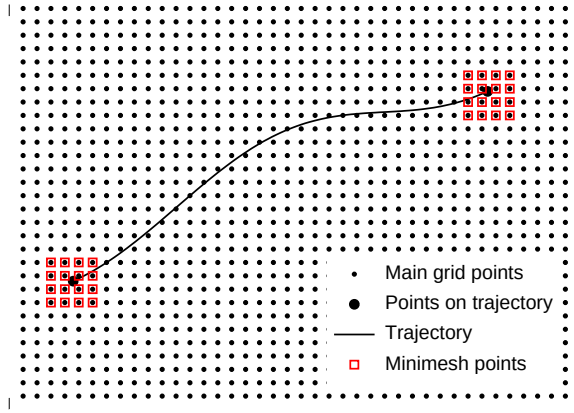


FIG. 2. (Color online.) A schematic representation of a dynamical trajectory in the space of mesh points, with minimeshes surrounding the initial and final points on the trajectory. Along the trajectory, every time a point is reached in the outer layer of hypercells in the minimesh, a new minimesh is defined, centered about the current trajectory point.

boundary hyperplanes of the five-dimensional mesh. For points in the neighborhood of any unit hypercell in the mesh, I define a local hypercubic spline on a minimesh of dimension $8 \times 8 \times 8 \times 8 \times 8$, extending three layers of hypercells around the current cell. It is straighforward to define a local five-dimensional cubic spline function for any quantity defined on the mesh, using standard basis-spline techniques [56, 57]. In principle, one could define a single spline approximation encompassing the entire mesh, but using the local minimesh leads to a much more manageable array of spline coefficients of size 32k words for each needed quantity. Such a small array size leads to more efficient use of memory in the computer simulations, leading to faster calculations.

Given a set of 3QS coordinates, it is straightforward to define the $R_1$, $\varepsilon_{\rm f1}$, $\varepsilon_{\rm f2}$, and $\alpha_{\rm g}$ mesh coordinates by using Eq. 15, and the inverses of Eqs. 7, 8, and 11. Similarly, the neck radius (for shapes with necks) is trivially $a_3$. The $d_{\rm n}$ coordinate is found by numerically iterating to find values of $\sigma_1$ and $\sigma_2$ which give the maximum and minimum neck radii possible for the other four mesh coordinates, using the same procedure as used to define the neck mesh in the first place. Then the neck mesh coordinate is found from Eq. 18.

The spline coefficients for a particular minimesh are used until the trajectory enters the outside layer of hypercells of the hypercube, at which point a new minimesh is defined, centered about the hypercell containing the current end of the trajectory. As a practical matter, the number of separate minimeshes which need to be defined for a single trajectory generally lie between about 15 and 40 for fission of $^{236}$U. A schematic picture of the moving spline approximation is illustrated in Fig. 2.

### 3. *Locating saddle points*

I use a version of the immersion algorithm [39, 46, 58, 59] to locate saddle points on a multidimensional surface. Discussion of the need to use non-local algorithms to locate saddle points, in contrast to the suitability of local methods to locate minima is given in Refs. [39, 59]. The immersion technique requires locating all local minima, including minima on the most elongated boundary hyperplane to define possible scission configurations. There can be a large number of such local minima, sometimes more than 150. By considering each possible pairing of all minima, one can define a saddle point separating each pair by use of immersion. Each higher minimum closer in energy to the saddle than a specified energy increment can be removed. Once all minima deeper than this nominal value (say 0.2–0.5 MeV) have been located, each pair is then considered separately with a more careful immersion calculation. A separate 'fluid' is introduced into each minimum, then the 'fluid' levels are raised together gradually until the 'fluids' have both wet at least one point in common. By repeating the process with finer and finer steps in the fluid level, one can locate the energy of the saddle point to any precision desired. In addition, the location of the saddle point can be determined to a single point on the mesh. This process can be refined by approximating the surface locally by a spline function, as discussed in Sec. II C 2. For a final refinement, instead of relying on the spline approximation to the energy surface, it is possible to search over sets of coordinates corresponding to spline approximations to their values on the mesh; thereby locating the set of coordinates with the minimum gradient vector.

As an example, for the $^{236}$U nucleus, with the energy values defined with respect to the macroscopic energy of a sphere, I find a deformed ground state at a potential energy of $-0.83$ MeV, a fission isomer state at about $-0.22$ MeV, and a third minimum of energy 1.55 MeV. The first saddle has an energy of about 3.31 MeV, while the second saddle has an energy of about 3.57 MeV, and the third saddle has an energy of about 2.40 MeV. This ground-state energy is really very crude, since the 3QS shape description does not allow as good a representation of the true ground state as other methods used to locate ground states in mass calculations [34, 37]. While the first saddle height is very close to the value of 3.39; the second saddle point is somewhat lower than that of 3.97 derived from the barrier heights tabulated in [39], after correcting for the ground-state energy of $-1.06$ MeV [34]. The earlier calculations used the old value of $1.0 B_{\rm S} \hbar\omega$ for the Strutinsky smoothing range (See Sec. III 1), the original Wigner-energy shape-dependence of Eq. 20, and also used a different coordinate mesh than that used here.

#### 4. Defining valleys and ridges

It has been shown empirically that defining all fission 'valleys' in the potential-energy surface has significant value [38, 39, 60]. This is so despite the general knowledge that 'valleys' in a multi-dimensional surface may be transformed out of existence by certain coordinate transformations [61]. But in the case where the chosen coordinates bear some relation to actual physical quantities, these 'valleys' can have real significance. This is one of many reasons for the choice of the $R_1, d_n, \varepsilon_{f1}, \varepsilon_{f2}, \alpha_g$ coordinates, where these coordinates bear some direct relationship to actual important physical properties of the shapes, in contrast to what would occur if one were to choose the 3QS coordinates to define the mesh directly.

I choose to define a valley as the locus of points found by locating local minima in the four-dimensional subspaces defined by fixing the value of $R_1$. It turns out that the valleys defined in this way are very similar to those defined in terms of subspaces of fixed quadrupole moment [38, 60]. Operationally, one locates all local minima, then discards all such minima separated from another minimum by a saddle of height less than some threshold, say 0.5 MeV, for example, entirely as was done in the original five-dimensional space to define significant local minima. After finding these surviving minima, one defines a valley by connecting minima with adjacent values of $R_1$ which have similar values of the other four coordinates. I discard any local minimum which does not have at least two points of similar character for adjacent $R_1$ values as not being important. For actinide nuclei, one finds that there are a small number of valleys, often only two or three. These valleys have a close identification with properties of the observed mass distributions of fission at low excitation energies [38]. In this part of the nuclear chart, there is almost always a valley with nearly or total mass symmetry, and a valley with a mass asymmetry close to the average mass split observed in asymmetric fission. It is interesting that this asymmetric valley arises out of the microscopic part of the potential energy, all of whose parameters were determined solely by considering level ordering and quantum numbers of states near both spherical and deformed ground states [62]. No fission observables of any kind enter into determining the microscopic potential. Nevertheless, the approximate mass-split seen in low-energy actinide fission arises from doing this simple analysis of valleys in the potential-energy surface [38].

Once valleys have been found, it is straightforward to define 'ridges' which separate distinct valleys, by use of immersion to define saddle points in the constant-$R_1$ subspaces. These are then identified as ridges in the full space. Among the many nonintuitive features of potential surfaces in more than two dimensions, one frequently finds that a ridge separating a symmetric valley from an asymmetric valley may have an asymmetry larger than that of the asymmetric valley, something which is topologically impossible in two dimensions.

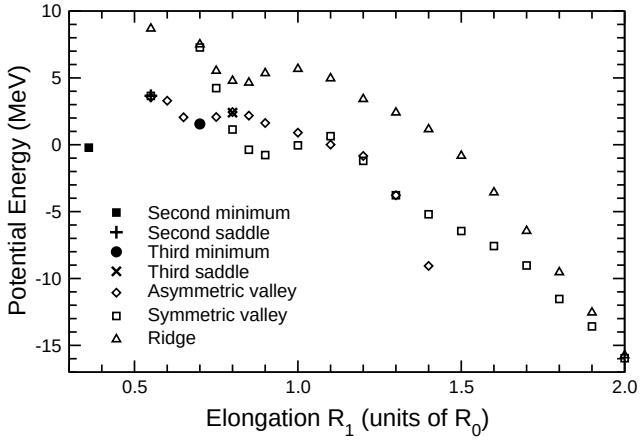


FIG. 3. The calculated energies of the second and third minima, the two outermost saddle points, the mass-symmetric and mass-asymmetric valleys, and the ridge between them as functions of the coordinate $R_1$ for $^{236}$U.

I illustrate the energies of the second and third minima, the two outermost saddle points, the symmetric and the asymmetric valleys, and the ridge between them for $^{236}$U in Fig. 3. The shapes of these four equilibrium points shown in this figure are shown in Fig. 8 of Ref. [60] The last point shown on the asymmetric valley has a zero neck radius, whereas the last point shown on the symmetric valley, at an energy near -16 Mev retains a neck radius of about 1.8 fm. The symmetric valley persists with a finite neck radius to elongations much larger than the asymmetric valley. Although the energy of the symmetric valley for $R_1 = 0.8$ is less than that of the asymmetric valley, which is essentially the same as the energy of the third saddle point, and drops farther below the energy of the asymmetric valley just outside the third saddle, it is well separated from the asymmetric valley in coordinate space, and thus is not easily reached due to the high ridge between the valleys. This is discussed further in Section IV.

### D. Inertia tensor

There is a very long history of attempts to model the nuclear inertia for various types of motion. Some examples are modeling the energies of vibrational $2^+$ states by use of a cranking model, calculating spontaneous fission lifetimes by calculating penetrabilities using a number of approximations for the nuclear mass, and many other ways of trying to estimate the matter currents for various types of assumed motion of the nuclear surface.

In the spirit of trying the simplest nontrivial models for the various terms in Eqs. 1,2, and the success achieved in the past in modeling average fission-fragment kinetic energies with simple fluid models for inertias (see Sec. III 4), I use the Werner-Wheeler approximation to ir-

rotational flow [7, 8, 51, 63]. In addition to being the minimum possible inertia for a particular type of surface motion, this simple model has been extensively applied in most earlier dynamical and Langevin simulations [7–9, 21, 25, 27, 28, 44, 64, 65]. In order to investigate the effect of using a larger inertia, I will consider multiplying this limiting value with a possible scaling factor (see Sec. III 3). This scaling is the simplest possible, being the same for all inertia tensor elements. It is easy to think of more realistic models which involve scaling different modes differently, but this will remain something to be investigated in the future. It is obvious that late in the fission process, the inertia corresponding to the separation of the fragments will approach the reduced mass, while the inertia of the fragment deformations might have a larger scale factor more characteristic of simple models for beta vibrational states. Such a model is beyond what I attempt in this preliminary study.

The expressions used to find the Werner-Wheeler inertia are given in Appendix A of [8]; the gradients of the inertia are found by differentiating Eq. (A9) of that reference with respect to the $q_i$, and employing appropriate coordinate derivatives of Eqs. (A13a) and (A13b). The integrals defining the $A_i$ coefficients and their gradients are performed analytically, and those for the inertia itself by applying a Gauss-Legendre quadrature formula with 128 abscissa points. The quadrature is broken into four parts, in order to avoid integrating over points of discontinuities in higher-order derivatives. The intervals in $z$ of the integration are (for shapes with necks) $[l_1 - c_1, z_1]$, $[z_1, l_3]$, $[l_3, z_2]$, and $[z_2, l_2 + c_2]$, with each interval approximated by a numerical quadrature with 32 abscissas. Nix [52] presented analytic forms for the inertia tensor elements utilizing the original form for the middle body given in Eq. 3. Similar analytic expressions for the inertia tensor using the alternative form for the middle body, Eq. 4, have been derived, but through extensive testing it has been demonstrated that equivalent accuracy and speed of calculation are achieved by use of the numerical quadrature formulas, with the use of algebraicly much simpler expressions. The analytic forms derived for this alternative shape function require careful analysis of various limiting cases for the values of the parameters $\alpha$, $\beta$, and $\sigma_2$. The numerical approach is much simpler.

### E. Dissipation tensor

The earliest dynamical calculations of fission including dissipation started from the minimal assumption of extending the liquid-drop model to consider the shear viscosity of a simple fluid [8, 66]. With such a simple assumption for the nature of dissipation, it was found that dissipation led to more elongated shapes for fissioning nuclei than was the case for non-dissipative motion. This is due to the increase in damping associated with higher shape multipoles for shear viscosity. The calculations of fragment kinetic energies compared to data implied a motion which was significantly dissipative, but underdamped.

Even at that time it was realized that individual nucleons have a long effective mean-free path inside nuclei, primarily due to the Pauli exclusion principle. This long mean-free path is the reason for the success of the shell model in describing nuclear structure. It is an irony of history that for over a decade starting in the 1930's most serious nuclear physicists felt that a shell model was impossible for nuclei because of the very large cross sections of free nucleons; such large cross sections implying very short mean-free paths. Only after the success of applying the shell model to nuclear structure was the effect of the Pauli principle understood to contribute to a much longer effective mean-free path than the free n-n cross section would imply.

#### *1. The wall formula*

In the 1970's the awareness of the shell model led almost immediately to consideration of models for nuclear dissipation which emphasized the one-body nature of nucleonic motion in a mean field, as opposed to the shear viscosity which is valid for constituents with very short mean-free paths. The first concrete model based on one-body dynamics, which involved several simplifying assumptions, was the so-called wall-formula dissipation [9]. In this model, the movement of the surface of the nuclear potential (the 'wall') couples energy from the motion of the wall into the average velocities of the nucleons colliding with the wall. These nucleons were assumed to be free-streaming particles occupying a Fermi sphere in momentum space, interacting only with the surface of the mean-field potential, which could be moving with respect to the average velocity of all the nucleons. The wall-formula energy dissipation rate is then proportional to the surface integral of the square of the normal velocity of the nuclear surface with respect to the average velocity of the nucleons,

$$\left.\frac{\mathrm{d}E}{\mathrm{d}t}\right]_{\mathrm{wall}} = \rho\langle v\rangle \oint v_{\mathrm{n}}^2 dS. \tag{22}$$

For a simple zero-temperature Fermi gas, $\langle v\rangle = \frac{3}{4}v_{\mathrm{F}}$, where $v_{\mathrm{F}}$ is the Fermi velocity and $\rho$ is the mass density of the nucleons.

If the Fermi velocity of nucleons at normal nuclear density is used, this dissipation model leads to very overdamped motion. In addition, the tensorial nature of wall-formula dissipation leads to less elongation of fissioning nuclei than is the case for non-dissipative motion. This is due to a relative decrease of wall damping with multipole order, in contrast to the opposite behavior for two-body shear viscosity. In the initial studies of the wall formula, it looked like the data on fragment kinetic energies could be explained by such highly overdamped motion also, because the lack of the prescission kinetic energy which

had occured in the two-body dissipation calculations, was compensated for by the increased Coulomb energy of the fragments when they fly apart from the less elongated scission shapes [9].

### 2. The window formula

Another type of one-body dissipation may be thought of classically as the ballistic transport of momentum from one part of a nuclear shape to another [9]. A simple example would be two nuclei suffering a peripheral collision, but getting close enough together that their surfaces partly merge, lowering the mean field in a small region; that is, opening a 'window' between the two nuclei. If nucleons randomly pass through the window, they will have an average velocity characteristic of their original 'home' nucleus, which is generally different from that of the 'new home' nucleus. Thus the average velocity of nucleons in the recipient nucleus will be changed. This rate of momentum change behaves like a dissipative force acting on the relative velocity of the two nuclei [9]. A number of calculations of damping in heavy-ion collisions and the transport of angular momentum between collision partners have been performed utilizing the window-dissipation model. A similar consideration of nascent fission fragments in the late stages of fission suggests there is a slowing down of the relative motion of the two fragments, again due to the random transport of nucleons from one nucleus to the other through a narrow neck between them. This dissipative force has been named 'window' dissipation. If one specializes to the case of two nuclei (fragments) with no angular momentum moving either together or apart only along a line connecting their centers, the window dissipation is [9]

$$\left.\frac{\mathrm{d}E}{\mathrm{d}t}\right]_{\mathrm{window}} = \frac{1}{2}\rho\langle v\rangle\Delta\sigma\dot{R}^2 \qquad (23)$$

where $\dot{R}$ is the rate of change of the distance of separation between the mass centers of the fragments and $\Delta\sigma$ is the area of the window.

### 3. Wall-and-window dissipation

After recognizing that the wall dissipation was appropriate for a single nucleus, and the window dissipation along with wall dissipation independently inside each of two almost separated nuclei, a combination of the two models was introduced [44]. This model originally had an abrupt transition between the two models at a specified neck radius, but was relatively quickly slightly modified in [67] to effect a smooth transition between the pure wall and the wall-and-window dissipation. To lead to the proper limits, a simple ansatz was used. For nuclei having no neck, the pure wall formula is used; for separated nuclei, the window dissipation for the separation coordinate, and the wall dissipation applied to each fragment separately, where the normal velocity employed is with respect to that of the individual fragment or nucleus, and not to the average velocity of the total system. For shapes between the formation of a neck and scission, a linear combination of the two dissipation mechanisms was used.

$$\left.\frac{\mathrm{d}E}{\mathrm{d}t}\right]_{\mathrm{W+W}} = \tau\left.\frac{\mathrm{d}E}{\mathrm{d}t}\right]_{\mathrm{wall+wind}} + (1-\tau)\left.\frac{\mathrm{d}E}{\mathrm{d}t}\right]_{\mathrm{wall}}, \qquad (24)$$

where

$$\left.\frac{\mathrm{d}E}{\mathrm{d}t}\right]_{\mathrm{wall+wind}} = \rho\langle v\rangle\left[\frac{1}{2}\Delta\sigma\dot{R}^2 + \oint v_{\mathrm{n,L}}^2 dS_L + \oint v_{\mathrm{n,R}}^2 dS_R\right],$$

$$v_{\mathrm{n,L}} = \hat{n}_{\mathrm{L}}\cdot(\vec{v}_{\mathrm{wall}} - \vec{v}_{\mathrm{D,L}}),$$

$\hat{n}_{\mathrm{L}}$ is the outward normal to the surface of the left nascent fragment, $\vec{v}_{\mathrm{D,L}}$ is the drift velocity of the left fragment, with similar definitions holding for the right-fragment quantities $\hat{n}_{\mathrm{R}}$, $\vec{v}_{\mathrm{n,R}}$, and $\vec{v}_{\mathrm{D,R}}$. This drift velocity was approximated as the velocity of the mass center of the appropriate fragment in the earliest implementation of the model, but soon replaced by the 'force-free' drift velocity, defined so that the net force along the axis of separation on the left or right fragment due to collisions of the nucleons initially inside that fragment is zero. The interpolation factor $\tau$ is arbitrarily defined to smoothly transition between the pure wall dissipation for shapes without necks and the pure window for the separation, and pure wall inside each fragment for fragments from scission outwards.

$$\tau = cos^2(\pi[S_{\mathrm{min}}/S_{\mathrm{max}}]/2),$$

where $S_{\mathrm{min}}$ is the area of the neck, and $S_{\mathrm{max}}$ is the lesser of the maximum areas of the left and right fragments. For shapes with no neck, $\tau = 0$, and for separated fragments, $\tau = 1$.

### 4. Surface-plus-window dissipation

Right from the introduction of the extreme one-body or wall dissipation model, it was realized that the high dissipation rate depended upon the 'randomization hypothesis' [9]; that is, that the average velocity or momentum of the nucleons that collide with the wall at a particular moment are distributed in a Fermi sphere in momentum space characteristic of an equilibrium distribution with no net velocity along the normal to the wall. This randomization might occur for a classical system if the shape of the nuclear mean field (container) is sufficiently irregular, or if some residual two-body interactions would quickly lead to some isotropization of a distorted Fermi surface caused by earlier wall collisions.

Indeed, the result that the wall collisions lead to dissipation depends upon the relative phases of the distortions of the container and the Fermi surface. A simple model of the isoscalar giant quadrupole and octupole resonances which accurately predicts the mass number dependence of the energy of these resonances results from simply assuming that these distortions have a specific phase relationship for harmonic motion [68, 69]. The restoring force in this model has exactly the same magnitude as does the dissipative force in the wall formula, which assumes that the surface and Fermi surface are out of phase for harmonic motion. Semiclassical and quantum models both give a great reduction in the dissipation for small-amplitude quadrupole motion [70–72], demonstating that the randomization hypothesis fails for highly symmetric deformations.

The reason for preferring a one-body dissipation model is the observation described in Sec. II E 1 that the mean free path of nucleons near the Fermi energy is relatively long. This is due to the Pauli exclusion principle forbidding scattering into already occupied states. Recognizing that the Pauli principle depends upon the density, one must conclude that this inhibition on collisions must go away in the surface of the nucleus as the density decreases towards zero [73]. Heuristically, the probability of two-body collisions must involve a convolution of the density with the inverse of the mean free path. One may conclude that it is plausible to infer that the two-body collision rate peaks in the surface region. Starting only from the assumption that dissipation from either source is concentrated in the nuclear surface region, it is possible to approximate the dissipation rate as an expansion in powers of the ratio of the surface diffuseness to the nuclear radius [74]. The leading term of this expansion has exactly the same form as the wall dissipation, but with a coefficient involving the probability of two-body collisions near the nuclear surface, instead of just the Fermi velocity.

The unknown reduction of the strength of the wall dissipation due to possible distortions of the Fermi surface and the similar functional form for two-body collsions concentrated in the nuclear surface led to the postulation of the surface dissipation model [45, 75–78].

$$\left.\frac{\mathrm{d}E}{\mathrm{d}t}\right]_{\mathrm{surface}} = k_{\mathrm{s}}\rho\langle v\rangle \oint v_{\mathrm{n}}^2 dS \tag{25}$$

Ignorance of the details of the two contributions leads to the simplest possible modification of the window dissipation model, the introduction of the empirical parameter $k_{\mathrm{s}}$.

By combining the surface dissipation model with the window dissipation, which, since it involves momentum transfer between nascent fragments or colliding nuclei, should not be renormalized, leads to the surface-plus-window (SPW) dissipation model

$$\left.\frac{\mathrm{d}E}{\mathrm{d}t}\right]_{\mathrm{spw}} = \tau\rho\langle v\rangle\left[\frac{1}{2}\Delta\sigma\dot{R}^2 + k_{\mathrm{s}}\oint v_{\mathrm{n,L}}^2 dS_L + k_{\mathrm{s}}\oint v_{\mathrm{n,R}}^2 dS_R\right] + (1-\tau)\left.\frac{\mathrm{d}E}{\mathrm{d}t}\right]_{\mathrm{surface}}, \tag{26}$$

where the quantities other than $k_{\mathrm{s}}$ are exactly as defined following Eq. 24.

The SPW dissipation model was developed in 1985, but was not published outside of some relatively inaccessible conference proceedings [45, 75–78]. Despite its lack of wide dissemination, this dissipation model has been implemented by other authors [23, 65, 79–81].

It turns out that fission-fragment total kinetic energies (TKE) do not clearly distinguish among $k_{\mathrm{s}}$ values in the range 0.2–0.5 [45], although it is clear that the data are inconsistent with the original wall-and-window model ($k_{\mathrm{s}} = 1$) [15]. Because of an earlier unsuccessful attempt to relate observed widths of isoscalar giant multipole resonances to any existing dissipation models [68, 69], it was decided to see what would be the consequences of assuming that the mechanism of nuclear dissipation was universal, applying equally well to the isoscalar giant multipole resonances, which can be thought as incompressible vibrations about the ground-state shape of a nucleus, as to the much slower motions characteristic of fission. There may be many theoretical objections to this assumption of a simple constant characterizing dissipation, independent of multipole order, elongation, and temperature, but in the same spirit in which the irrotational inertia is used, this simple ansatz for the dissipation mechanism is adopted to learn how it may be consistent with, or contradicted by, measurements. By applying the surface dissipation model to the measured widths of the isoscalar giant quadrupole and octupole resonances, an empirical value of $k_{\mathrm{s}} = 0.27$ was deduced. The comparison of the simple model of oscillations about a sphere is compared to the data in Fig. 4. Although not perfect, this relatively close reproduction of the data is to be compared to that for other dissipation models displayed in Refs. [68, 69].

With the dissipation strength fixed in this manner, the same model was applied to fission. At the time, it was not feasible to calculate large numbers of trajectories for a Langevin equation, so only mean-value trajectories were calculated using essentially equations 1 and 2 with both the stochastic term and the microscopic contribution to the energy surface ignored. For these calculations, the axial Legendre polynomial shape parametrization, with 8 symmetric shape parameters was used [15, 50]. It was later determined that the results found using the 3QS shape parametrization are very close to those shown. In order to get a more accurate estimate of the final TKE, after scission the fragments were approximated as deformable coaxial spheroids, as outlined in Sec. II H [8]. The resulting TKE values are plotted as a function of $Z^2/A^{1/3}$ in Fig. 5. The 1985 Viola systematics [84] are also shown in the figure. The Viola two-parameter fit,

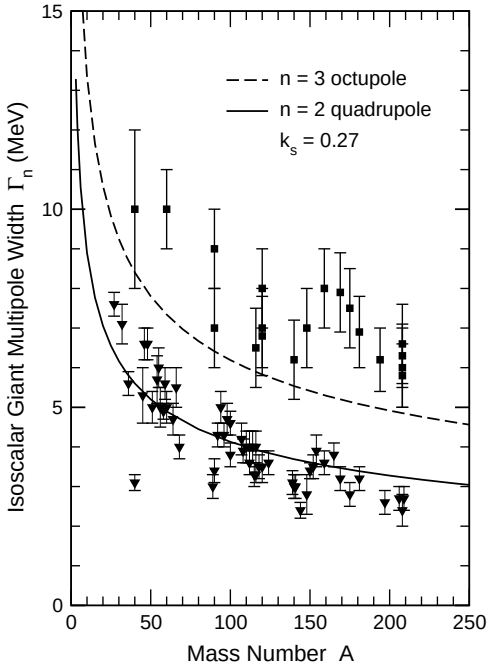


FIG. 4. Isoscalar giant quadrupole and octupole widths used in 1985 to fix the strength $k_s$ of the surface dissipation. The width data are from Refs. [82, 83].

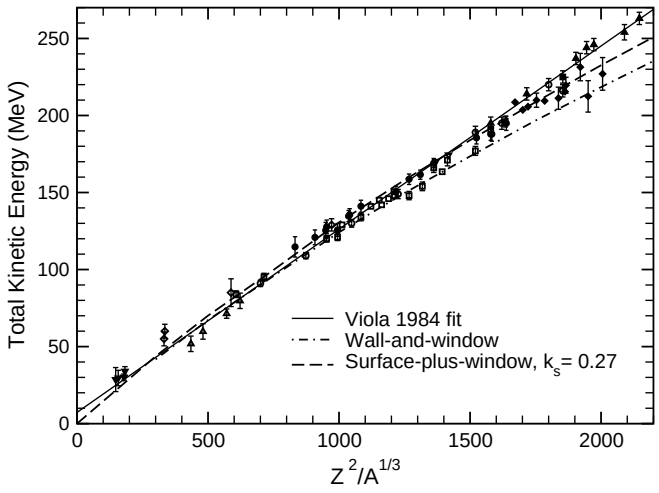


FIG. 5. Data on symmetric or average fission-fragment kinetic energies for highly excited systems compared to the 1985 Viola two-parameter fitted systematics and to the predictions of both the wall-and-window and the surface-plus-window dissipation models with a purely macroscopic potential energy. The data are from: 1, solid circles from Ref. [89], corrected in [90], 2, solid square from Ref. [91], 3, downward-pointing solid triangles from Ref. [92], 4, upward-pointing solid triangles from Ref. [93]. 5, solid diamonds from Ref. [94], 6, open circles from Ref. [95], 7, open squares from Refs. [96–98], tabulated in [90], 8, open upward-pointing triangles from Ref. [99], 9, open downward-pointing triangles from Ref. [100], and 10, open diamonds from Ref. [101].

determined by comparison to a data set with about an 85% overlap with the one plotted here, has a $\chi^2$ per point of 3.1. The SPW model calculations shown, which have not been adjusted to the data, have a $\chi^2$ per point of 3.6. The wall-and-window dissipation model gives a $\chi^2$ per point of 7.7. Because of this success of the model, the surface-plus-window dissipation model is adopted as the starting point for the fission simulations described below.

Some might object to the assumption of dissipation being independent of the excitation energy and having a relatively mild dependence upon the deformation of the nucleus, just given by its definition by means of a surface integral (Eqs. 25,26). Many authors have used data to infer large increases of dissipation strength with excitation energy or temperature [85–87]. The study by Lestone and McCalla [88] convincingly demonstrates that most, if not all, such strong increases in inferred dissipation are artifacts of the use of a statistical decay model which neglects certain known physical effects. Thus, in the spirit of choosing the simplest possible non-trivial model with few arbitrary constants, I will use this simple dissipation model and allow the confrontation with data to determine whether there is a need for more sophisticated treatments.

### F. Nuclear temperature

Following the minimally complicated path already described, I choose a simple quadratic dependence of nuclear excitation energy on temperature:

$$E^* = a_{\rm th} T^2, \tag{27}$$

where $a_{\rm th} = A/8.6$ MeV$^{-1}$. The excitation energy $E^*$ is defined locally as the difference between the initial total energy of the nucleus and the sum of the kinetic and potential energies. To avoid numerical problems with very small or slightly negative values of $E^*$, the temperature has a lower limit of $T_{\rm c} = 0.002$ MeV.

### G. Solving the Langevin equations

Equations 1 and 2 may be combined and solved as 10 first order stochastic differential equations for the variables $q_i$ and $p_i$. There are detailed discussions of solution methods in the review articles [22, 23]. Stochastic differential equations pose some difficulties as compared to the ordinary differential equations used for deterministic trajectories. For the latter, predictor-corrector methods have been very successful, as judged by applying an energy-conservation test to the results. The random force, which in principle is different at each time step, makes such algorithms useless. But it turns out that the stochastic equations may be integrated by assuming a constant random force over the time step, provided the time step is short enough that the momenta and coordinates do not undergo a large change during the short time. It is always possible to find such a step, since the change in q or p over the step is proportional to $\Delta t$, while the size of the random force is proportional to $(\Delta t)^{-1/2}$.

Because of the highly nonlinear nature of both the coordinates and the dissipation and inertia tensors, it is highly inefficient to adopt a single time step which will guarantee an accurate solution of the equations. Instead, I use an adaptive step size based upon a Runge-Kutta algorithm with a truncation error estimate in each step [102]. The random force is fixed at the beginning of the time step, and an approximate solution at the end of the step, along with a truncation error estimate are determined. When the relative truncation error is below $10^{-4}$, the step is accepted, and a new random force is calculated for the next step. If the error is too large, the step size is halved, but the random force vector is retained, but multiplied by $\sqrt{2}$. At the end of this reduced step, a new random force is used for the second half of the original step. When the relative error gets very small, the step size is doubled for subsequent steps, up to a maximum step, for which I have chosen the value of $2.5 \times 10^{-23}$ s.

### 1. *Starting conditions for induced fission*

To approach as closely as possible the experimental situation of an excited compound nucleus created by the absorption of a neutron, ideally one would start the system out with an equilibrium distribution of coordinates around the ground-state minimum, with a distribution of momenta whose average magnitudes would reflect an excitation energy of the sum of the neutron kinetic energy and the one-neutron separation energy of the compound system. Because the characteristic time scale of low-multipole shape oscillations in the ground-state minimum is of the order of $10^{-21}$ s, and the fission lifetime for thermal-neutron induced fission of, for example, $^{235}$U or $^{239}$Pu is roughly of the order of $10^{-15}$ s, it is not feasible to run simulations of roughly $10^8$ time steps to observe a single fission. In addition to this obvious difficulty, the difficulty of describing shapes in the neighborhood of the ground state in the 3QS shape parametrization causes singularities which make such a simulation doubly impractical.

I have verified, using a simplified dynamical macroscopic model, in which the microscopic correction energy is ignored, and the shapes are described in 4-, 6-, or 8-parameter axial Legendre polynomial shapes [50], that these systems at much higher excitation energies will fission with a time scale similar to that estimated from simple statistical arguments [88]. In addition, this simplified model exhibits the expected equipartition of energy in kinetic and potential energy in the collective normal modes, characterized by the appropriate temperature for a given excitation energy. This test verifies that the basic equations and solution techniques give the appropriate limiting distributions at long times.

The practical solution to this difficulty of dealing with very long times to reach fission is to recognize the power of the transition-state approach. Those trajectories that do lead to fission will be in quasi-equilibrium as they pass over (or near) the fission saddle point, the configuration with the largest available phase space of any configuration leading to fission. Because the gradient of the potential energy is by definition zero at the fission saddle point, it is possible to perform a normal-mode analysis of the dynamical system at the saddle [7]. Such an analysis leads to five uncoupled normal modes, four with positive squared frequencies and one with a negative squared frequency. The latter is the fission mode, which will grow exponentially for any small displacement away from the saddle point. For a non-dissipative model in thermal equilibrium, the distributions of the coordinate displacements with respect to the saddle point and the momenta are gaussian functions centered at zero, with widths proportional to the square root of the temperature [7]. Since the actual systems I am modeling are dissipative, the normal-mode problem becomes slightly changed. As outlined in Ref. [103], the dissipative normal-mode solution leads to 2N normal modes, where N is the dimensionality of the system; in this case N = 5. For moderate dissipation values, as in the SPW model, the unstable fission mode becomes an exponentially damped inertial mode which is not relevant for fission, and an exponentially growing mode driven by the potential. The other modes may split into paired damped-harmonic-oscillator modes with complex-conjugate frequencies, or in some cases to two overdamped modes with different decay constants, similar to the inertial fission mode.

For the unstable fission mode, Kramers [4] gave an exact stationary solution to the Fokker-Planck equation for the phase-space probability for the situation when the potential is parabolic, and the inertia and dissipation are constant. I use this solution, as elaborated in Ref. [13], to select the distribution of starting momenta along the unstable fission eigenvector near the saddle point. For the other normal modes, to simplify the treatment, I use the frequencies and distributions for the non-dissipative system.

Explicitly, for neutron-induced fission, I use the following algorithm to determine the random starting condition for each trajectory:

1. Choose the central starting shape coordinates. In practice, in order to avoid wasting time on trajectories that end up going to more compact shapes and ending up in a local minimum (fission isomer), I choose a central coordinate which is shifted to the outside of the outermost fission saddle point (second or third barrier) by a small increment along the non-dissipative fission eigenvector. I have verified that there is no discernable difference in final distributions from starting from this position compared to starting exactly at the saddle point. The less elongated starting shape simply leads to many more trapped trajectories, which make the computations significantly less efficient.

2. Find the excitation energy at this deformation by comparing the potential energy to the starting total

energy. This allows the local temperature to be defined.

3. Randomly sample the Kramers velocity distribution for this temperature to select a starting velocity along the fission eigenvector. As in the earlier step, I only consider positive velocities to avoid large numbers of trapped trajectories.

4. Define a new temperature for the remaining four degrees of freedom by reducing the available energy by the amount of kinetic energy in the fission mode.

5. Choose random coordinate increments and momenta along the non-fission eigenvectors by sampling the appropriate gaussian distributions [7].

6. Rescale the magnitude of the total momentum vector if the total kinetic plus potential energy is larger than the initial excitation energy. This can occur because I independently sample the probabilities for each bound normal mode for simplicity, and have not considered the more difficult to calculate multidimensional joint probability.

#### 2. Starting conditions for spontaneous fission

A truly physical model of spontaneous fission would require calculating barrier penetrabilities with a more realistic inertia model than that used in this study. Such semi-realistic calculations are beyond the scope of this study, and are extremely difficult for five-dimensional barriers. In lieu of such an approach, I have adopted an extremely simple heuristic approximation. I choose the mesh point along the bottom of the fission valley whose energy is closest to the ground-state energy for the fissioning isotope [34, 37]. I define the potential energy and the 3QS coordinates on minimeshes around this point, by the use of splines, exactly as described in Sec. II C 2. I calculate the energy on all $8^5$ points on the minimesh, and store the coordinates for all the points whose energy is within 0.001 MeV of the ground-state energy. This criterion selects around 200–500 shapes for the systems so far tested. The mean coordinates and standard deviations of the coordinates are defined from this ensemble of possible exit points from the barrier. I randomly sample starting coordinates from gaussian or rectangular distributions of various widths centered at the mean exit point found, and begin with zero momentum. Because of the approximations involved in both the independent sampling of each coordinate, and the spline approximations for the coordinates, the actual energies of the points randomly selected can vary from the actual ground-state energy. To mitigate this, the first coordinate $\sigma_1$ is varied to give a potential energy within a certain window around the ground-state energy. The values used for the energy window and the widths of the resulting distributions are discussed in Secs. IV C 3 and IV D. This technique has been supplemented in the case of $^{240}$Pu(SF) by including a small admixture of trajectories beginning in the symmetric fission valley, again with a distribution of starting coordinates. The relative probability of exiting in the neighborhood of either valley cannot be calculated with any precision, and is employed as a free parameter to improve the modeling of the symmetric yield, when necessary.

#### 3. Keeping the shape inside the mesh

Preliminary test calculations with a reduced Langevin term in the momentum equation led me to increase from an initial guess the size of the fragment-eccentricity meshes, the number of neck mesh points, the extent of the more closely spaced part of the $R_1$ mesh and to the maximum value of $R_1$. The great majority of Langevin trajectories then lie within this extended mesh. However, due to the random nature of the Langevin force, it is possible for a system to attempt to evolve outside the boundaries of the mesh, or to otherwise approach shapes for which the inertia tensor may be singular. An example of the latter is when a shape evolves to resemble two spheroids with a cusp between them ($\sigma_2 \ll 0$). Because of the nature of the finite-range nuclear energy, there is no force acting to prevent such shapes, which have a singular inertia tensor. Depending upon the overall elongation, longer shapes may tend to evolve to very prolate ends, again with a cusp trying to form between them. These shapes can exceed the maximum fragment eccentricity allowed in the mesh. Another type of shape that can occur occasionally has highly oblate end fragments, again falling below the minimum values of $\varepsilon_{\rm f}$ allowed on the mesh of $-0.5$. In lieu of just throwing away all trajectories which try to leave the mesh, or lead to cusps between the end fragments, I elected to define conservative pseudopotentials which push trajectories away from such shapes. It was discovered that three such pseudopotentials prevented the great majority of pathological terminations of fission trajectories. I define three separate dimensionless pseudo-curvature-energy terms:

$$B_{\rm cvi} = F_{\rm cv}(x_i), \text{where } i = 1, 2, 3, \tag{28}$$

and $F_{\rm cv}(x)$ is a function which is 0 for $x \leq 0$, and has the form

$$F_{\rm cv}(x) = exp(x) - 1 - x - x^2 \tag{29}$$

for $x > 0$; $x_i = \beta_i(\kappa_i - \kappa_{i0})$, $\beta_1 = 55$, $\kappa_{10} = 1.2$, $\beta_2 = -10$, $\kappa_{20} = 0.37$, $\beta_3 = 4$, and $\kappa_{30} = 2.3$,

$$\kappa_1 = -\frac{a_3^2}{c_3^2} \text{ if } \sigma_2 < 0,\ z_1 \leq l_3 \leq z_2, \text{ and } a_3 > 0.15;$$

0 otherwise, $\kappa_2 = min\,(\frac{a_1^2}{c_1^2}, \frac{a_2^2}{c_2^2})$, and $\kappa_3 = max\,(\frac{a_1^2}{c_1^2}, \frac{a_2^2}{c_2^2})$.

The conservative pseudo-curvature-energy terms have zero value, first and second derivatives at their respective thresholds, and then rise rapidly as the system tries to move into the 'forbidden' region. One may think of these functions in analogy to an imaginary ice rink, where the outside edges, instead of having a wall, have a smoothly rising curved ice surface which pushes out-of-control skaters leaving the regular surface back onto it with conserved total energy.

To assess how much of an effect these conservative artificial energy terms have on actual fission calculations, the number of time steps for which one of the pseudo-curvature energies was greater than 0.001 MeV was tallied. For a sample of 1000 $^{235}$U(n, f) fission trajectories with thermal neutrons, there were a total of 728, 336 time steps calculated. Of these, the pseudo-curvature energy exceeded 0.001 MeV for 1.9% with $E_{\rm cv1}$, 0.5% with $E_{\rm cv2}$, and 0.2% with $E_{\rm cv3}$. Only 6 trajectories had any pseudo-curvature energy at scission, all with less than 1 MeV, and only two trajectories had to be discarded because of reaching an unphysical shape. In contrast, without the pseudo-curvature-energy terms, the same test calculation had 120 trajectories which terminated due to reaching unphysical shapes, and the entire simulation took 1.3 times as long to achieve fission in 118 fewer cases. The problems with systems leaving the mesh become more severe for reactions induced by higher energy neutrons; with correspondingly higher efficiency being effected by these 'walls' to the mesh.

### H. Post-scission model

Experience with earlier macroscopic fission dynamical studies [8, 15, 44] has demonstrated the need to go beyond just calculating the Coulomb interaction energy at scission when modeling fragment total kinetic energies (TKE). Unless the motion is so highly dissipative that the fragment deformations are effectively 'frozen' during the initial separation, the interaction of the dynamically changing fragment deformations as they separate will change the acquired kinetic energy from the initial interaction energy by up to a few MeV. When comparing to data as is done in Fig. 5, such differences are significant.

A multipole expansion of the interaction energy [5] shows that the most important terms to consider involve the monopole and quadrupole moments of the fragments. A simple method to approximate these effects is to model the separating fragments as spheroids. A further simplification is to constrain the spheroids to be coaxial. This freezing of angular orientation variables will lead to a very slight overestimation of the final TKE, but simple estimates of the torques involved suggest that the fragments will not rotate very far until they are well apart. When one wishes to model the fragment angular momentum distributions, important for modeling gamma deexcitation of the fragments, more careful consideration of the angular degrees of freedom will become important.

With the coaxiality constraint, the system then has three degrees of freedom; the deformation of each fragment and the separation of their centers of mass. The mass asymmetry is of course fixed for separated fragments. The deformation of a spheroid may be described many different ways; I choose to use the shape moments $\sigma_{\rm L}$ and $\sigma_{\rm R}$, where:

$$\sigma_i = \sqrt{\frac{< z^2 >_i}{< z^0 >_i} - \left[\frac{< z >_i}{< z^0 >_i}\right]^2},$$

where the moments of the spheroids are defined just as following Eq. 16, by replacing the integration limits by $-c_i$ and $+c_i$, with $c_i$ the semi-symmetry axis of the L or R spheroid. The notation $\sigma_i$ is used for historical reasons, being defined exactly like the standard deviation of a distribution, often designated as $\sigma$. In the context, with the subscript $i$ being L or R, it should not be confused with the symmetric 3QS coordinates defined in Eq. 6, which have the subscripts 1, 2, or 3.

For this very simplified post-scission model, which attempts to account for the Coulomb interaction of the fragments as their deformations change as they separate, to save time, I use only the macroscopic energy. Thus the fragments will relax in time to spheres, instead of to their possibly deformed ground states. Because there is no dissipation acting on the separation coordinate, and because the integration of the post-scission motion is carried out until the fragments have relaxed to spherical shapes, I do not consider the Langevin term in the equations of motion. The fluctuations in the dynamical evolution of the spheroids would only give small changes to the final kinetic energies calculated, and are not worth the extra complication. These simplifying assumptions lead to the equations of motion:

$$\begin{aligned}
\mu\frac{d^2R_2}{dt^2} &= -\frac{\partial V}{\partial r} \\
M_{\rm L}\frac{d^2\sigma_{\rm L}}{dt^2} &= -\frac{\partial V}{\partial \sigma_{\rm L}} - \frac{1}{2}\frac{dM_{\rm L}}{d\sigma_{\rm L}}\dot{\sigma}_{\rm L}^2 - \eta_{\rm L}\dot{\sigma}_{\rm L} \\
M_{\rm R}\frac{d^2\sigma_{\rm R}}{dt^2} &= -\frac{\partial V}{\partial \sigma_{\rm R}} - \frac{1}{2}\frac{dM_{\rm R}}{d\sigma_{\rm R}}\dot{\sigma}_{\rm R}^2 - \eta_{\rm R}\dot{\sigma}_{\rm R}.
\end{aligned} \tag{30}$$

The inertias $M_i$ are the irrotational inertias for spheroidal deformations, which can be calculated analytically. The diagonal dissipation tensor elements $\eta_i$ correspond to the pure surface dissipation model; the window between the fragments is gone, with the only remaining dissipation due to the interaction of the fragment internal nucleons either with or in the neighborhod of the moving surface of the fragments. The potential energy contains only the nuclear macroscopic energy and the diffuse-surface Coulomb energy, calculated using exactly the same surface-integral formulas as used for the single prescission shape. With the fragments having the mass

numbers $A_1$ and $A_2$, the following definitions lead to the values of the inertia and dissipation coefficients:

$$\begin{aligned}
\mu &= \text{the reduced mass } F_1F_2,\\
M_i &= F_i(1+\frac{F_i}{2c_i^3}),\\
F_i &= \frac{A_i}{A},\\
c_i &= \sqrt{5}\sigma_i\\
\eta_i &= \frac{\pi\rho\langle v\rangle}{8}k_{\rm s}G_i\left[\frac{{F_i}^{\frac{3}{2}}}{{c_i}^{\frac{5}{2}}}\right],\\
\alpha_i &= 1-\frac{F_i}{{c_i}^3},\\
G_i &= \left[\frac{1}{{\alpha_i}^2}\right][(-27+6\alpha_i)\sqrt{1-\alpha_i}+Q_i\,(27-24\alpha_i+8{\alpha_i}^2)],\\
Q_i &= \frac{\log[\sqrt{(1-\alpha_i)}+x_i]}{x_i} \qquad \text{if } \alpha_i < -0.01,\\
Q_i &= \frac{\arcsin(x_i)}{x_i} \qquad \text{if } \alpha_i > 0.01,\\
x_i &= \sqrt{|\alpha_i|}. \qquad (31)
\end{aligned}$$

For values of $|\alpha_i| \le 0.01$, a series expansion in powers of $\alpha_i$ is used for $G_i$.

The starting values for the post-scission dynamics are taken from the scission configuration from the Langevin simulation of each trajectory. The values of $R_2$, $\dot{R}_2$, $\sigma_i$, and $\dot{\sigma}_i$ for the scission shape are held continuous at scission, which is defined by the neck radius reaching the specified value (see Sec. III). The equations of motion are integrated until the value of $R_2$ reaches 20 $R_0$, where $R_0$ is the radius of the fissioning nucleus. With the values of the surface dissipation coefficient used in all the calculations presented in this study, the fragment nuclei have relaxed to spheres by this time. The final kinetic energy (TKE) is calculated by adding the remaining Coulomb interaction energy to the calculated kinetic energy at this late time. The TKE is corrected by adding the calculated nuclear interaction energy of the fragments at scission and adding the remaining Wigner energy, which is the difference between the final value of $B_{\rm W} = 2$ and the value of Eq. 21 at the scission shape.

## III. PARAMETERS IN THE MODEL

There are a considerable number of approximations made in this model. Some are done for convenience, and others reflect ignorance of certain physical effects. I have adopted a limited number of quantities which may be varied to assess the sensitivity of the results to model details, and in some cases to empirically include effects beyond the ability of the model to specify with precision. I also include certain known physical effects, such as the fact that many experimental data sets are the results of experiments with limited mass resolution. As I show later, the model sometimes is quantitatively quite accurate when compared to certain data. Some adjustment of parameters is done to optimize one class of observables to allow the assessment of how well the model allows prediction of certain other quantities. This allows a partial assessment of whether the model may be useful as a predictive tool for evaluating certain quantities that have not or cannot be measured for interesting isotopes.

But at the outset, I will stress that with one small exception, described in Sec. III 1. the potential-energy surface is taken as specified by the macroscopic-microscopic mass model [34, 37]. The microscopic-model parameters are essentially as determined in 1974 [62], with small interpolating corrections as discussed in Ref. [37]. The parameters of the macroscopic model are determined nearly entirely from global fits to nuclear masses [34, 37, 47], which involve only relatively small deformations, including some information on a few measured fission-barrier heights used to slightly modify the model constants determined mostly by nuclear masses. The entire portion of the potential surface relevant to fission lies at much larger deformations, with the details of the fission potential surface being a major extrapolation of the model outside the space where its constants were determined. To the extent that certain observable quantities such as multi-humped barriers, barrier heights, fission-isomer energies [39], mass asymmetry of fission-fragment yields [38, 48, 104] correspond with measured values provides a powerful test of the global nature of the model. No parameters of the macroscopic-microscopic model have been adjusted to **any** fission observables in this study.

### 1. *Stutinsky smoothing range*

I do not wish to delve deeply into the details of the Strutinsky procedure for calculating the microscopic corrections to the macroscopic potential energy. There is an extensive literature on the subject, starting from the beginning of the use of the technique. There is one important difference in studies of fission as compared to nuclear ground states; that is, the occurrence of larger deformations in the former. The Strutinsky smoothing range that has proven very successful for studies of nuclear masses [34, 37], is $1.0B_{\rm S}\hbar\omega$, where $\hbar\omega$ corresponds to the separation of major shells for spherical nuclei and $B_{\rm S}$ is the surface area of the shape normalized to that of a sphere. The optimum smoothing range is determined empirically to lie within a range where the calculated microscopic energy has roughly 'plateaued' for small variations of that parameter. The plateau condition is satisfied when the range is in the neighborhood of the separation of major shells. When the deformations are extended well beyond those of nuclear ground states, but well before scission, the separation of major shells can be considerably larger than near the ground state, as is illustrated in Fig. 7 of Ref. [105]. Thus, for large deformations, the smoothing range which works well and has been adopted for

mass modeling may be too small to reach the plateau region. This is discussed in Ref. [106]. Following that study closely, for this work, I have adopted the value of

$$\gamma = 1.4 B_{\rm S} \hbar\omega. \tag{32}$$

This value is used for all the calculations presented, and is not varied.

#### 2. Starting coordinates and widths

To implement the prescription described in Sec. II G 1, the starting conditions should be randomly sampled from the gaussian distributions of normal-mode displacements and momenta defined there. It is obvious that a significant fraction of trajectories starting from the saddle point would end up trapped in the fission-isomer or the third-minimum regions, not contributing to fission in any reasonable time. In addition to the approximations described in the section II G 1, I have allowed the coordinate and momentum widths from the transition-state analysis to have arbitrary multipliers. Empirically, I have found that a nonzero coordinate width leads to a significant number of trajectories becoming trapped in a minimum inside the outer saddle. This leads to a major increase of computational cost to calculate any particular number of fissioning Langevin trajectories. In nearly all the calculations I will present, the coordinate-width multiplier will be set to 0. With limited testing, I have not found any systematic variation of observables such as yields with this multiplier, only that as the value of it increases, the efficiency of the calculation suffers significantly. I find that the final distributions are not very sensitive to the initial assumptions about the momentum width, and generally use the default value of 1.0. For the ranges of physical parameters checked so far, the action of the Langevin random force over the trajectory seems to overwhelm variations of the starting widths of the momentum distributions. The effective value of the momentum width is reduced for fission at low excitation energies by the process of enforcing energy conservation which leads to reducing the randomly selected starting momentum vector as described in Sec. II G 2.

#### 3. Inertia tensor scaling

The use of a scaling parameter to vary the magnitude of the inertia tensor is discussed in Sec. II D.

#### 4. Dissipation tensor scaling

The SPW dissipation model contains the empirical constant $k_{\rm s}$, which multiplies the surface-dissipation integral. This parameter is varied to investigate the effect of changing the overall strength of this contribution to the dissipation. Since the window dissipation models the change in relative momentum between two parts of the system due to the flow of nucleons between the parts, it is not physical to just multiply it by a scaling factor, so it remains unchanged when $k_{\rm s}$ is varied.

#### 5. Scission neck radius

I define scission in this model as occurring when the minumum neck radius falls to a specified value in fm denoted by $R_{\rm sc}$. The chosen value can be varied to analyze how sensitive the results are to this parameter.

#### 6. Mass resolution

A majority of existing detailed fission measurements of yields and TKE's have been done using dual ionization chambers or silicon detectors which measure the kinetic energies of both fragments. There is an inherent uncertainty of the fragment masses deduced from such measurements which is hard to calculate exactly, but which is estimated to be in the neighborhood of 3–5 mass units. The largest part of this uncertainty occurs because of the inability to measure the number of neutrons emitted in an individual event. Another significant uncertainty is due to correcting the observed signals for the energy not being measured in an ionization chamber or solid-state detector due to energy losses in non-sensitive parts of the apparatus and in the target itself. To the extent that the average number of neutrons emitted varies with the mass of the fragments, in principle the mass uncertainty may also be a function of the fragment mass. This complication will be ignored because of the difficulty of modeling it accurately. In order to compare calculations of this model to such data, I introduce a constant mass-resolution uncertainty. At the end of each trajectory calculation, the calculated mass of one fragment has an increment added to it which is chosen from a gaussian-distributed random number with standard deviation $\Delta A$. Including this random mass 'smearing' has not only the obvious consequence of broadening the calculated mass distribution, and increasing the apparent symmetric yield, but also the less obvious effect of changing the slope of the TKE(A) function in the region of maximum yield, where it has a nearly linear behavior. This quantity has often been measured and tabulated. As pioneered by the Cosi fan Tutti spectrometer measurements at ILL, Grenoble [107], recently, experiments which measure both the energies and velocities of fission fragments are beginning to produce data sets with much improved mass resolution [108]. Yields with mass resolutions approaching 1 u will provide a much more stringent test of models than do the historical lower-resolution distributions.

### 7. Additional fission modes

For many years various measurements of fragment yields and TKE yields have been interpreted in terms of distinct modes of fission. By mode, I mean a subset of events which seem to have a particular average peak yield, and possibly a distinctly different average energy compared to the entire distribution of fission events. For subactinide fission in the radium region, the separate modes may be particularly distinct, with a triple-humped mass distribution, with very different average TKE's for events in the different mass peaks, and different energy dependences of their relative probabilities [109]. Frequently, the distribution between or among different modes apparently changes with the energy of the system. In the context of this model, more information is available from the Langevin trajectories than experiments can be expected to yield. As seen in the analysis of the potential-energy surface presented in Fig. 3, because of the properties of the shapes in the two identified valleys in the potential energy for $^{236}$U, one would expect that systems following the asymmetric valley would obviously have an asymmetric mass distribution, and a higher TKE because the scission point will be much more compact in that valley, as seen by the disappearance of the neck for shapes with a separation of less than $2.15R_0$. The symmetric mode will have a symmetric mass distribution, and a significantly lower TKE because scission will occur at much more elongated shapes.

For many actinide nuclei, only one outer saddle point can be easily identified by immersion analysis of the surface. As described previously, I choose to start the system off near the identified saddle point, because I are unable to practically calculate the trajectories of particles in the outermost minimun of the surface, waiting until particular trajectories eventually make their way over the barrier to fission. It is at least plausible to assume that some fraction of systems will find themselves exiting into the symmetric valley, while it is totally impractical to accurately calculate this fraction directly because of the inherent uncertainties of the model, as reflected in, e.g. the theoretical error in mass models [34, 37]. The inherent uncertainty in the model means the relative energies of the valleys and the ridge near their beginnings must reflect this uncertainty. For this reason I will introduce an empirical parameter which describes the probability the system finds itself in the symmetric valley; in which case it is started out at a point in that valley whose energy is not far from that of the asymmetric valley. A random-number generator is used to select an appropriate number of trajectories that start in the symmetric valley.

Just as the exact relationship of the energies of the valleys are inherently uncertain in the macroscopic-microscopic model, so too, the 'real' height of the ridge separating the valleys may be higher or lower than calculated in the model. In the case when too many trajectories find their way into the symmetric valley to properly model the observed symmetric fission probability, I employ a random probability to discard a fraction of the trajectories which enter the symmetric valley. Because of the nature of the potential surfaces explored so far, I find that trajectories reaching the symmetric valley almost always remain there, so discarding a fraction of them is the simplest way to proceed to reproduce observed mass yields. Of course, if the only data being studied were mass yields, this exercise would be futile. However, since the model describes TKE's, TKE($A_{\rm frag}$), and other observables, it is possible to find out whether or not this addition or subtraction of another fission mode leads to a more consistent picture of the fission process.

### 8. Random neck rupture

The default definition of scission adopted in this work is that it occurs when the neck radius decreases to a prespecified value. The plane of scission is perpendicular to the axis of symmetry and located at the minimum neck radius. The details of the precise physical nature of the scission process lie outside the scope of the relatively slow shape dynamics modeled in this study, but almost certainly involve shorter timescales more characteristic of the Fermi motion of nucleons, and the quantum dynamics of those wavefunctions with significant probability in the neck region. Additionally, even in the restricted context of this dynamical model, keeping only five coordinates does not allow much additional freedom once the nascent-fragment masses and deformations have been specified. In addition, one expects the inherent quantum nature of regions of low density to lead to some 'fuzziness' of the exact point of rupture of the neck. The idea of random neck rupture is quite old [110, 111]. Although the physical ideas underlying our conception of random neck rupture differ somewhat from those in Refs. [110, 111], the resulting empirical definition of the variance of the neck position bears a slight resemplance to the earlier work. To investigate how this ignorance of the exact point of scission affects the model results, I have allowed the possibility of randomly varying the axial (z) coordinate of the scission plane away from the point of minimum neck radius. This random scission model uses a gaussian random number with a specified standard deviation to be added to the default location of the scission plane. Because low-probability shifts with large values make no physical sense, the gaussian distribution is truncated by use of rejection to limit its maximum shift to a number slightly (usually 0.5 fm) larger than the standard deviation of the gaussian distribution sampled.

## IV. RESULTS

I present distributions of quantities calculated for a sufficiently large number of Langevin trajectories that the statistical uncertainties of the studied quantities are

sufficiently low for meaningful comparisons. Most of the results shown are for 1–5×$10^5$ trajectories. The process for selecting the random starting conditions for each trajectory is outlined in Sec. II G 1. For neutron-induced fission, the starting total energy is the sum of the neutron kinetic energy and the neutron separation energy. This starting energy is corrected for the model ground-state microscopic correction [34, 37], since the potential surface is defined with respect to the macroscopic spherical energy. The starting coordinate shape is usually held fixed as a small displacement outside the outermost saddle point. The starting momentum vector is chosen as described previously, with a possible renormalization to limit the total energy. When scission occurs, the mass of each fragment is defined. The proton number of each fragment is scaled exactly with the mass, with the values kept as real numbers, not integers. The coordinates for the last three time steps are used to define quadratic approximations to the time dependence of the coordinates, giving the exact point of scission and the scission values of the moments and time derivatives to specify the starting conditions for the post-scission motion. If a finite mass resolution is used, the mass split is randomly broadened to reflect the experimental uncertainty of the mass resolution and stored. The mass split used for the post-scission motion is maintained at the actual modeled value, since the real mass split cannot be affected by the uncertainty in its measurement. The events are finally binned in 1 u mass bins, and 1 MeV TKE bins, with selected distributions saved for analysis. Certain other quantities are calculated and used to extract averages and standard deviations of interesting quantities which might not be measurable, such as fission dynamical times, scission temperatures, fragment translational kinetic energy at scission, etc. In all the plots of model results given below, the error bars are 1-$\sigma$ statistical binning uncertainties. Experimental data points only have error bars when they have been specified in the experimental data sets.

The term default model used below refers to an unscaled Werner-Wheeler inertia, the original strength of the SPW dissipation, $k_s = 0.27$, no distribution of initial shape coordinates (for induced fission), the nominal statistical widths of the starting momentum distributions defined by the starting excitation energy or temperature, a scission neck radius of 1.0 fm, only asymmetric-mode fission, and a mass resolution parameter characterized by the experiment simulated.

## A. $^{236}$U

The fission of $^{235}$U induced by a neutron, the earliest-discovered and most studied fissioning system, is the first nuclide I consider. A few of the important features in the potential-energy surface for $^{236}$U are presented in Fig. 3. Following the prescription described previously, the starting shape is found by displacing by 0.15 times a normalized fission eigenvector from the calculated outermost (third) saddle point. The saddle point has a deformation of $R_1 = 0.80$ and an energy of 2.40 MeV. The starting point has a deformation of 0.81 and an energy of 2.03 MeV. The ground-state microscopic energy is -1.08 MeV, and the neutron separation energy is 6.60 MeV [37].

The $^{236}$U system will serve as a test case to establish the effect of varying the model parameters on the predicted results.

### 1. *Thermal-neutron induced fission*

For the fission of $^{235}$U induced by a thermal neutron, the default model with a neutron kinetic energy of 0.00 MeV is used. The first data compared to is from an evaluation of several 2E measurements used to generate input pre-evaporation distributions to sample for the Monte-Carlo post-scission decay model CGMF [112, 113]. This type of fragment yield data has an inherent uncertainty in the mass identification of roughly $3-5$ mass units, due both to the neutron evaporation models and data used to infer the pre-evaporation yields, and to systematic uncertainties in correcting measured fragment energies to infer the immediate post-evaporation values. The default model calculations with a mass resolution parameter of $\Delta A = 4.0$ give the yields shown in Fig. 6. The TKE distribution is shown in Fig. 7, and the average TKE as a function of fragment mass in Fig. 8. It is remarkable that the mean mass of the heavy-fragment peak is predicted to within 0.2 mass units, and the yield is well represented over 3 orders of magnitude, except for the symmetric region. It is worth repeating that the potential-energy model has no parameters adjusted to mass asymmetries observed in actinide fission. It is also striking that the predicted mean kinetic energy is within 1.6% of that measured, even with an admittedly quite crude model for post-scission fragment dynamics. The predicted width of the TKE distribution is about 20% too large. There is no other non-empirical model which has made predictions for this quantity. There are some significant discrepancies near the symmetric yield minimum for the TKE(A) displayed in Fig. 8, but the predictions are within 4 MeV of the measurements for the entire heavy-fragment yield peak from A = 135 to A = 160.

There exist other data sets in which some or all of the quantities presented in the previous three figures have been measured. I compare the identical model calculations to the measurements of Straede, et al. [114] in Figs. 9–10 This data displays an effective mass resolution in the yield that is narrower than that of the previous data set. I show the results of the same Langevin trajectories with a mass resolution of 3.0 u compared to the Straede data. The TKE probability distribution is not plotted because the model results do not depend upon $\Delta A$. The Straede data exhibits the mean value of 172.2 MeV, with $\sigma_{\rm TKE} = 12.2$ MeV. This width is coincidentally almost

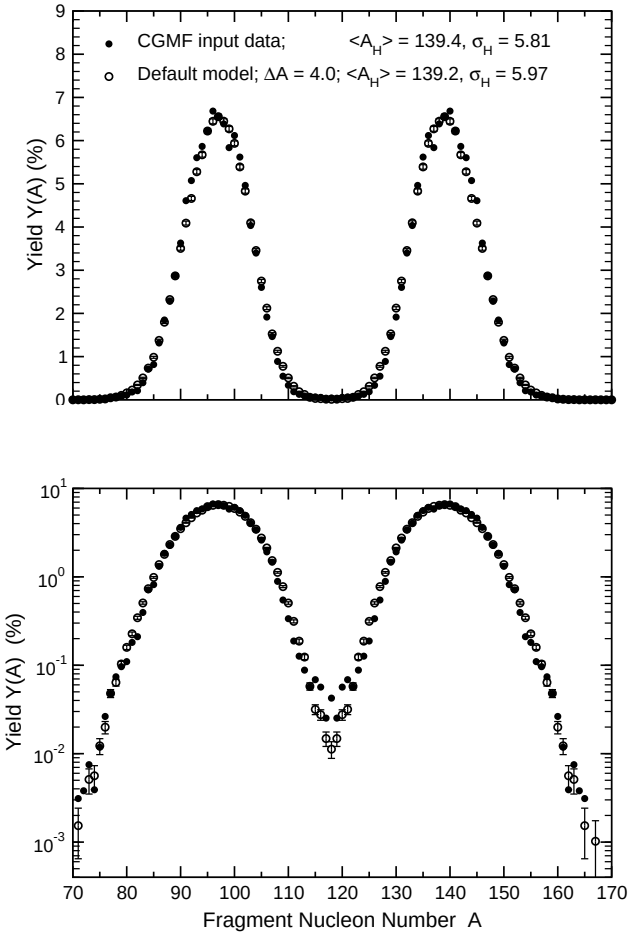


FIG. 6. Calculated pre-evaporation fragment yields as a function of fragment mass number A from the default model with a mass resolution $\Delta A = 4.0$ u for thermal-neutron-induced fission of $^{235}$U, compared to evaluated experimental data [113]. The upper part has a linear yield scale, while the lower part shows the same points with a logarithmic yield scale.

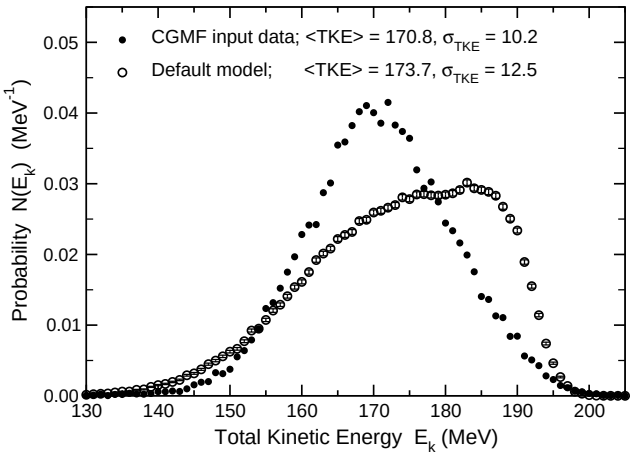


FIG. 7. Calculated pre-evaporation total fragment kinetic energy distribution from the default model for thermal-neutron-induced fission of $^{235}$U, compared to evaluated experimental data [113].

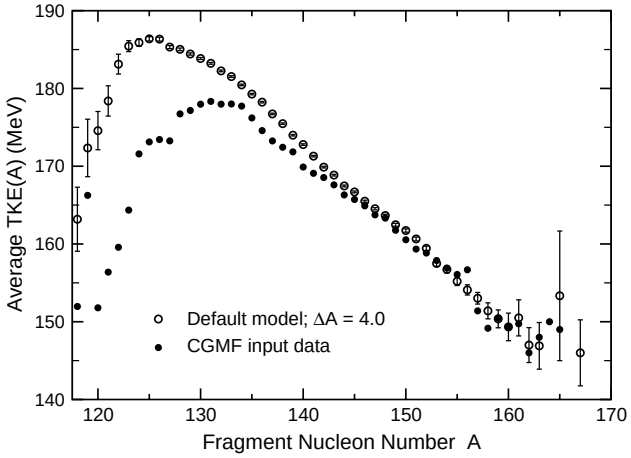


FIG. 8. Calculated pre-evaporation average total fragment kinetic energies as a function of fragment mass number from the default model with a mass resolution $\Delta A = 4.0$ u for thermal-neutron-induced fission of $^{235}$U, compared to evaluated experimental data [113]

exactly the same as from the model, but with a much more symmetric distribution (smaller third moment) in the data than in the model. The relatively large difference between the two data sets may suggest that the systematic uncertainty in the absolute value of the mean TKE for thermal-neutron-induced fission is of the order of 1.0–1.5 MeV, and the measured value of $\sigma_{\rm TKE}$ is uncertain at least to the 20% level. There is an interesting discrepancy between the mass resolution inferred from the yield data, and that from the TKE(A) measurements. I will show below that the slope of the modeled TKE(A) curve in the region of the mass-yield peaks is sensitive to the mass resolution. For the Straede data, the mass yield suggests a resolution of 3.0 u, while the slope of TKE(A) in the region $A = 135$–160 suggests a resolution as low as 4.0 u. Of course, since the default model predicts a much larger TKE for $A \sim 122 - 134$, the apparently steeper model slope in the $A \sim 135 - 140$ region may be a reflection of similar, but smaller deficiencies of the model for masses above 134.

Even without employing any of the model parameters, the simulations capture most of the features of the data, in some cases with high quantitative precision. The CGMF data set appears to have more symmetric yield than the model, but the Straede symmetric yield is close to the model with the increased mass resolution. One may surmise that the symmetric yield inferred from such 2E measurements is significantly more uncertain than the peak yields.

From these comparisons, one may conclude that for thermal-neutron-induced fission of $^{235}$U, the default

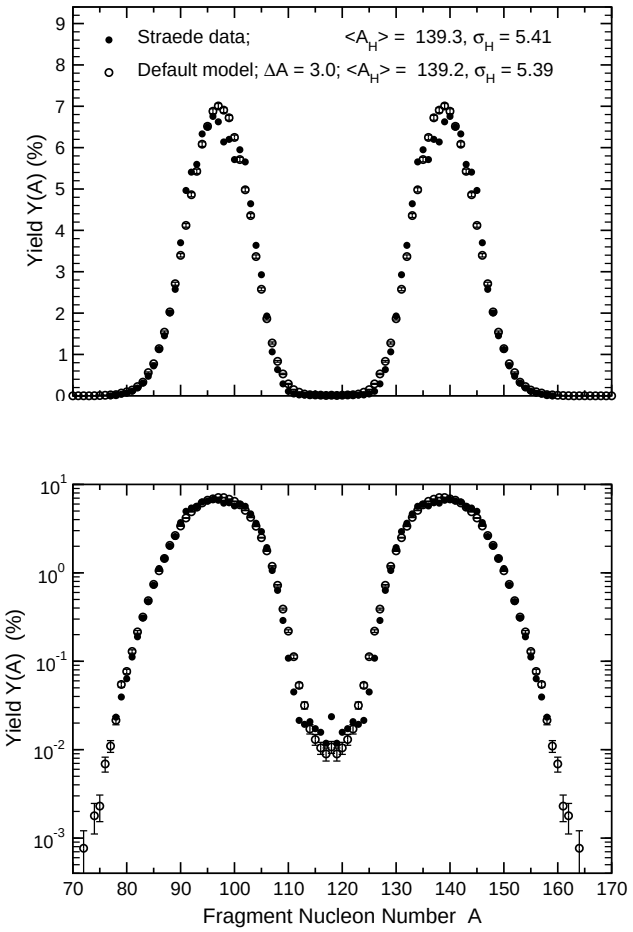


FIG. 9. Calculated pre-evaporation fragment yields as a function of fragment mass number A from the default model with a mass resolution $\Delta A = 3.0$ for thermal-neutron-induced fission of $^{235}$U, compared to the data of Straede [114]. The upper part has a linear yield scale, while the lower part shows the same points with a logarithmic yield scale.

model gives very good predictions of $< A_H >$ and $\sigma_A$ for the data measured in 2E experiments, which have inherent mass resolutions in the range of 3–4 u. The mean TKE is slightly overpredicted before any model variations are considered, while the TKE width is close to one data set and about 20% too large for another one. The TKE(A) is very well predicted for values of A above about 135, and in some cases near symmetry, a region with about 95% of the total yield. This prediction of TKE(A) means that the predicted shapes in the heavy-mass and light-mass peaks are well represented. The model predicts significantly too much kinetic energy for mass splits from about 114/122 to 102/134.

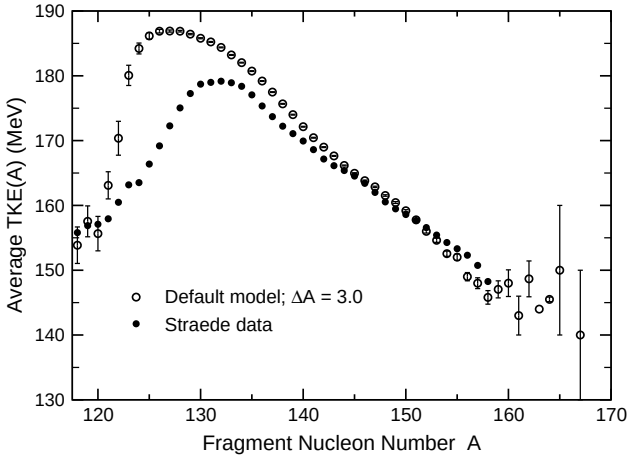


FIG. 10. Calculated pre-evaporation average total fragment kinetic energies as a function of fragment mass number A from the default model with a mass resolution $\Delta A = 3.0$ for thermal-neutron-induced fission of $^{235}$U, compared to the data of Straede [114].

### 2. *Post-evaporation yields*

A different class of data for the same fission reaction exists in the form of evaluated prompt yields. These data represent experiments which attempt to deduce the yields of fission fragments after prompt neutron emission, and before beta decay processes have occurred. In order to compare model results to such tabulations, the primary yields from the model must be corrected for neutron evaporation by use of a suitable model. For this purpose I use a semi-empirical Monte-Carlo neutron evaporation model which uses experimental data on the average number of neutrons, the distribution of average neutron number as a function of fragment mass, the fission neutron kinetic-energy distribution, and the multiplicity distribution of prompt neutrons [116]. The yields of post-evaporation fragments as a function of their mass number from the default model are compared to the evaluation of England and Rider [115] in Fig. 11. The two most obvious deviations of the model from the evaluation are the detailed structure near the yield peaks seen in the data compared to the smoother model, and the major underestimation of the width of the mass-yield peaks by the default model. It is interesting that the model gives almost the correct symmetric yield, while still getting the widths so poorly. In order for the model to represent this data, it becomes necessary to employ the random neck rupture.

### 3. *Effect of varying model parameters*

In this section I discuss the effect of varying some of the model parameters introduced in Sec. III.

A first test is of the approximation mentioned previ-

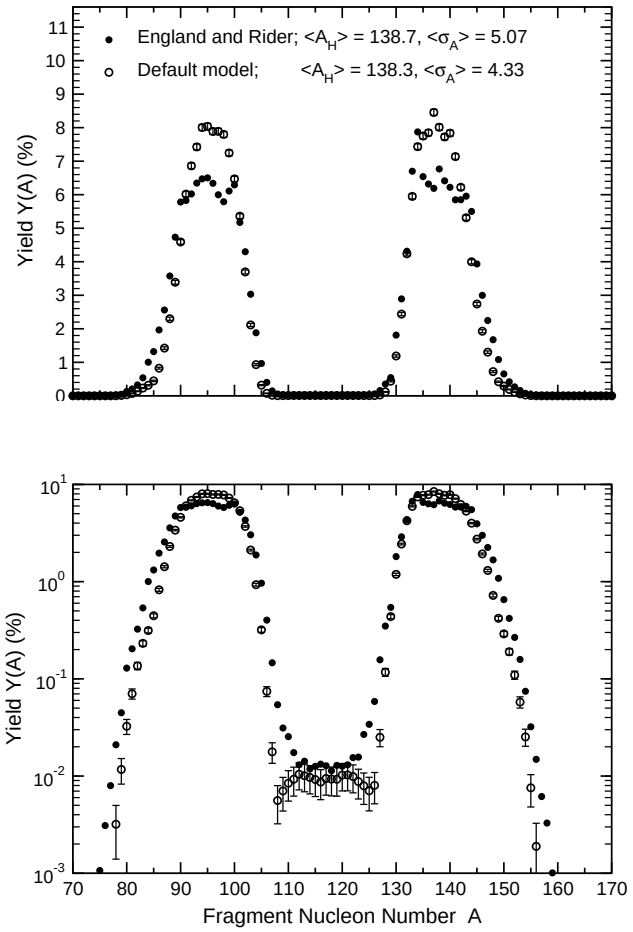


FIG. 11. Calculated post-evaporation fragment yields as a function of fragment mass number A from the default model for thermal-neutron-induced fission of $^{235}$U, compared to the evaluation of England and Rider [115]. The upper part of the figure has a linear yield scale, while the lower part has a logarithmic yield scale.

ously to not allow the starting coordinates for the Monte-Carlo trajectories to vary. Two different runs with the default model of approximately $10^5$ trajectories are made, one with all trajectories starting at the same deformation point, and the other one with the starting points randomly distributed along the transverse eigenvectors as outlined in Sec. II G 1. For the width of the gaussian distribution of transverse coordinates, I use a renormalization factor of 0.5 from the actual value from the transition-state model. This is to prevent too large a fraction of trajectories from terminating at unphysical shapes. The run with no variance of the starting coordinates has more than 99% of its trajectories fission, while the run with half the canonical standard deviation in the starting shape coordinates has about 90% of the trajectories fissioning. The mean value of the heavy mass, its standard deviation, the mean TKE and its standard deviation are all statistically identical for these two runs.

The comparison of the prompt yields to the evaluations shown in Fig. 11, shows that the only way within the model to model the mass-yield widths properly is to include a random neck rupture as discussed in Sec. III 8. It is found that a random-neck parameter in the range of 1.0 to 1.5 fm is needed to reasonably reproduce the observed prompt yield width.

The next parameter considered is the neck radius at which scission is defined to occur. Heretofore, the value of 1.0 fm for neck radius is used. Increasing the neck radius from 1.0 fm to 2.0 fm in steps of 0.25 fm leads to an increase of the mean mass of the heavy fragment from 139.2 to 139.6, while the standard deviation of the heavy-fragment mass yield increases very slightly from 5.97 to 6.11. This behavior reflects the property of the asymmetric valley, whose energy is shown in Fig. 3; the asymmetry of the valley decreases as $R_1$ increases, and its width becomes narrower (See Fig. 8 of [60]). The mean TKE decreases over the same change in the neck radius from 173.6 to 170.9 MeV. The standard deviation of the TKE distribution decreases from 12.5 to 11.7 MeV.

Increasing the inertia scaling from 1.0 to 2.0 causes a shift of the average heavy mass from 139.2 to 139.5, while the mass width decreases from 5.97 to 5.85. The average TKE drops more than 3 MeV, and the TKE width goes from 12.5 to 12.2.

Varying the surface dissipation coefficient from -20% to +20% from its default value 0.27 causes the mean mass to increase by 0.13 u, and the mass width to decrease by 0.10 u. As was seen in the original studies, [45, 75–78], over this range the mean kinetic energy is insensitive to the strength of the surface dissipation. The TKE width decreases as the dissipation strength decreases, as is suggested by the structure of Eq. 2.

By varying these four parameters, I arrive at a relatively good but not optimized representation of all three data sets discussed previously. I first set the surface dissipation to 50% of the default value. This is an arbitrary lower limit, but within the initial range of values allowed by the historical average kinetic energy calculations. This reduction is chosen to reduce the TKE width to be closer to measured values. Varying the scission neck radius and the random-neck parameter to give a much improved reproduction of the evaluated prompt yields leads to the values of $R_{\rm sc} = 1.7$ fm, and the random-neck-rupture parameter of 1.3 fm. The primary effect of varying the inertia scaling is to change the average kinetic energy, with relatively small effects on the mass width and the TKE width. A value of 1.3 for the inertia scaling leads to a mean TKE slightly higher than that for the first data set [113], but below that for the second data set [114]. I show in Figs. 12–17 the results calculated with this adjusted model compared to the three data sets already presented.

The model gives a reasonable representation of many of the gross features of the data sets; but exhibits a much smoother behavior than the prompt yield data near the peak yields. The TKE distribution reproduces the first two moments well, but has a very different skewness than

seen in the measurements. The symmetric yield is well reproduced, but the shape of the symmetric yield valley is narrower than that of the Straede measurements [114]. While the mass yield and the slope of the TKE(A) curve for the first data set [113] are both consistent with a mass resolution of order 3.5 u, the Straede data strongly suggests a resolution of 3.25 from the slope of TKE(A); the mass yield curve is more closely reproduced by a mass resolution of 2.50 u. In all cases, the TKE(A) predictions for roughly 95% of the yield are very well reproduced; there is a significant discrepancy for fragments of masses from about 120 to 130.

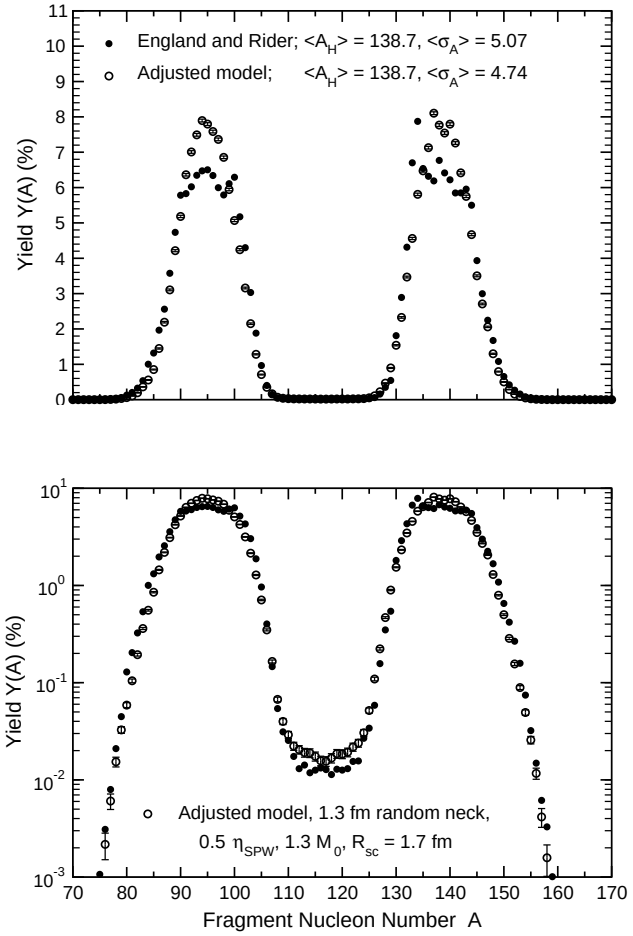


FIG. 12. Calculated post-evaporation fragment yields as a function of fragment mass number A from an adjusted model with reduced dissipation, increased inertia, increased scission neck radius, and a random neck rupture, for the thermal-neutron-induced fission of $^{235}$U, compared to the evaluation of England and Rider [115]. The upper part of the figure has a linear yield scale, while the lower part has a logarithmic yield scale.

As a final investigation of the parameter-dependence of the model results, I discuss the mass resolution parameter, $\Delta A$. The most obvious effect of increasing the mass uncertainty is to increase the width of the heavy (and

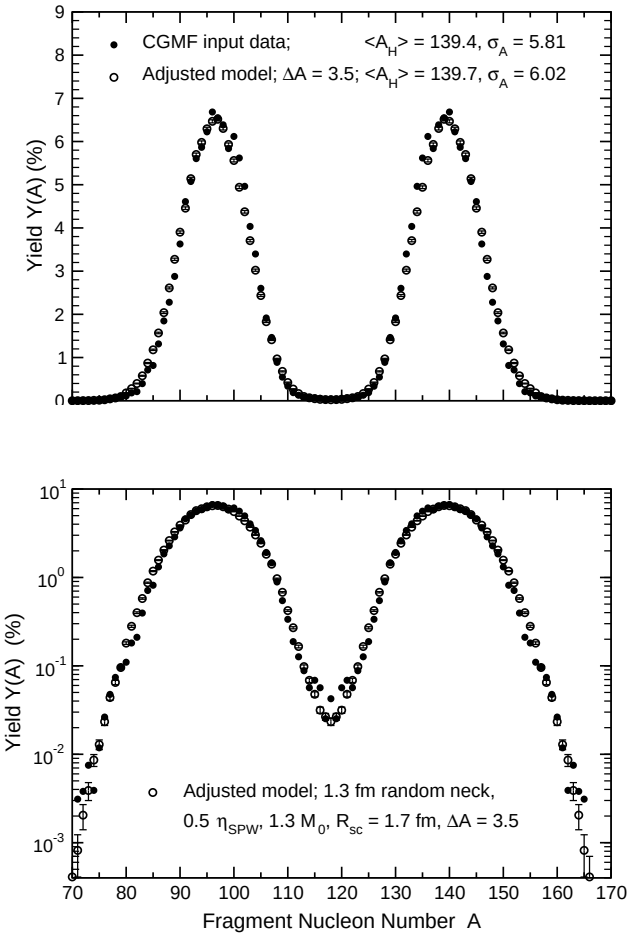


FIG. 13. Calculated pre-evaporation fragment yields as a function of fragment mass number A from an adjusted model with reduced dissipation, increased inertia, increased scission neck radius, a random neck rupture, for the thermal-neutron-induced fission of $^{235}$U, compared to evaluated experimental data [113].

light) mass peak(s), and to increase the apparent symmetric yield. But also, the slope of the TKE(A) curve in its nearly linear region covering the peak of the yield, depends rather sensitively on the mass resolution assumed for the measurement. In Fig. 18, I show the results of the adjusted model previously shown in Fig. 15 for several different values of the mass resolution. The value of 4.0 u, which was initially chosen for the default model because it lay in the middle of the band of estimated uncertainties of resolutions for these types of experiments, turns out to come very close to reproducing the slope of the curve in the region of the heavy mass peak yield, from A = 132 to 160. The value of 3.5 used in Figs. 13 and 15 is chosen as a slightly less optimum compromise value to provide a good representation of both types of data for that data set [113]. The $\Delta A = 3$ calculation seems to reproduce the data near symmetry better, but overestimates the curve more from A = 127 to about 135, as well as having the wrong slope in the region of the max-

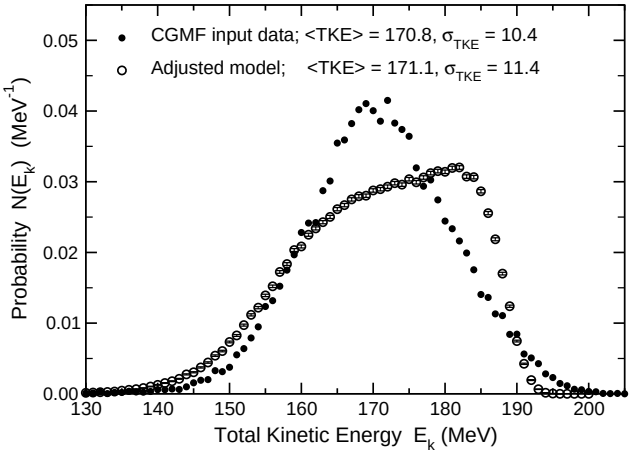


FIG. 14. Calculated pre-evaporation total fragment kinetic energy distribution from the adjusted model for thermal-neutron-induced fission of $^{235}$U, compared to evaluated experimental data [113].

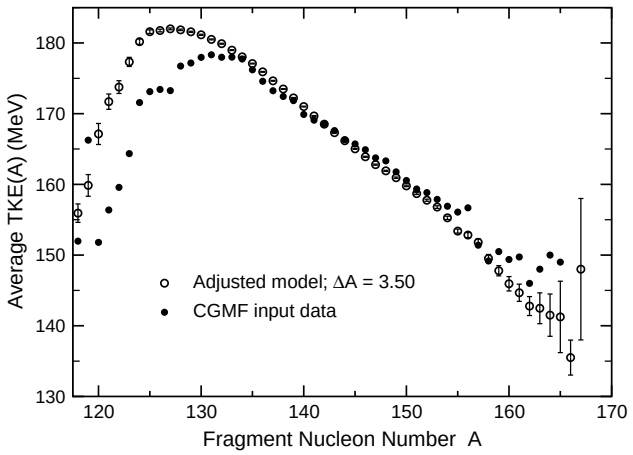


FIG. 15. Calculated pre-evaporation average total fragment kinetic energies as a function of fragment mass number from the adjusted model with a mass resolution $\Delta A = 3.5$ u for thermal-neutron-induced fission of $^{235}$U, compared to evaluated experimental data [113].

imum yield. Similarly, the value of 3.25 seems to give the correct slope for the Straede data plotted in Fig. 17, following the details of the experimental data with more fidelity than one has any right to expect. These calculated trajectories are for a model which was adjusted only to the mass yield, and to the mean and standard deviation of the total TKE. The values of TKE(A) are entirely a prediction of the dynamical model.

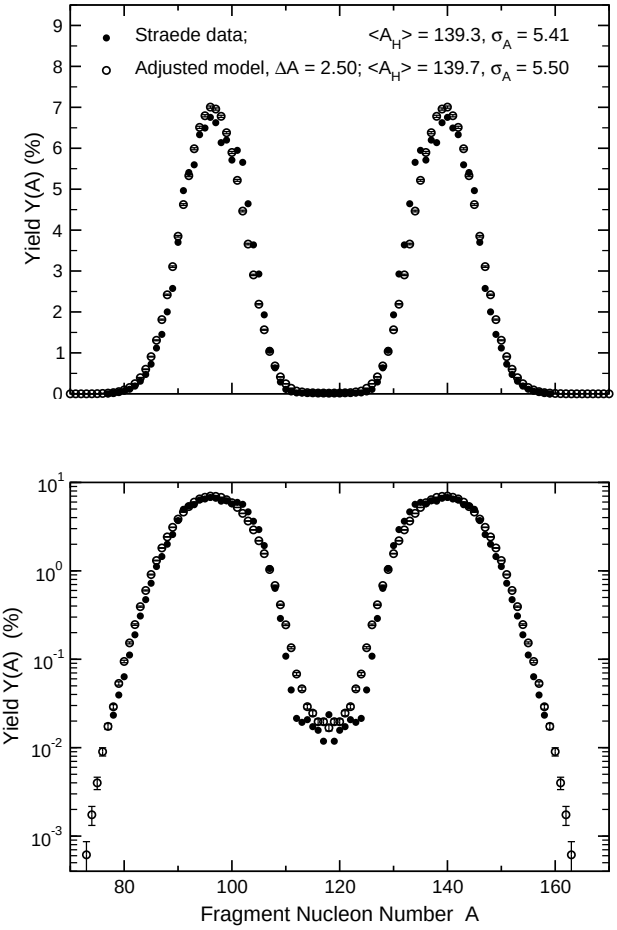


FIG. 16. Calculated pre-evaporation fragment yields as a function of fragment mass number A from the adjusted model with a mass resolution $\Delta A = 2.50$ u for thermal-neutron-induced fission of $^{235}$U, compared to the data of Straede [114]. The calculated trajectories are identical to those used to calculate the results in Fig. 13 except for the use of a different mass-resolution filter. The upper part of the figure shows the yields with a linear scale, while the lower part shows them with a logarithmic scale.

### *4. Higher-energy induced fission*

The fission of $^{235}$U induced by higher energy neutrons is modeled by changing only the initial total energy of the compound nucleus, as was mentioned in Sec. II G 1. i investigate the predictions of the neutron energy dependence of observables using the adjusted model as determined by thermal-neutron fission with no further model adjustments.

One quantity which has been measured for fissile systems is the average TKE as a function of the incident neutron energy. As previously mentioned, there is a systematic uncertainty in the measured mean TKE for thermal neutrons of roughly 1.0–1.5 MeV. Most experimental measurements are normalized to a currently accepted value. The relative energy-dependence of the mean TKE

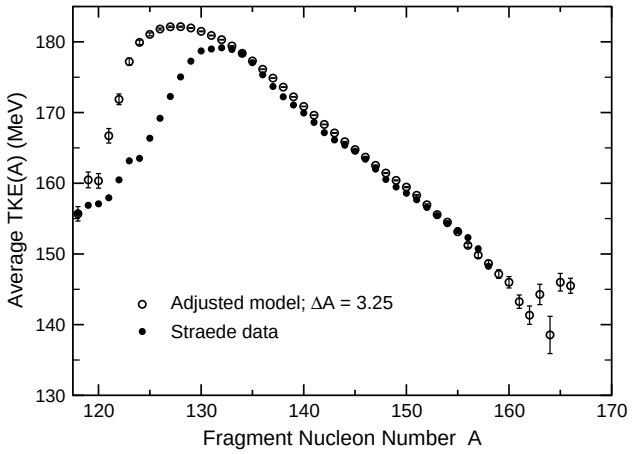


FIG. 17. Calculated pre-evaporation average total fragment kinetic energies as a function of fragment mass number A from the adjusted model with a mass resolution $\Delta A = 3.25$ u for thermal-neutron-induced fission of $^{235}$U, compared to the data of Straede [114]. The calculated trajectories are identical to those used to calculate the results shown in Fig. 15 except for the use of a different mass-resolution filter.

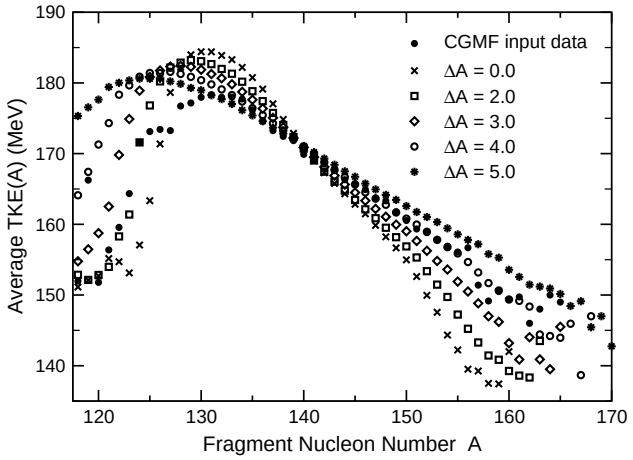


FIG. 18. Calculated pre-evaporation average total fragment kinetic energies as a function of fragment mass number A from the adjusted model for various mass resolutions $\Delta A$ from 0 to 5 u for thermal-neutron-induced fission of $^{235}$U, compared to evaluated data [113]. The 498,254 calculated trajectories are identical to those used to generate the model results shown in Fig. 15, but use different mass-resolution filters.

has much less uncertainty, both as measured, and as modeled. In Fig. 19 I show the predictions of the adjusted model from which 0.2 MeV has been subtracted, to several data sets and evaluations. The model predicts a neutron energy dependence of TKE for $^{235}$U(n,f) which is consistent with the measurements. Both the data and the model exhibit a significant second derivative at energies below about 3 MeV which causes a positive slope at the lowest energies, in contrast to what is measured for $^{239}$Pu(n,f) [117].

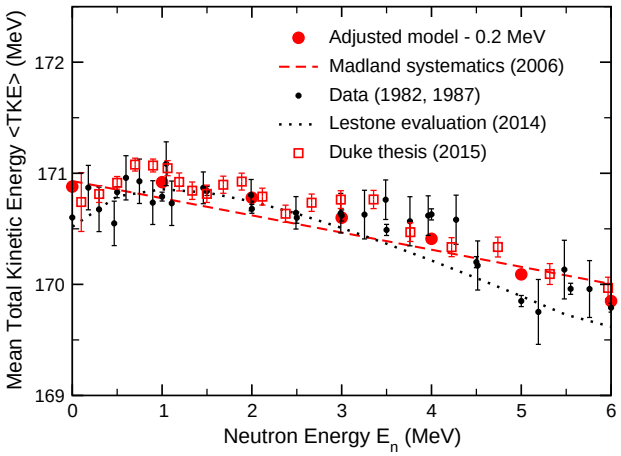


FIG. 19. (Color online) Calculated average pre-evaporation total fragment kinetic energy as a function of incident neutron energy for $^{235}$U(n,f), using the same model as for Figs. 12–17 (solid red circles). The model calculations have 0.2 MeV subtracted to facilitate comparison of the predicted neutron energy dependence with the several data sets. The solid black points are the data used by Madland to derive the linear evaluation shown as a red dashed line [114, 117, 118]. The dotted curve shows the 2014 evaluation of Lestone [119], while the recent measurements of Duke [120] are shown by opoen red squares. The calculated point at 6 MeV is for first-chance fission only, while the data include about 6% second-chance fission.

,

Another quantity which is of much interest because of its practical importance in designing and analyzing systems where the average neutron energy is not in the thermal range is the neutron energy dependence of fragment yields. Deducing the number of fissions occurring in a finite system is often accomplished by measuring the concentration of specific fission-product isotopes whose yield is not strongly dependent upon the energy of the neutrons producing the fissions. Understanding the energy dependence of the yield may be extremely important for analyzing modern reactor designs which utilize non-thermal neutron spectra. If the yield depends upon neutron energy in a way that is not reflected in current data evaluations, the inference of a fission rate could be in error.

Using the same model parameters, I present in Fig. 20 the model predictions for the average logarithmic derivatives of the fragment yields between thermal and 3 MeV neutron energy, compared to linear fits to the neutron energy dependences measured recently [121]. In order to be able to compare to these measurements of prompt fragment yields, the model predictions must be corrected for neutron evaporation. For this purpose, I use the evap-

oration model by Lestone used previously [116], which is tied to the extensive data available on neutron multiplicities and correlations for thermal-neutron-induced fission of $^{235}$U. For the 3 MeV calculations, two different assumptions are made about the distribution of the extra excitation energy between the fragments. In the evaporation assumption labeled 1, the extra excitation energy is allocated proportional to the mass number of the fragment (thermal equilibrium), while the assumption labeled 2 puts all the extra excitation energy into the heavier of the two fragments, weighted by the fragment mass.

Because the yield is always normalized to 200%, any broadening of the yield distribution with neutron energy must necessarily lead to a decrease in the peak yield, which implies a negative logarithmic derivative near the peak yield regions around A = 96 and 140. Similarly, in any lower-yield region, broadening will lead to positive logarithmic derivatives. Both the experiment and the model exhibit these features. Surprisingly, five of the seven isotopes measured in the light-fragment region are consistently predicted by the model. In the heavy peak, the model lies above the data for the mass 130–135 region, reflecting the fine structure in the yield seen in Fig. 9, where the data exhibits local maxima for pre-evaporation A = 135 and 137. It is reasonable to find that an above average yield at thermal energy will lead to a more negative logarithmic derivative. In the heavy-peak region, the three heaviest isotopes are reasonably consistent in the model, while four of the five lighter isotopes have too high derivatives; the A = 127 value is consistent with the model.

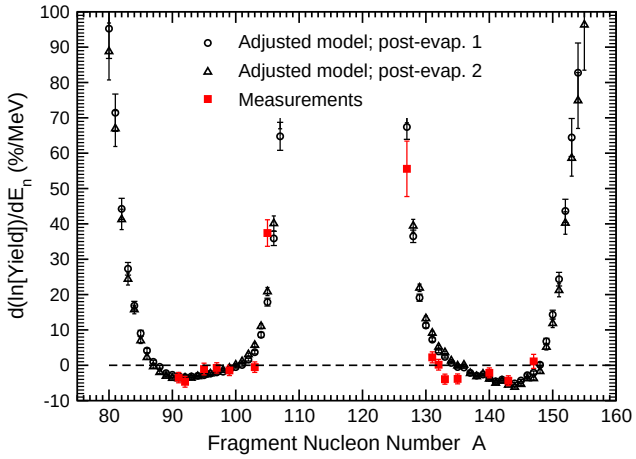


FIG. 20. (Color online) Logarithmic derivative with respect to neutron energy of the post-evaporation fragment yields for $^{235}$U(n,f). The plotted quantity is $\frac{100}{3}[Y(E_3)/Y(E_{\rm th}) - 1]$, where $Y(E_3)$ is the calculated post-evaporation fragment yield for 3 MeV neutron-induced fission, while $Y(E_{\rm th})$ is the calculated yield for thermal-neutron-induced fission of $^{235}$U. The points labeled post-evap 1 (open circles) and post-evap 2 (open triangles) utilize different assumptions about the distribution of excitation energy in the heavy and light fragments for 3 MeV neutron energy. See the text for details. The data points (solid squares) are from linear fits to measured prompt yields as a function of the energy of monoenergetic neutron beams interacting with $^{235}$U targets from Ref. [121].

,

## B. $^{234}$U

The potential-energy surface for $^{234}$U is very similar to that for $^{236}$U. There are three saddle points, occurring at deformations very similar to those for the $A = 236$ isotope. The calculated fission isomer minimum has an energy of 0.27 MeV, the second saddle at $R_1 = 0.52R_0$ has an energy of 3.65 MeV, the third minimum an energy of 1.65 MeV, and the third saddle point at $R_1 = 0.79R_0$ has an energy of 2.66 MeV. The shapes of these equilibrium points are shown in Fig. 5 of Ref. [38]. Following the same procedure as with $^{236}$U, I use a displaced starting point with a value of $R_1 = 0.83R_0$ and an energy of 2.55 MeV.

### 1. *Thermal-neutron induced fission*

I employ the adjusted model with all the same parameters as used for $^{235}$U(n,f) to simulate the thermal-neutron-induced fission of $^{233}$U. The calculated pre-evaporation mass yields are compared to two experimental data sets [122, 123] in Fig. 21, while the post-evaporation yields are compared to the evaluated prompt yields [115] in Fig. 22. While the two data sets from 2E experiments are slightly different in the symmetric yield region, the adjusted model predicts more symmetric yield than either measurement. The post-evaporation symmetric yield is significantly too high in the model.

By arbitrarily discarding 60% of the trajectories entering the symmetric fission valley as discussed in Sec. III 7, the symmetric yield approximates that measured in one of the 2E experiments [122], as well as that in the prompt yield evaluation [115]. There are no tabulated TKE distributions, but the measured mean and standard deviation of the TKE distribution are published in Ref. [124]. The prompt mass yield, the pre-evaporation mass yield, the TKE yield, and TKE(A) for the 40% symmetric-mode model are shown in Figs. 23, 24, 25, and 26, respectively, compared to the appropriate data sets.

The calculated distributions for $^{233}$U(n,f) and $^{235}$U(n,f) show many similarities, but a few surprising differences. The adjusted model determined by consideration of $^{235}$U(n,f) with thermal neutrons is used unchanged for $^{233}$U(n,f) except for the 60% reduction of the symmetric yield. The pre-evaporation mass yield distributions in the peak yield regions are similar, with the model exhibiting smoother behavior than the measurements. The measured prompt yield is significantly flatter than the model, and also exhibits more structure which

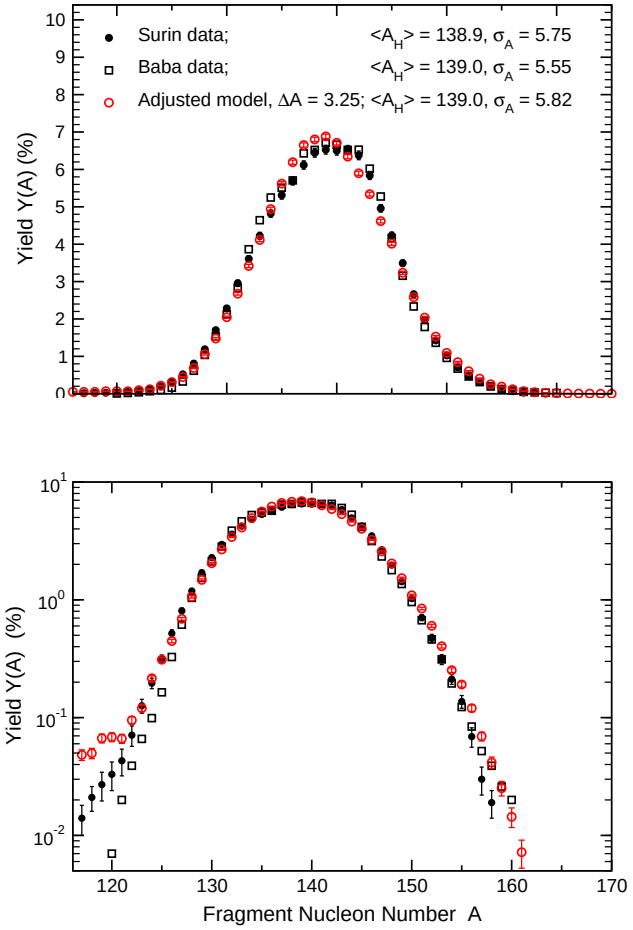


FIG. 21. (Color online)Calculated pre-evaporation fragment yields as a function of fragment mass number A from the adjusted model with a mass resolution $\Delta A = 3.25$ for thermal-neutron-induced fission of $^{233}$U (red circles), compared to two data sets [122, 123]. The upper part of the figure shows the yields with a linear scale, while the lower part shows them with a logarithmic scale.

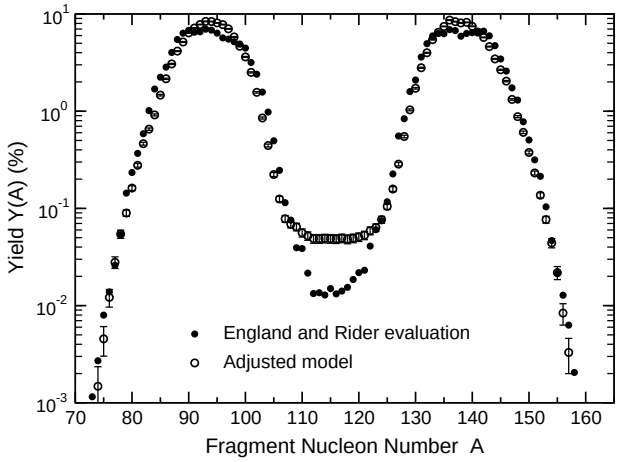


FIG. 22. Calculated post-evaporation fragment yields as a function of fragment mass number A from the adjusted model for thermal-neutron-induced fission of $^{233}$U, compared to evaluated prompt yields [115].

is probably reflective of fragment shell influences; but in both systems, the mean masses and the mass widths are close to those observed. It is most likely a coincidence that the mean TKE for the $^{234}$U system is exactly equal to the data shown. As previously discussed, there are systematic uncertainties in normalizing mean TKE values of the order of 1–1.5 MeV. It is interesting that whatever the normaliztion, the model predicts about 1.5 MeV higher mean TKE for $^{234}$U than for $^{236}$U. Because of the very low yield in the symmetric region, this conclusion is robust in that it does not depend upon the assumption of discarding 60% of the symmetric trajectories. The simulations presented in Figs. 21 and 24 have a mean TKE differing from each other by only 0.05 MeV. For both the U isotopes, the model predicts slightly too much fragment kinetic energy in the very low yield mass region from about A = 121 to 130. The different slopes apparent in the two data sets shown in Fig. 26 suggest that the experiments have different mass resolutions. The mass resolution of 3.25 u seems to provide a good representation of the mass yields, but the slope of the TKE(A) curve suggests a slightly higher mass uncertainty would be optimum. All such speculations would become unimportant if one were to allow for the possibility of an effective mass resolution which depends on the fragment mass, reflecting the differing average number of neutrons evaporated for different fragment masses. As mentioned previously, high quality data with mass resolutions approaching 1 u will be a very useful tool in evaluating the quality of this and other models.

### 2. *Higher-energy induced fission*

I proceed to calculate the mean TKE as a function of neutron incident energy exactly in parallel to the procedure outlined in Sec. IV A 4 for $^{235}$U(n,f). This quantity has not been measured as of this writing. The calculated TKE($E_n$) for this isotope is significantly different than that for $^{235}$U(n,f). The latter, as earlier discussed, has a significant negative second derivative component at lower neutron energies. By contrast, the calculated TKE($E_n$) function for the former system is very nearly linear, with only the hint of a very slight negative second derivative at the lowest energies. The slope of the curve is between -300 and -350 keV/MeV. The slope of the corresponding curve for $^{235}$U(n,f) reaches a maximum negative value above 3 MeV neutron energy of -250 to -280 keV/MeV. This linear dependence is a robust prediction of the model, not depending on the reduction of the number of symmetric trajectories.

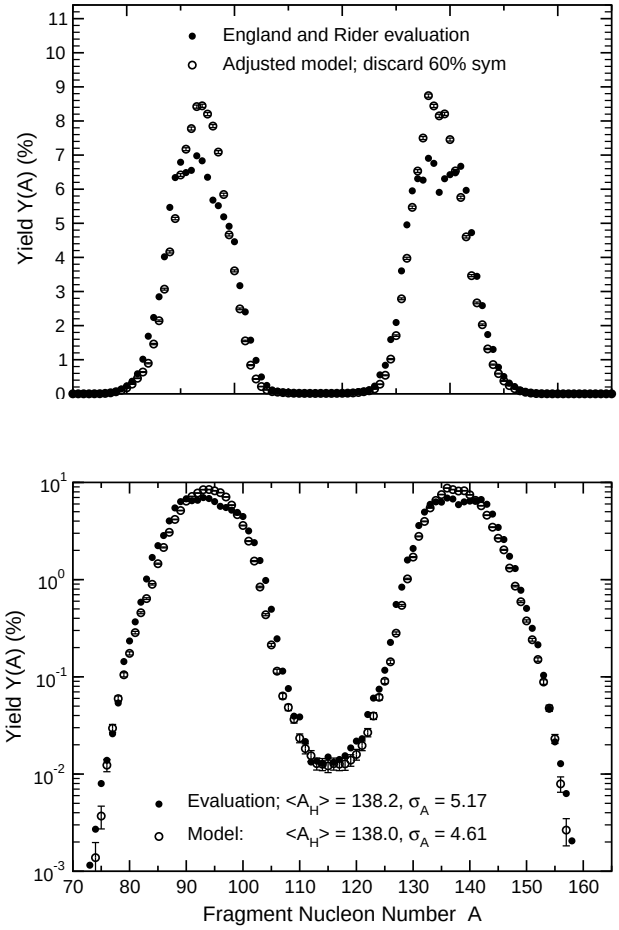


FIG. 23. Calculated post-evaporation fragment yields as a function of fragment mass number A from the adjusted model for thermal-neutron-induced fission of $^{233}$U, with 60% of symmetric trajectories removed, compared to evaluated prompt yields [115]. The upper part of the figure shows the yields with a linear scale, while the lower part shows them with a logarithmic scale.

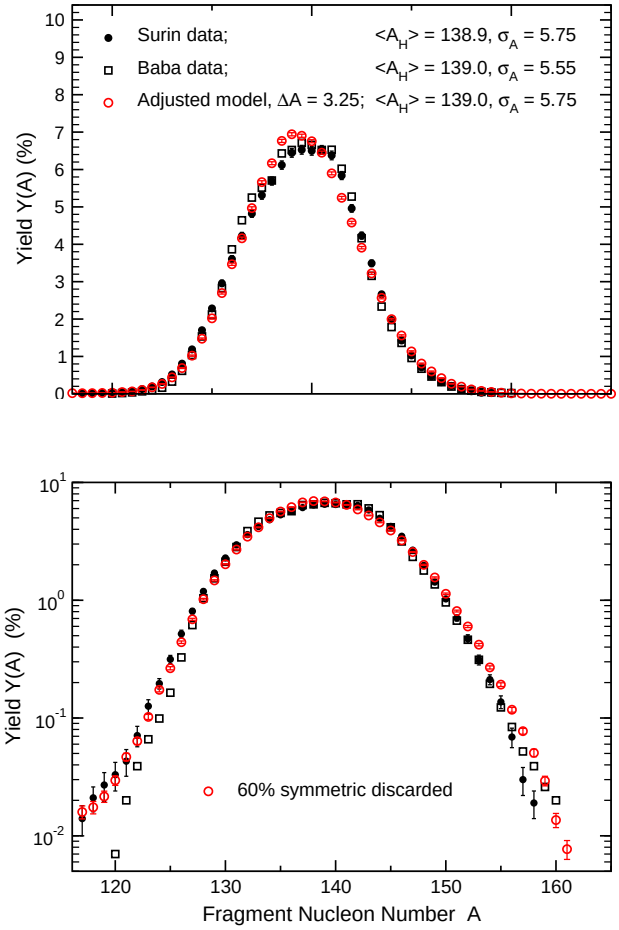


FIG. 24. (Color online) Calculated pre-evaporation fragment yields as a function of fragment mass number A from the adjusted model with 60% of the symmetric trajectories removed, and a mass resolution $\Delta A = 3.25$ for thermal-neutron-induced fission of $^{233}$U, compared to two data sets [122, 123]. The upper part of the figure shows the yields with a linear scale, while the lower part shows them with a logarithmic scale.

### C. $^{240}$Pu

For modeling $^{239}$Pu(n,f), I proceed much in the same way as for $^{235}$U(n,f). In Fig. 28 I show the outermost (second) minimum and saddle point for $^{240}$Pu, along with the symmetric and asymmetric valleys and the ridge between them. This nuclide does not have a third asymmetric barrier in the macroscopic-microscopic potential model I use. Otherwise, the nature of the valleys is very similar to those shown in Fig. 3 for $^{236}$U. There is one very important difference, however. In the case of $^{236}$U, the ridge near the starting point in the asymmetric fission valley has an energy very near the total available energy for thermal neutron-induced fission, and it rises for initial elongations outside the third saddle point. The system then has a very low probability of making its way into the symmetric valley. For $^{240}$Pu, by contrast, the much more compact starting configuration has a significantly lower ridge separating it from the symmetric valley for shapes more elongated than the starting configuration, and because the total energy available for thermal-neutron-induced fission is significantly greater than the height of the ridge, the system has a much higher probability of passing between the valleys in the early part of the time evolution than does the $^{236}$U system. Just as in Fig. 3, the last point along the asymmetric valley at $R_1 = 1.5$ has no neck remaining.

#### 1. *Thermal-neutron induced fission*

For thermal-neutron-induced fission of $^{239}$Pu, I start the system out using similar approximations as used for $^{235}$U(n,f). In order to avoid the slight local maximum in

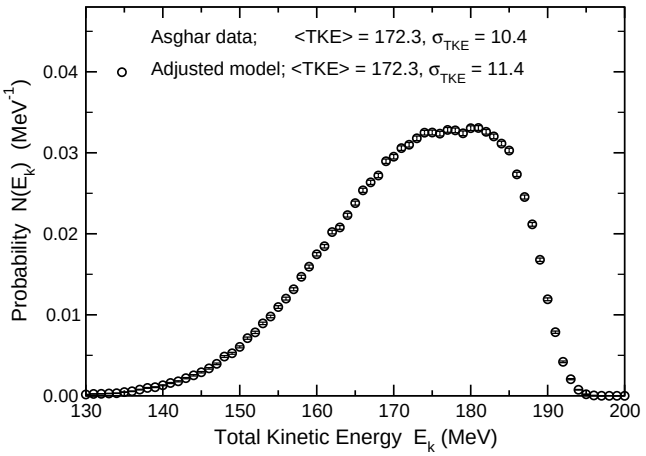


FIG. 25. Calculated pre-evaporation total fragment kinetic energy distribution from the adjusted model for thermal-neutron-induced fission of $^{233}$U, for which the only data available are the mean and standard deviation of the experimental distribution [124].

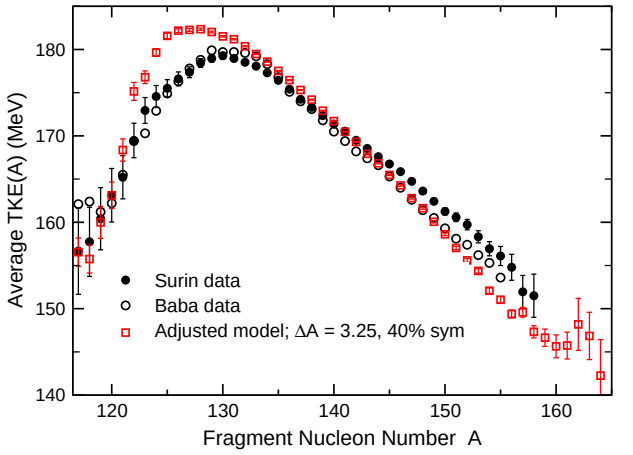


FIG. 26. (Color online) Calculated pre-evaporation average total fragment kinetic energies as a function of fragment mass number from the adjusted model with 60% of the symmetric trajectories discarded, and a mass resolution $\Delta A = 3.25$ u for thermal-neutron-induced fission of $^{233}$U, compared to two data sets [122, 123].

the potential along the asymmetric valley visible in Fig. 28, which causes a great increase in the average time for a successful fission trajectory, I start the system farther away from the outer saddle. The outer saddle point has a value of $R_1 = 0.58$, with the energy 2.68 MeV. The starting point has $R_1 = 0.85$ with an energy of 0.21 MeV. Fig. 29 shows the fragment yields calculated using the same adjusted model used for the $^{236}$U system, compared to data. For $^{240}$Pu, a slightly larger scission neck radius of 1.8 fm is used. There is too much symmetric fission yield in the model calculation, possibly in part due to the rea-

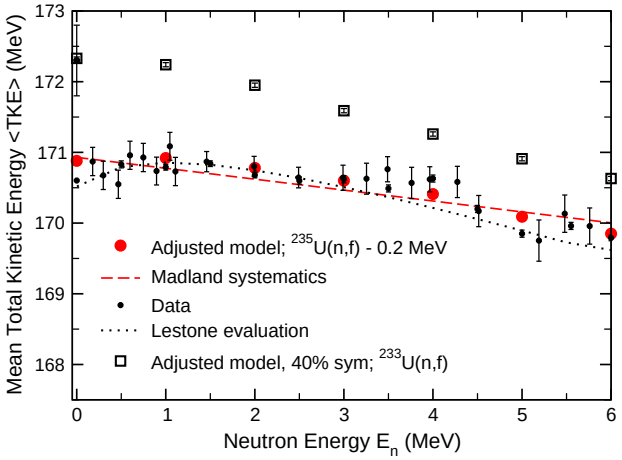


FIG. 27. (Color online) Similar to Fig. 19. The solid data points, the Madland systematics [117], the Lestone evaluation [119], and the solid circles (model) are the same as in that Figure, and apply to $^{235}$U(n,f), while the open squares are calculated using the same adjusted model, with 60% of the symmetric trajectories discarded, for $^{233}$U(n,f). The data point for $^{233}$U(n,f) at thermal energy is from Ref. [124]. The calculated points at 6 MeV are for first-chance fission only, while the data include about 6% second-chance fission.

,

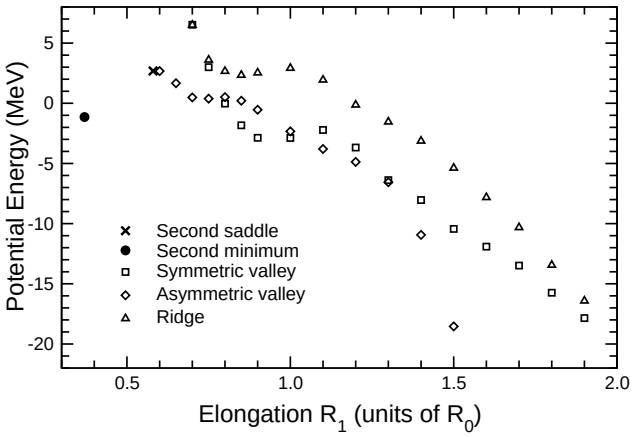


FIG. 28. The calculated energies of the second minimum, the second (outermost) saddle point, the mass-symmetric and mass-asymmetric valleys, and the ridge between them as functions of the coordinate $R_1$ for $^{240}$Pu.

sons discussed previously. In order to get the yield curve to more closely represent the yield in the symmetric region, I arbitrarily remove 85% of the symmetric trajectories, as discussed in Sec. III 7. The calculated prompt yields are shown in Fig. 30, while the pre-evaporation yields are shown in Fig. 31. The TKE yield from the model with reduced symmetric yield is compared to data in Fig. 32, and the predicted TKE(A) is shown in Fig.

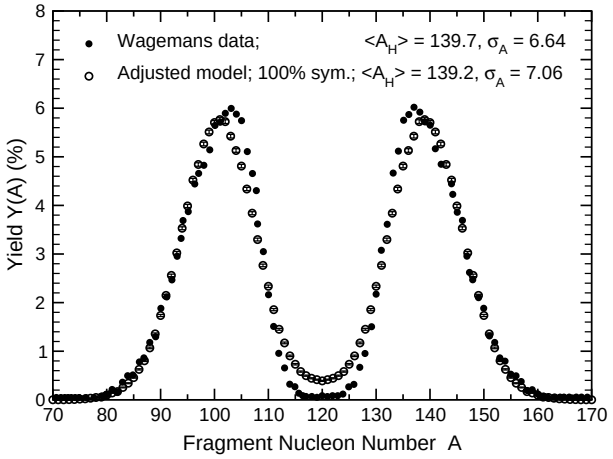


FIG. 29. Calculated pre-evaporation fragment yields for thermal-neutron-induced fission of $^{239}$Pu as a function of fragment mass number A from the adjusted model with a mass resolution $\Delta A = 3.50$, compared to experimental data [125], with a linear scale.

33. In decided contrast for the $^{236}$U results, there is a significant deviation of the details of the mass yield in the peak-yield region for $^{240}$Pu. Although the model with the parameters set from the U case gives the first and second moments of the mass peaks very well, the data has a much larger third moment than the model, even though the model does show more third moment than it did for U. The pre-evaporation mass yield in the symmetric region is slightly too high, even though the post-evaporation yield is well represented by the model with 85% of the symmetric trajectories removed. The model TKE yields, although the first and second moments are close to the data, exhibits a large asymmetry, as was seen in $^{236}$U. It is interesting that the TKE(A) is well reproduced for all fragment masses less than about 155, which accounts for about 97% of the total yield. The large deviations seen for $A < 130$ in the U isotopes are not present, while the model underestimates the TKE for fragments of masses 155–167.

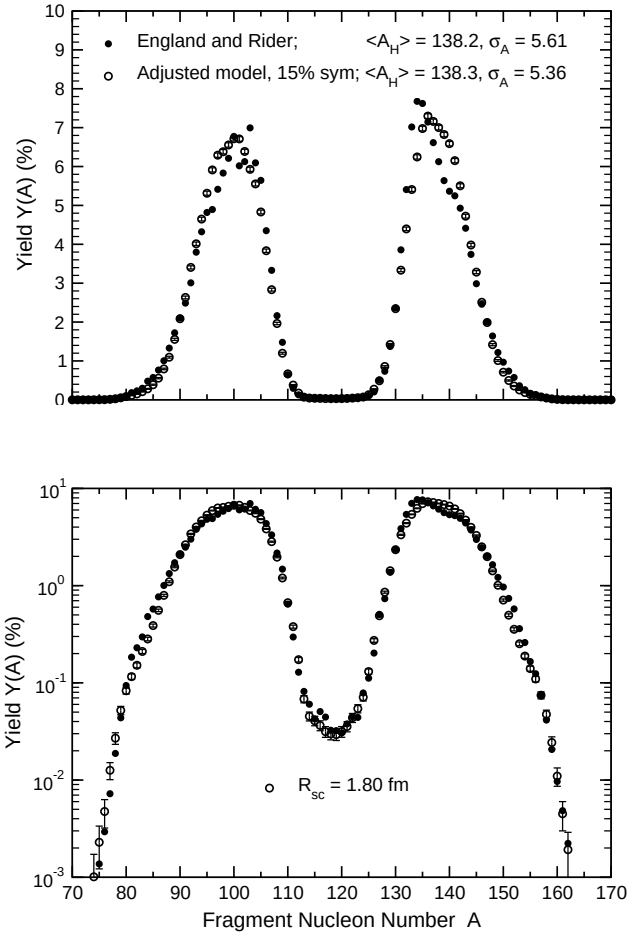


FIG. 30. Calculated post-evaporation fragment yields as a function of fragment mass number A from the adjusted model for thermal-neutron-induced fission of $^{239}$Pu, compared to the evaluation of England and Rider [115]. The model uses the same parameters as for $^{235}$U (n,f) except for a scission neck radius of 1.8 fm instead of 1.7 fm. 85% of symmetric trajectories have been discarded to more closely approximate the symmetric yield. The upper part of the figure shows the yields with a linear scale, while the lower part shows them with a logarithmic scale.

### 2. *Higher-energy induced fission of $^{239}$Pu*

The process of simulating fission induced by neutrons of higher energies proceeds just as outlined for $^{235}$U(n,f). The same starting coordinates are used, with the total energy available increased by the kinetic energy of the incident neutron giving rise to a larger average starting momentum. I show in Fig. 34 the calculated neutron energy dependence for first-chance fission, compared to the data of Akimov [126] and the linear evaluation by Madland [117]. The model, which has only been changed from that used for $^{235}$U(n,f) by the removal of 85% of the symmetric trajectories, shows a linear dependence with very little evidence of a second derivative, but with a slope significantly less than that in the data and evaluation. The latter has a slope of about -350 keV/MeV, while the model has a slope of about -100 keV/MeV. A second model calculation is shown in the Figure, which uses the same model parameters, but without discarding any symmetric trajectories. This calculation gives too much symmetric yield, see Fig. 29, but has a slope closer to that observed, about -230 keV/MeV.

In Fig. 35, I show the calculated neutron-energy dependences of the yields for $^{239}$Pu(n,f), compared to measurements [121]. The calculations are performed in exactly the same way as those presented in Fig. 20 for $^{235}$U(n,f). In this case, the model results differ significantly from most of the measurements. It is quite possible that there

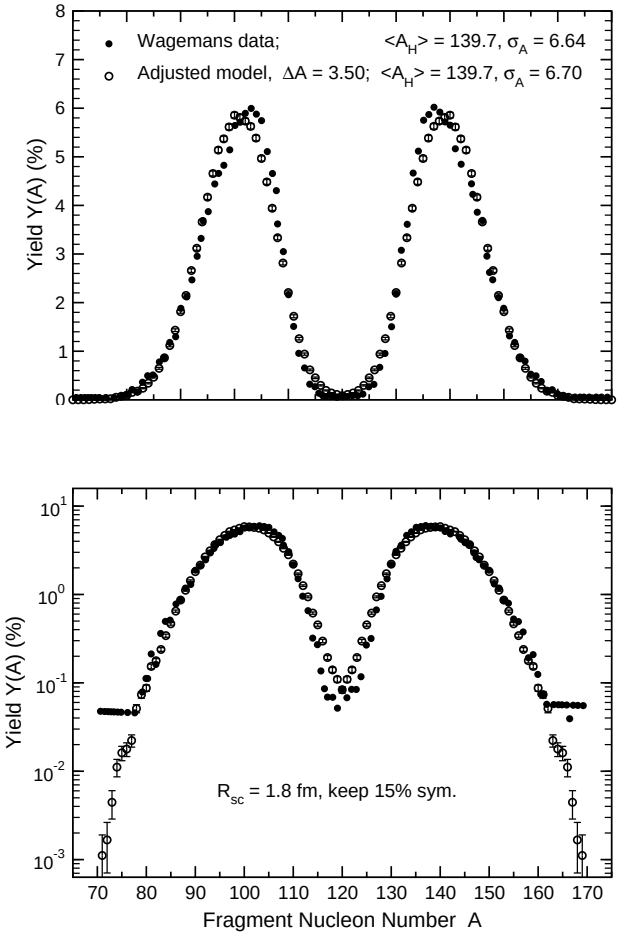


FIG. 31. Calculated pre-evaporation fragment yields as a function of fragment mass number A from the adjusted model with with 85% of the symmetric yield discarded, for thermal-neutron-induced fission of $^{239}$Pu, compared to experimental data [125]. The scission neck radius of 1.8 fm is used instead of 1.7 fm for the case of $^{235}$U (n,f) shown previously, while the mass resolution $\Delta A = 3.50$ u. The upper part of the figure shows the yields with a linear scale, while the lower part shows them with a logarithmic scale.

remain some unidentified systematic errors in the data. Since fission yields are always normalized to 200%, it is necessary that slopes in the regions of peak yields must become negative if there is any broadening of the mass-yield peaks. Only one of the 14 measured slopes for $^{239}$Pu is negative, a highly unlikely result. As shown in Fig. 20, for $^{235}$U(n,f), 12 of 15 experimental slopes are negative, as would be expected for a measurement which can only be performed for mass values with yields of roughly 0.1% or higher, thus sampling mostly masses in the neighborhood of the yield peaks. While there is reason to expect that the data may not be correct for all mass values, that of course does not mean that the model is necessarily right for this fissioning isotope.

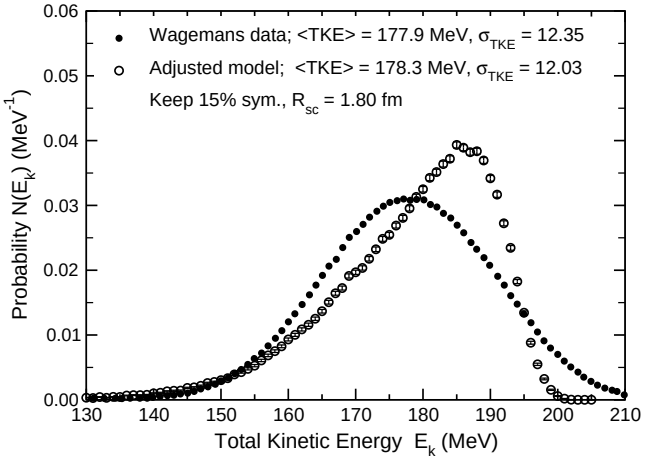


FIG. 32. Calculated pre-evaporation total fragment kinetic energy distribution from the adjusted model for thermal-neutron-induced fission of $^{239}$Pu, compared to the experimental data of Wagemans [125].

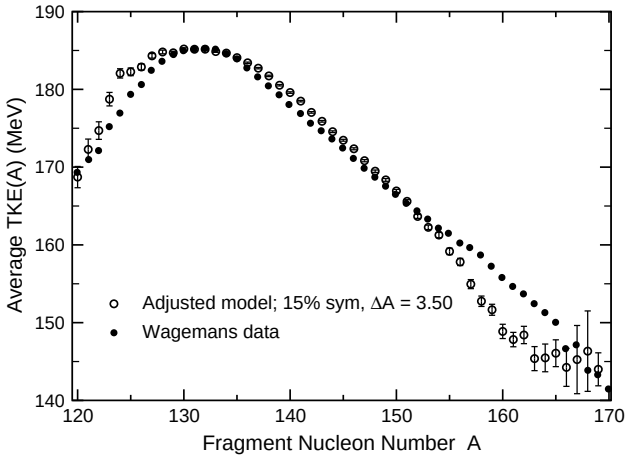


FIG. 33. Calculated pre-evaporation average total fragment kinetic energies as a function of fragment mass number from the adjusted model with 85% of symmetric trajectories discarded, and with a mass resolution $\Delta A = 3.5$ u, for thermal-neutron-induced fission of $^{239}$Pu, compared to the experimental data of Wagemans [125].

### *3. Spontaneous fission of $^{240}$Pu*

To model spontaneous fission of $^{240}$Pu, I employ the crude approximation described in Sec. II G 2 to define a distribution of barrier exit-point coordinates, from which the system is started at rest. I use the same model parameters as used for the thermal-neutron-induced fission of $^{239}$Pu. I use gaussian coordinate distributions with the standard deviations found in the procedure described in Sec. II G 2. The first 3QS coordinate $\sigma_1$ is varied to make the starting potential within 0.5 MeV of the ground-state

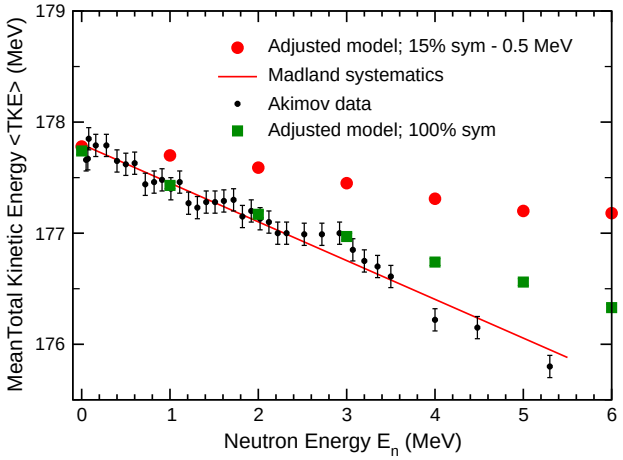


FIG. 34. (Color online) Calculated average pre-evaporation total fragment kinetic energy as a function of incident neutron energy for $^{239}$Pu(n,f), using the same model as for Figs. 30–33 (solid red circles). The model calculations have 0.5 MeV subtracted to facilitate comparison of the predicted neutron energy dependence with the data set. The solid black points are the data used by Madland to derive the linear evaluation shown as a red solid line [117, 126]. The same model with all symmetric trajectories included, used to calculate the results shown in Fig. 29, predicts the energy dependence shown by the green solid squares. The calculated points at 6 MeV are for first-chance fission only.

,

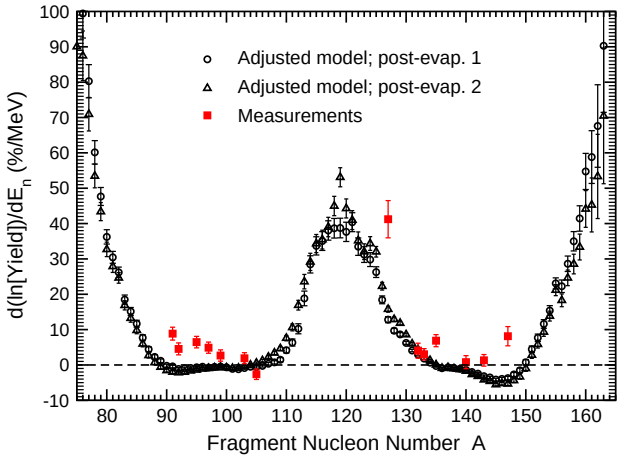


FIG. 35. (Color online) Same as Fig. 20, for $^{239}$Pu(n,f).

,

energy of -1.83 MeV [37]. However, no trajectories starting in the asymmetric valley are discarded. I find a symmetric yield consistent with the available data by starting 0.5% of the trajectories in the symmetric valley. Because of trajectory abnormal terminations, actually only 0.27% of the trajectories (about half of those started in the symmetric valley) actually contribute to the distributions. This small admixture gives a good representation of both the uncertain symmetric yield, and the measured TKE(A) for symmetric fragments. The TKE distribution is changed almost not at all by leaving out this small symmetric component. To summarize, the adjusted model determined earlier from $^{235}$U amd $^{239}$Pu(n,f) by thermal neutrons is used with only the mass resolution and the symmetric admixture determined from the mass yield data.

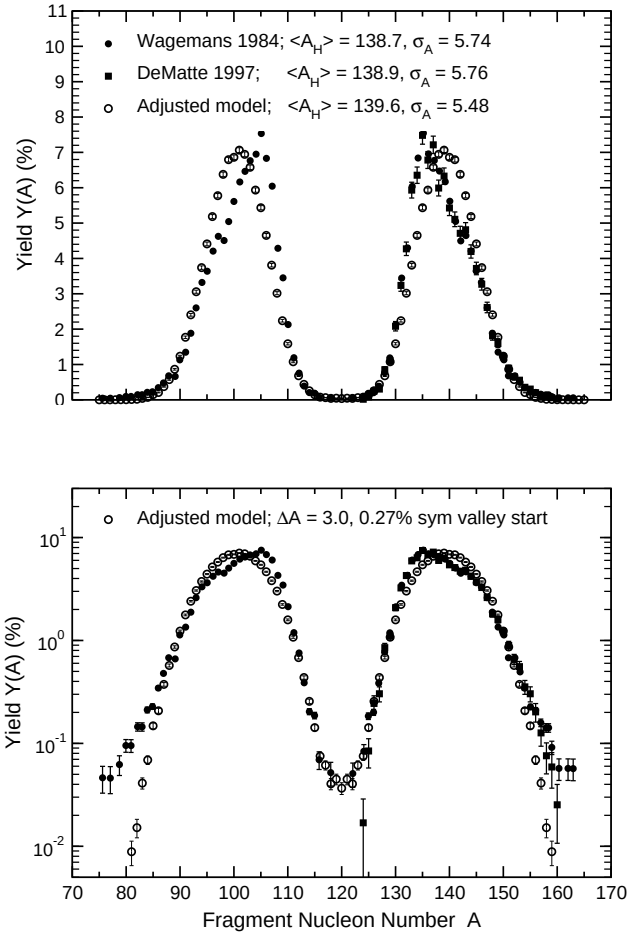


FIG. 36. Calculated pre-evaporation fragment yields as a function of fragment mass number A from the adjusted model with with 0.27% of the trajectories starting in the symmetric valley, while the remainder start in the asymmetric valley, for spontaneous fission of $^{240}$Pu, compared to experimental data [125], [127]. The mass resolution applied to the model is $\Delta A = 3.0$ u. The upper part of the figure shows the yields with a linear scale, while the lower part shows them with a logarithmic scale.

The calculated mass yields are compared to two data sets in Fig. 36. The mean mass of the heavy-mass peak is reduced only very slightly compared to the thermal-neutron prediction, while the width, which does depend upon the assumed mass resolution, is reduced by more than the roughly 1 u by which the experimental mass width is reduced compared to that for thermal fission. By

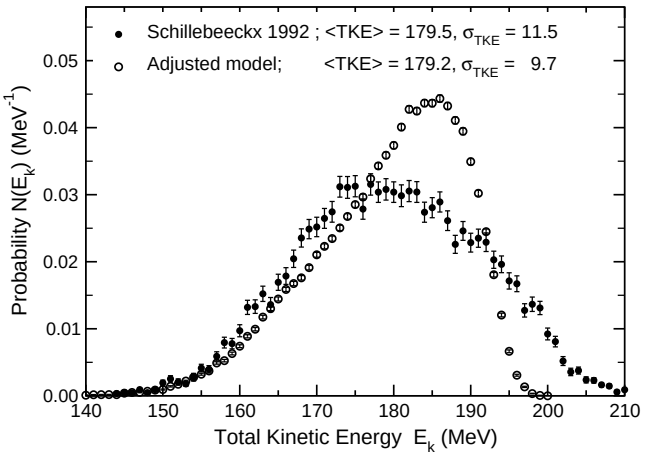


FIG. 37. Calculated pre-evaporation total fragment kinetic energy distribution from the adjusted model for spontaneous fission of $^{240}$Pu, compared to the experimental data of Schillebeeckx [128].

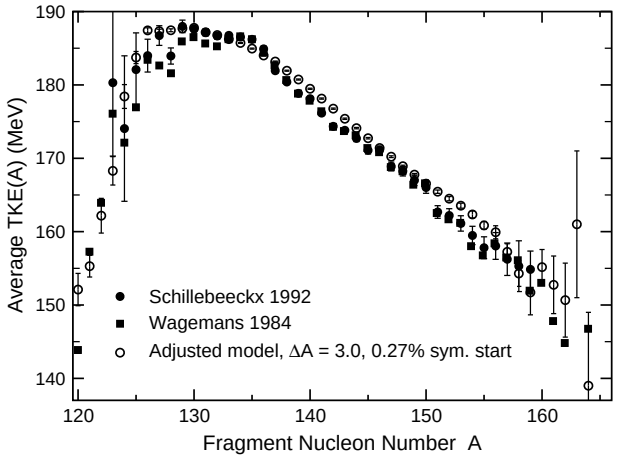


FIG. 38. Calculated pre-evaporation average total fragment kinetic energies as a function of fragment mass number from the adjusted model with 0.27% of trajectories starting in the symmetric valley, and with a mass resolution $\Delta A = 3.0$ u, for spontaneous fission of $^{240}$Pu, compared to the experimental data of Wagemans [125] and Schillebeeckx [128].

employing a mass resolution $\Delta A$ of 3.0 MeV, the model has the same width as the data. The very skewed distribution seen in the data for thermal fission is even more pronounced for spontaneous fission. Even though the model exhibits a small amount of skewness, it totally fails to reproduce the details seen in the data. Although the data uncertainty gets fairly large in the mass 80 and 160 regions, the model appears not to model the fall-off seen in these extreme mass regions. This is in contrast to the thermal-neutron distributions, for which the model gives a very good representation to the largest masses for which the data is reliable, while providing too much symmetric yield for the pre-evaporation distribution (see Fig. 31), and giving a good reproduction of both the symmetric and large-mass yields for the post-evaporation evaluated data (Fig. 30).

The TKE distribution is shown in Fig. 37. The model predicts well the 1–1.5 MeV shift of the mean TKE to higher energy for spontaneous fission, [125], [128]. while predicting a large reduction of the standard deviation of the TKE distribution, which experimentally is measured to be close to that for thermal-neutron-induced fission [125], or only slightly reduced [128]. Finally, it is somewhat surprising that the predicted TKE(A) distribution shown in Fig. 38 for a mass resolution of 3.0 u, essentially exactly fits the data to the accuracy with which it has been measured.

### D. Spontaneous fission of $^{252}$Cf

The $^{252}$Cf potential-energy surface is quite different from that of $^{240}$Pu, having four more protons and eight more neutrons. It does possess a double-peaked barrier, but this is more compact than that for Pu; the second minimum at $R_1 = 0.37R_0$ has a calculated energy of -1.20 MeV, while the second barrier at $R_1 = 0.45R_0$ has an energy of 2.36 MeV. The FRLDM ground-state energy is -3.08 MeV [37]. There is a well-defined asymmetric valley extending from $R_1 = 0.65$ to 1.40 which vanishes before $R_1 = 1.5$, even though the neck radius is still 2.5 fm at the last point at $R_1 = 1.4$. The symmetric valley does not exist inside of $R_1 = 0.85$, but extends out beyond $R_1 = 1.9$, as it does for the lighter isotopes considered. Between $R_1 = 0.85$ and 1.40 there are from zero to three additional valleys, most of which are not persistent in the sense that their character is stable over several $R_1$ values. The conclusion from this is that there is a significantly larger range of elongations over which fissioning nuclei evolve, and the potential energy is 'flatter' in the transverse directions than one would infer for $^{236}$U, e.g. from Fig. 8 of [60].

Just as in the case of $^{240}$Pu(SF), I start the trajectories at an ensemble of starting configurations with average coordinates as determined following Sec. II G 2; that is, at the approximate barrier exit point in the asymmetric fission valley. I independently sample from gaussian distributed increments to all the coordinates as determined from the coordinate standard deviations found while determining the exit-point coordinates. The $\sigma_1$ coordinate is varied to restrict the potential energy of the starting point to within 0.5 MeV of the ground-state energy of -3.08 MeV. All trajectories are started at rest. The scission neck radius $R_{\rm sc} = 2.0$ fm is used.

The calculations, corrected for neutron evaporation [116], are compared to the England and Rider evaluated prompt yields [115] in Fig. 39. In addition to the exhibited incorrect first and second moments of the heavy-fragment peak, this calculation also has an average prescission TKE of 188.1 MeV, compared to the experi-

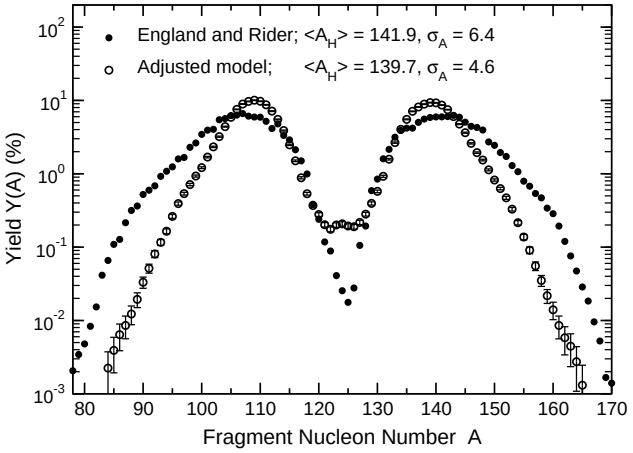


FIG. 39. Calculated post-evaporation fragment yields as a function of fragment mass number A from the adjusted model, for spontaneous fission of $^{252}$Cf, compared to an evaluation [115]. All trajectories start in the neighborhood of the exit point in the asymmetric valley, and the scission neck radius is 2.0 fm, compared to 1.8 fm used for Figs. 36–38

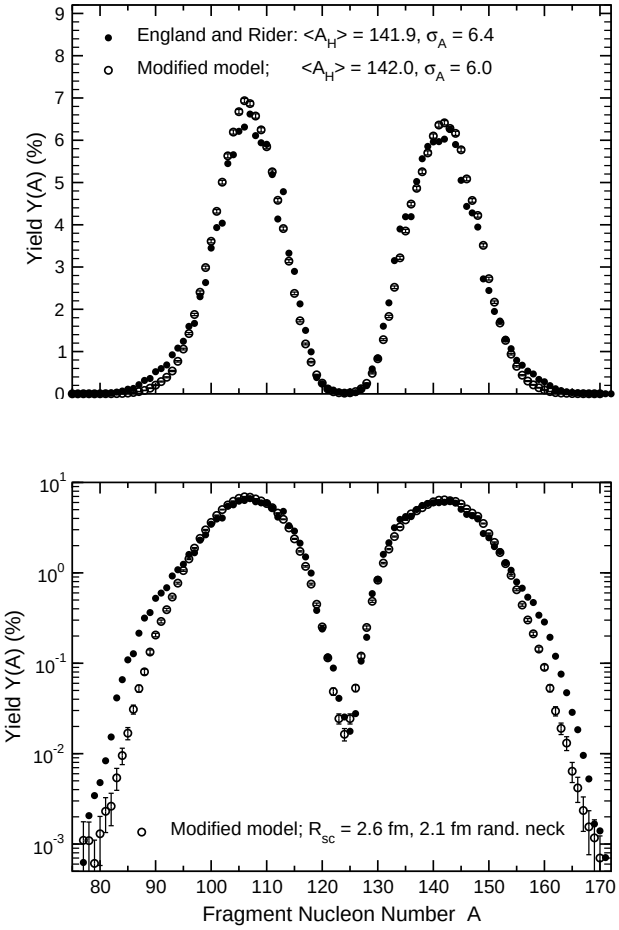


FIG. 40. Calculated post-evaporation fragment yields as a function of fragment mass number A from the 'modified model', for spontaneous fission of $^{252}$Cf, compared to an evaluation [115]. The dissipation and inertial parameters are the same as used in the adjusted model, but a scission neck radius of 2.6 fm, and a neck rupture parameter of 2.1 fm are used. The upper part of the figure shows the yields with a linear scale, while the lower part shows them with a logarithmic scale.

mental value of 183.6 MeV.

A general feature of the actinide potential-energy surfaces investigated so far in this study is that the asymmetry of the fission valley decreases as the elongation $R_1$ increases. By decreasing the average elongation at scission by increasing the scission neck radius, and increasing the value of the random-neck-rupture parameter from its value of 1.3 fm which worked reasonably well for both U and Pu, and also eliminating **all** trajectories in the symmetric valley, it is possible to represent more accurately the gross properties of the mass yields. The remaining mass splits near symmetry are due to the random neck rupture process only. The post-evaporation yields from this 'modified model' are compared to the evaluation [115] in Fig. 40. The pre-evaporation yields from this 'modified model' are compared to one evaluation [113] in Fig. 41. The TKE distribution is shown in Fig. 42, while the TKE(A) results are shown in Fig. 43.

The need to modify the scission details to get a somewhat reasonable representation of the mass yields means that the model at this stage of development is not predictive of yield details for some systems, despite the very good prediction illustrated in Fig. 6, at least for the case of spontaneous fission. Whether this is also true for induced fission is not yet known, because of the limited mass region for which induced fission calculations have been completed. This situation was seen in a less drastic way for the relatively minor changes needed to better represent the yields for $^{233}$U(n,f), $^{239}$Pu(n,f), and $^{240}$Pu(SF) presented previously. But I show these results from the modified model because of the rather remarkable representation of the average TKE which is achieved by **only** adjusting the model to the mass yield, and then calculating the TKE values which result. When calculating the $^{252}$Cf(SF) <TKE> for the original adjusted model, I find 188.1 MeV, with a standard deviation of 12.4. For the 'modified' model, adjusted only to the mass yields, the calculated value is 183.7 ± 9.5 MeV, while the experimental value is 183.6 ± 10.9 MeV. an error of less than 0.1% for the first moment. In the case of $^{252}$Cf(SF), the second moment is underestimated by roughly 15%, as was the case for $^{240}$Pu(SF). This is a similar magnitude of discrepancy, but with the opposite sign to the case for induced fission. The TKE(A) results are close to the measurements for the peak-yield region, but deviate more significantly than was the case for U and Pu in both the symmetric region, and in the very heavy mass region above about A = 160 and the corresponding low-mass region. In Figs. 41 and 43, I show the effect of varying the mass resolution from 3.0 to 4.0 u. The 4.0 mass uncer-

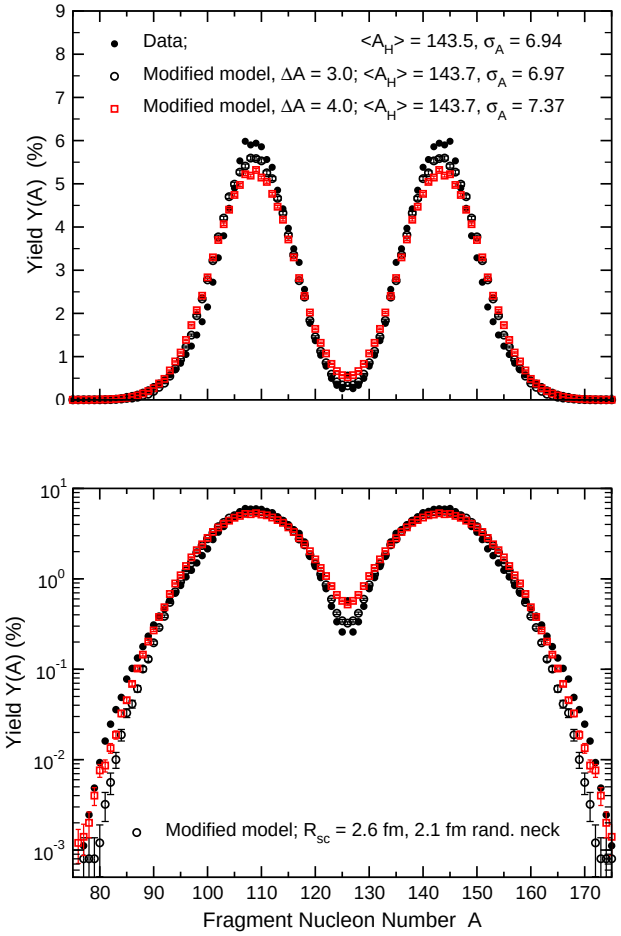


FIG. 41. (Color online) Calculated pre-evaporation fragment yields as a function of fragment mass number A from the 'modified model', for spontaneous fission of $^{252}$Cf, compared to experimental data [113]. The dissipation and inertial parameters are the same as used in the adjusted model, but a scission neck radius of 2.6 fm, and a neck rupture parameter of 2.1 fm are used. The results with two different mass resolutions are shown; $\Delta A = 3.0$ u (black circles) and 4.0 u (red squares). The upper part of the figure shows the yields with a linear scale, while the lower part shows them with a logarithmic scale.

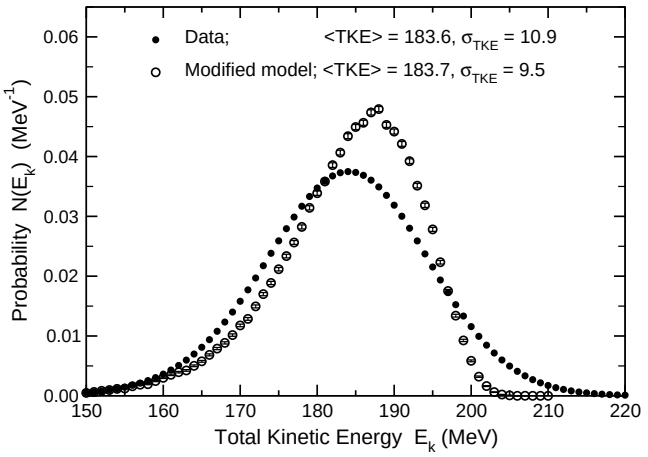


FIG. 42. Calculated pre-evaporation total fragment kinetic energy distribution from the modified model for spontaneous fission of $^{252}$Cf, compared to experimental data [113].

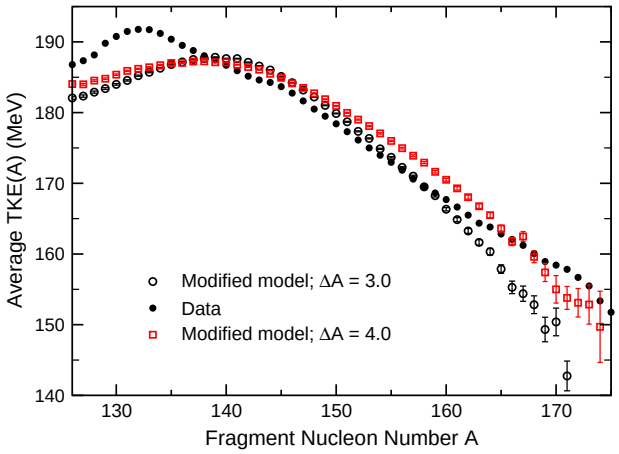


FIG. 43. (Color online) Calculated pre-evaporation average total fragment kinetic energies as a function of fragment mass number from the modified model with a mass resolution $\Delta A = 3.0$ u (black circles) and 4.0 u (red squares), for spontaneous fission of $^{252}$Cf, compared to experimental data [113].

tainty gives an overall better representation of TKE(A), but the details in the case of either mass resolution are not as well represented as they were for $^{240}$Pu(SF). The larger mass uncertainty destroys the approximate representation of the mass yield in the symmetric-mass region achieved with $\Delta A = 3.0$. By contrast, the larger uncertainty comes much closer to the yield in the $A > 160$ region. For the prompt yields in Fig. 40, the values of $R_{sc}$ and the random neck parameter, and the discarding of all the symmetric trajectories, which give a good representation of both the symmetric yield and the peak-yield mass regions, deviates very significantly from the pronounced shoulders seen in the evaluation for $A < 94$ and $A > 156$. It is useful to keep in mind that only about 2% of the total yield lies above A = 156 in the prompt yield. It is interesting that so many gross features of the mass and energy distributions come quite accurately from a model which ignores all the physics inherent in the effect of barrier penetrability on the distribution of starting points for fission trajectories. One could speculate that the pronounced shoulders in the yield at large A might be from a feature in the potential surface that is not found in the macroscopic-microscopic model employed here, or some variation in a more accurate estimation of the barrier-penetration probability that favors large asymmetries more than the simple approximation

employed here, or some other not-understood factor.

## V. DISCUSSION

### A. Summary

This paper presents a dynamical study of fission of actinide nuclei, both spontaneous and induced by neutrons of energies of up to the threshold for second-chance fission. The model represents a merger of a simple classical dissipative dynamical model with a macroscopic-microscopic potential-energy model. The potential model has been fit to ground-state nuclear properties, and has previously been shown to be successful in predicting fission-barrier heights throughout the nuclear chart and the complex structure of actinide fission barriers [39, 40]. It is used in this dynamical model unchanged from its static form. The dynamical model consists of a scaled hydrodynamical inertia and a scaled one-body dissipation model which was previously shown to predict mean fragment kinetic energies when used in a non-stochastic dynamical model for mean trajectories. A very simple model for the thermal properties of nuclei is employed, with the potential surface remaining unchanged for the temperatures encountered. The model employs a minimal number of physical parameters which are varied to optimize the reproduction of mass yields, while only one parameter has been varied to reproduce the average fragment TKE for $^{236}$U, and is used unchanged for all the other systems studied. A very simple model of the interactions of separating deformed fragments is used to improve the modeling of the fragment kinetic energy over simple estimates based only on the Coulomb interaction energy at scission.

The model, with essentially no data on fission entering its definition, does a very good job of predicting a number of observables, such as the mean mass asymmetry seen in fission, the approximate width of the mass yields of the heavy and light peaks, and the approximate average fragment kinetic energy and width for thermal-neutron induced fission of $^{235}$U. With adjustment of the dissipation strength, the inertia scaling, the radius of the neck at scission, and a random neck rupture distribution, it gives a very good representation of the yields measured. One of the parameters, the inertia scaling, is used to fit the mean fragment TKE. With these model constants fixed, the model predicts very well the neutron-energy dependence of the average TKE for $^{235}$U(n,f), and the energy dependence of the fragment yields. The symmetric yield increases even without invoking any changes in the level-density parameter, the number of events starting out in the symmetric valley, or any postulated weakening of shell structure with excitation energy. Fine details of the mass yields which may reflect detailed fragment structure effects, are missed because of the frozen isospin assumption, which is made to reduce the dimensionality of the model.

With the same model applied to $^{233}$U(n,f), the mass yields and the average TKE are well reproduced. To fit the still relatively uncertain symmetric yield, 40% of trajectories entering the symmetric valley are removed. The incident neutron energy dependence of the TKE is predicted to be significantly different from that for $^{235}$U(n,f). A sufficiently accurate measurement of this observable would provide an important test of the predictive power of this model.

When applied to $^{239}$Pu(n,f), the model with the same parameters as determined for $^{235}$U(n,f) predicts the mean masses of the asymmetric yield peaks and their standard deviations with small errors. However, the model predicts about a factor of 6 too much symmetric yield, and does not reproduce well the large experimental third moment of the yield peak compared to $^{235}$U(n,f). By arbitrarily removing 85% of the trajectories which reach scission in the symmetric valley, a very good reproduction of the prompt yield in the symmetric region is achieved. The fine details of the prompt yield near the maxima are missed to about the same extent as was seen for $^{236}$U. With the model fixed only by considering mass yields, the predicted mean TKE is within 0.4 MeV of the experimental value, and the standard deviation is within 3% of the expermental value. The predicted TKE(A) is again very accurate for fragment masses from 128 to 154. There is a slight overestimation for A = 122 to 127, but much less so than the model predicts for $^{235}$U(n,f) for thermal neutrons. The model deviates more significantly for the very low yields for $A \geq 155$. The predicted neutron energy dependence of <TKE> is linear, but with a slope significantly less than seen in the data. The predicted dependence of the mass yields on neutron energy is inconsistent with the available data, which may have systematic errors [121].

The same model applied to $^{240}$Pu spontaneous fission again finds the mean masses of the heavy and light peaks quite well, with a similar missing of the fine details and extreme skewness of the measured yield peaks. The model, again only adjusted to mass yields by adding a 0.27% admixture of trajectories starting in the symmetric valley, predicts relatively well the difference between the mean TKE for spontaneous fission compared to that for thermal-neutron fission of $^{239}$Pu [125],[128], but it significantly underpredicts the second moment of the TKE distribution. It provides a surprisingly good prediction of the measured TKE(A).

When the same model is applied to the spontaneous fission of $^{252}$Cf, the average mass and the second moments of the asymmetric yield peaks are significantly in error, as is the predicted mean TKE. An arbitrary readjustment of the scission neck radius, the random-neck rupture parameter, and discarding all trajectories which enter the symmetric valley leads to a model which reproduces the mean masses and slightly underestimates their second moments. It is striking that this modified model, arbitrarily changed to fit the prompt and pre-evaporation mass yields, gives essentially the exact

experimental mean TKE, and underestimates the second moment of the TKE by about 15%. The TKE(A) measurements are reasonably well predicted for the mass range 137 to 160, but deviate significantly in both the symmetric region and the very asymmetric range.

### B. Conclusions

A number of general conclusions may be drawn from the systems so far investigated.

There does not appear to be any deep mystery about fission. A straightforward extension of the ideas of Bohr and Wheeler from 1939 [129], the inclusion of shell effects on the nuclear potential energy by means of the procedure developed by Strutinsky [35], and the assumption that fission dynamics is dissipative and essentially classical leads to very good predictions of the average mass split in actinide fission. In addition, there seems to be a surprisingly good prediction of fragment kinetic-energy distributions from a rudimentary model with a universal set of parameters. Of course, many details about yield distributions do reflect the quantum-mechanical nature of the single-particle structure of the nucleus, but only as a perturbation on the dominantly classical dynamical behavior,

An analysis of the macroscopic-microscopic potential-energy surface, and the reproduction of the mass yield over 3 orders of magnitude in some cases show no evidence of more than one independent asymmetric fission mode. Analyses of experimental results have often been performed in terms of two or three independent asymmetric fission modes; for an example see Ref. [114]. However, the need for such extra modes seems to be a result of assuming a gaussian yield distribution from each mode. Since the observed yields are not gaussian, more than one mode is then required. But the model calculations give a very good representation of the shape of the non-gaussian asymmetric yield peaks, starting from a single asymmetric valley in the potential energy, in addition to giving significant details of the TKE distributions which are consistent with the existing measurements. Application of Occam's sRazor would suggest that the analysis of yield and TKE distributions in terms of multiple gaussian functions is not warranted.

These calculations show, somewhat surprisingly, that the results are not very sensitive to the exact value of dissipation strength. This is similar to the conclusions drawn decades ago and outlined in Sec. II E 4. One might have suspected that the more detailed modeling of widths and correlations in a Langevin model might have predicted some details which would lead to a more refined constraint on the strengh of dissipation. I have rather arbitrarily limited consideration of the dissipation strength in the surface-plus-window model to from half of to twice the value deduced in 1985. Over this range, the only quantity observed to depend sensitively on the dissipations strength is the average saddle-to-scission time. The TKE width for $^{235}$U(n,f) decreases slightly with decreasing dissipation strength, with the value for the dissipation strength of 0.5 of the default value still being too large; for $^{252}$Cf(SF), exactly the opposite behavior is seen, but the TKE width prediction remains less than that measured even for dissipation strengths as low as 0.25. of the default value of 0.27. The mean kinetic energy seems to be very well predicted by the value of this scale factor of 0.5 for the four isotopes considered, but similar results could be found for a range of a factor of two in either direction with only a very slight readjustment of the other model parameters from those adopted.

The maximum average temperature of the nucleus at scission is within 10% of 0.4 MeV for all the results presented here. This conclusion does not depend strongly on the assumed strength of dissipation. The average temperature for thermal-neutron-induced fission of $^{235}$U varies only from 0.33 to 0.42 MeV as the dissipation scaling is varied from 0.25 to 1.0. This low temperature at scission would seem to justify post facto the assumption that the zero-temperature potential energy is a good approximation to the free energy. This temperature does not, of course, reflect the excitation energy of the fragments when neutron evaporation occurs, long after the shape dynamical processes have ceased. The excitation energy of the fragments at this late time will contain, besides the excitation at scission, the deformation energy of the fragments at scission, which will have been damped out by the time of neutron emission.

The average dynamical fission (saddle-to-scission) time is in the range of $3–7\times10^{-21}$ s for all the systems studied, including varying the the dissipation scale factor from 0.25 to 1.0. With the 'adjusted-model' dissipation scale of 0.5, all average dynamical fission times are less than $5 \times 10^{-21}$ s.

Despite the success of modeling certain aspects of $^{240}$Pu(SF), the need to change the model scission parameters significantly to reproduce the mass yields of $^{252}$Cf(SF) would suggest that a more sophisticated model of the distribution of exit points after barrier penetration, used as starting points for the dynamical trajectories, would be desirable.

The model seems to give a very good prediction of the dependence of both energy and mass yield observables on incident neutron energy for induced fission, but this conclusion must remain tentative until significantly more fissioning isotopes have been modeled and compared to not-yet-measured data.

Of a more speculative nature, the fact that some of the gross observables seem to be predicted when making small excursions in Z,A space indicate that it might be possible to use a more mature version of this model to predict fission distributions for poorly-measured or nearly-impossible-to-measure minority actinide isotopes. Whether this is feasible will require examining more systems for which reasonable data is available. Since it has already been shown that the potential-energy model predicts differences for different isotopes of the same fission-

ing element [38, 39], this model will capture subtle differences between such isotopes. It is reasonable to think that the correlations among different mass and TKE observables for such systems are better constrained by this type of model than by the usual independent evaluations of different types of observables in existing data evaluations, where such correlations are usually not included.

### C. Future directions

One of the more interesting explorations of the current model would be to examine fission of Th and Ra isotopes, which exhibit a transition to yield distributions where symmetric fission is of a comparable magnitude to asymmetric fission.

Another straightforward but involved calculation would be to implement yield and TKE calculations for higher neutron energies for induced fission. This requires modeling multiple-chance fission. To do this in the context of this model requires considering potential surfaces for the desired element with atomic mass numbers of $A-1, A-2, \ldots, A-n$ for n+1th chance fission and also having a realistic model for the energy dependence of the n-th chance fission cross sections, which cannot be calculated in this model.

It seems clear that the simplest extension of this model would be to modify the post-scission dynamics to include the beyond-macroscopic potential energy of the fragments. Including the extra binding energy of nearly magic fragments should lead to higher TKE being calculated for such systems. This would mitigate the rapid fall-off of the TKE probability distribution at the upper end and the lack of events at higher energies seen in the data. Whether this improvement would lead to a less skewed TKE distribution remains unclear until such an improvement is implemented. In addition to this improvement, it would be feasible to add consideration of the angular momentum of the fragments, which might guide modeling of initial spin distributions for post-scission decay models.

A more difficult extension of the model would be to include the isospin of the nascent fragments. The results of [130, 131] indicate that much of the fine-scale structure in the yield seen in experiments might be much better predicted by including this effect, although it might be difficult for conceptual reasons to implement it in this dynamical treatment.

## VI. ACKNOWLEDGEMENTS

The author wishes to thank Morgan White for advice and support during this research, Jørgen Randrup for discussions of the inertia and dissipation models and for detecting an error in the inertia calculation, J. R. Nix for guidance on Sect. II E, John Lestone for many illuminating discussions and for providing the neutron-evaporation model code needed to create Figures 20 and 35 and all the prompt yield calculations, and Peter Möller, for many discussions over many years, especially for bringing attention to the importance of the Strutinsky smoothing range to the microscopic energy correction for highly-deformed nuclei, and for generously sharing his single-particle energy code, which was essential, and which in modified form was used to calculate all the potential-energy and gradient surfaces used in this work. This work was carried out under the auspices of the National Nuclear Security Administration of the U.S. Department of Energy at Los Alamos National Laboratory (LANL) under Contract No. DE-AC52-06NA25396. A major part of this work was supported by the LANL LDRD Program Office.

[1] O. Hahn and F. Strassmann, Naturwiss. **27** (1939) 11.
[2] L. Meitner and O. R. Frisch, Nature **143** (1939) 239.
[3] A. Einstein, Ann. Phys. **17** (1905) 549.
[4] H. A. Kramers, Physica **7** (1940) 284.
[5] J. R. Nix and W. J. Swiatecki, Nucl. Phys. **71** (1965) 1.
[6] R. W. Hasse, Phys. Lett. B **27B** (1968) 605.
[7] J. R. Nix, Nucl. Phys. **A130** (1969) 241.
[8] K. T. R. Davies, A. J. Sierk, and J. R. Nix, Phys. Rev. C **13** (1969) 2385.
[9] J. Blocki, Y. Boneh, J. R. Nix, J. Randrup, M. Robel, A. J. Sierk and W. J. Swiatecki, Ann. Phys. (N. Y.) **113** (1978) 330.
[10] P. Grangé, H. C. Pauli, and H. A. Weidenmüller, Phys. Lett. B **88B** (1979) 9.
[11] P. Grangé and H. A. Weidenmüller, Phys. Lett. B **96B** (1980) 26.
[12] K. Pomorski and H. Hofmann, J. Physique **62** (1981) 381.
[13] H. Hofmann and J. R. Nix, Phys. Lett. B **122B** (1983) 117.
[14] F. Scheuter, C. Grégoire, H. Hofmann and J. R. Nix, Phys. Lett. B **149B** (1984) 303.
[15] J. R. Nix, A. J. Sierk, H. Hofmann, F. Scheuter, and D. Vautherin, Nucl. Phys. **A424** (1984) 239.
[16] S. Chandrasekhar, Rev. Mod. Phys. **15** (1943) 1.
[17] H. Feldmeier and H. Spangenberger, Nucl. Phys. **A435** (1985) 229.
[18] R. Donangelo and L. F. Canto, Nucl. Phys. **A451** (1986) 349.
[19] G. D. Adeev, I. I. Gontchar, and L. A. Marchenko, Yad. Fiz. **42** (1985) 42.
[20] P. Fröbrich and J. Marten, Z. Phys. A **339** (1991) 171.
[21] H. Feldmeier, Rep. Prog. Phys. **50** (1987) 915.
[22] Y. Abe, S. Ayik, P.-G. Reinhard, and E. Suraud, Phys Rep. **275** (1996) 49.
[23] P. Fröbrich and L. I. Gontchar, Phys. Rep. **292** (1998) 131.
[24] I. I. Gontchar, G. I. Kosenko, N. I. Pischasov, and O. J. Serdyuk, Yad. Fiz. **55** (1992) 920; translated in Sov. J. Nucl. Phys. **55** (1992) 514.
[25] G.-R. Tillack, Phys. Lett. B **278** (1992) 403.
[26] T. Wada, N. Carjan, and Y. Abe, Nucl. Phys. **A538** (1992) 283c.
[27] P. N. Nadtochy, A. V. Karpov, D. V. Vanin, and G. D. Adeev, Yad. Fiz. **64** (2001) 926; translated in Phys. At. Nucl. **64** (2001) 864.
[28] A. V. Karpov, P. N. Nadtochy, D. V. Vanin, and G. D. Adeev, Phys. Rev. C **63** (2001) 054610.
[29] T. Ichikawa, T. Asano, T. Wada, and M. Ohta, J. Nucl. Radiochem. Sci. **3** (2002) 67.
[30] P. N. Nadtochy, E. G. Ryabov, A. E. Gegechkori, Yu. A. Anischenko, and G. D. Adeev, Phys. Rev. C **85** (2012) 064619.
[31] Y. Aritomo and S. Chiba, Phys. Rev. C **88** (2013) 044614.
[32] Y. Aritomo, S. Chiba, and F. Ivanyuk, Phys. Rev. C **90** (2014) 054609.
[33] S. Goriely, M. Samyn, P.-H. Heenen, J. M. Pearson, and F. Tondeur, Phys. Rev. C **66** (2002) 024326.
[34] P. Möller, J. R. Nix, W. D. Myers, and W. J. Swiatecki, At. Data Nucl. Data Tables **59** (1995) 185.
[35] V. M. Strutinsky, Nucl. Phys. **A95** (1967) 420.
[36] P. Möller, A. J. Sierk, R. Bengtssson, H. Sagawa, and T. Ichikawa, At. Data and Nucl. Data Tables, **98** (2012) 149.
[37] P. Möller, A. J. Sierk, T. Ichikawa, and H. Sagawa, At. Data Nucl. Data Tables **109–110** (2016) 1.
[38] P. Möller, D. G. Madland, A. J. Sierk, and A. Iwamoto, Nature **409** (2001) 785.
[39] P. Möller, A. J. Sierk, T. Ichikawa, A. Iwamoto, R. Bengtsson, H. Uhrenholt, and S. Åberg, Phys. Rev. C **79** (2009) 064304.
[40] P. Möller, A. J. Sierk, T. Ichikawa, A. Iwamoto, and M. Mumpower, Phys. Rev. C **91** (2015) 024310.
[41] M. Kowal, P. Jachimowicz, and A. Sobiczewski, Phys. Rev. C **82** (2010) 014303.
[42] G. D. Adeev, A. V. Karpov, P. N. Nadtochy, and D. V. Vanin, Phys. Part. Nuclei **36** (2005) 378.
[43] P. N. Nadtochy, A. Kelíc, and K.-H. Schmidt, Phys. Rev. C **75** (2007) 064614.
[44] A. J. Sierk and J. R. Nix, Phys. Rev. C **21** (1980) 982.
[45] J. R. Nix and A. J. Sierk, *Proc. Intl. Symp. on Perspectives in Nucl. Phys., Madras, India, 1987*, J. Madras Univ. **B50** (1987) 38.
[46] P. Möller and A. Iwamoto, Phys. Rev. C **61** (2000) 047602.
[47] P. Möller, A. J. Sierk, and A. Iwamoto, Phys. Rev. Lett. **92** (2004) 072501.
[48] J. Randrup, P. Möller, and A. J. Sierk, Phys. Rev. C **84** (2011) 034613.
[49] P. Jachimowicz, M. Kowal, and J. Skalski, Phys. Rev. C **85** (2012) 034305.
[50] S. Trentalange, S. E. Koonin, and A. J. Sierk, Phys. Rev. C **22** (1980) 1159.
[51] A. J. Sierk, Phys. Rev. C **33** (1986) 2039.
[52] J. R. Nix, University of California Radiation Laboratory Report UCRL-17958 (1968), (unpublished).
[53] S. G. Nilsson, Kgl. Danske Videnskab. Selskab. Mat.-Fys. Medd. **29**:No. 16 (1955).
[54] S. G. Nilsson, C. F. Tsang, A. Sobiczewski, Z. Szymański, S. Wycech, C. Gustafson, I.-L. Lamm, P. Möller, and B. Nilsson, Nucl. Phys. **A131** (1969) 1.
[55] W. M. Howard and P. Möller, At. Data Nucl. Data Tables **25** (1980) 219.
[56] C. deBoor, A Practical Guide to Splines, (Springer-Verlag New York, 1978).
[57] C. deBoor, ACM Trans. Math. Software **5** (1979) 173.
[58] A. Mamdouh, J. M. Pearson, M. Rayet, and F. Tondeur, Nucl. Phys. **A644** (1998) 389.
[59] B. Hayes, Am. Sci. **88** (2000) 481.
[60] T. Ichikawa, A. Iwamoto, P. Möller, and A. J. Sierk, Phys. Rev. C, **86** (2012) 024610.
[61] L. Wilets, Theories of nuclear fission (Clarendon Press, Oxford, 1964).
[62] P. Möller, S. G. Nilsson, and J. R. Nix, Nucl. Phys. **A229** (1974) 292.
[63] I. Kelson, Phys. Rev. **136** (1964) B1667.
[64] K. Bao, Y. Zhuo, and X. Wu, Z. Phys. A **352** (1995) 321.
[65] G. Chaudhuri and S. Pal, Phys. Rev. C **63** (2001) 064603.

[66] H. Lamb, *Hydrodynamics*,, 6th ed. (Cambridge University Press, Cambridge 1932), pp. 579–581.
[67] J. R. Nix and A. J. Sierk, Nucl. Phys. **A428** (1984) 161c.
[68] J. R. Nix and A. J. Sierk, Phys. Rev. C **21** (1980) 396.
[69] J. R. Nix and A. J. Sierk, Phys. Rev. C **25** (1982) 1068.
[70] S. E. Koonin and J. Randrup, Nucl. Phys. **A289** (1977) 475.
[71] C. Yannouleas, Nucl. Phys. **A439** (1985) 336.
[72] J. J. Griffin and M. Dworzecka, Nucl. Phys. **A455** (1986) 61.
[73] R. W. Hasse and P. Schuck, Nucl. Phys. **A438** (1985) 157.
[74] W. J. Swiatecki, Prog. Part. Nucl. Phys. **4** (1980) 383.
[75] J. R. Nix, D. G. Madland, and A. J. Sierk, *Proc. Intl. Conf. on Nucl. Data for Basic and Applied Science, Santa Fe, New Mexico, 1985*, Radiation Effects **92** (1986) 263.
[76] J. R. Nix and A. J. Sierk, *Proc. Winter Workshop on Nuclear Dynamics IV, Copper Mountain, Colorado, 1986*, National Technical Information Service Report No. CONF-860270 (1986) 1.
[77] J. R. Nix and A. J. Sierk, *Proc. Intl. School-Seminar on Heavy Ion Physics, Dubna, USSR, 1986*, Joint Institute for Nuclear Research Report No. JINR-D7-87-68 (1987) 453.
[78] J. R. Nix and A. J. Sierk, *Proc. 6th Adriatic Intl. Conf. on Nuclear Physics: Frontiers of Heavy-Ion Physics, Dubrovnik, Yugoslavia, 1987*, (World Scientific, Singapore, 1987) 333.
[79] G. D. Adeev and V. V. Pashkevich, Nucl Phys. **A502** (1989) 405c.
[80] D. V. Vanin, P. N. Nadtochy, G. I. Kosenko, and G. D. Adeev, Yad. Fiz. **63** (2000) 1957; Phys. At. Nucl. **63** (2000) 1865.
[81] I. Gontchar, M. Morjean, and S. Basnary, Europhys. Lett. **57** (2002) 355.
[82] F. E. Bertrand, Nucl. Phys. **A354** (1981) 129c.
[83] F. E. Bertrand, private communication (1985).
[84] V. E. Viola, K. Kwiatkowski, and M. Walker, Phys. Rev. C **31** (1985) 1550.
[85] P. Paul and M. Thoennessen, Annu. Rev. Nucl. Part. Sci. **44** (1994) 65.
[86] I. Dioszegi, N. P. Shaw, I. Mazumdar, A. Hatzikoutelis, and P. Paul, Phys. Rev. C **61** (2000) 024613.
[87] B. B. Back, D. J. Blumenthal, C. N. Davids, D. J. Henderson, R. Hermann, D. J. Hofman, C. L. Jiang, H. T. Penttila, and A. H. Wuosmaa, Phys. Rev. C **60** (1999) 044602.
[88] J. P. Lestone and S. G. McCalla, Phys. Rev. C **79** (2009) 044611.
[89] V. E. Viola, Jr. and T. Sikkeland, Phys. Rev. **130** (1963) 244.
[90] V. E. Viola, Jr., Nucl. Data **A1** (1966) 391.
[91] T. Sikkeland, Phys. Lett. **27B** (1968) 277; misprint: the experimental kinetic energy should be 225±4 MeV rather than 255±4 MeV.
[92] K. Grotowski, Z. Majka, R. Płaneta, M. Szczodrak, Y. Chan, G. Guarino, L. G. Moretto, D. J. Morrissey, L. G. Sobotka, R. G. Stokstad, I. Tserruya, S. Wald, and G. J. Wozniak, Phys. Rev. C, **30** (1984) 1214.
[93] J. Toke, R. Bock, G. X. Dai, A. Gobbi, S. Gralla, K. D. Hildenbrand, I. Kuzminski, W. F. J. Müller, A. Olmi, and H. Stelzer, Nucl. Phys. **A440** (1985) 327.
[94] D. v. Harrach, P. Glässel, Y. Civelekoğlu, R. Männer, H. J. Specht, J. B. Wilhelmy, H. Freisleben, and K. D. Hildenbrand, *Proc. Fourth IAEA Symp. Phys. Chem. of Fission, Jülich, 1979*, (International Atomic Energy Agency, Vienna, 1980), 575.
[95] B. Borderie, F. Hanappe, C. Ngô, J. Péter, and B. Tamain, Nucl. Phys. **A220** (1974) 93.
[96] J. Galin, M. Lefort, J. Péter, X. Tarrago, E. Cheifetz, and Z. Fraenkel, Nucl. Phys. **134** (1969) 513.
[97] H. C. Britt, H. E. Wegner, and J. C. Gursky, Phys. Rev. **120** (1963) 2239.
[98] F. Plasil, D. E. Burnett, H. C. Britt, and S. G. Thompson, Phys. Rev˙**142** (1966) 696.
[99] M. N. Namboodiri, J. B. Natowitz, E. T. Chulik, K. Das, and L. Webb, Nucl. Phys. **A252** (1975) 163.
[100] D. S. Burnett, Lawrence Berekeley Laboratory Report UCRL-11006 (1963) (unpublished).
[101] C. Cabot, C. Ngô, J. Péter, and B. Tamain, Nucl. Phys. **A244** (1975) 134.
[102] J. A. Zonneveld, *Automatic Numerical Integration*, Mathematical Center Tract No. 8 (Mathematisch Centrum, Amsterdam, 1964), 23.
[103] K. T. R. Davies, J. R. Nix, and A. J. Sierk, Phys. Rev. C **28** (1983) 1181.
[104] J. Randrup and P. Möller, Phys. Rev. Lett. **106** (2011) 132503.
[105] P. Möller, J. R. Nix, and W. J. Swiatecki, Nucl. Phys. **A469** (1987) 1.
[106] P. Möller, J. R. Nix, and W. J. Swiatecki, Nucl. Phys. **A492** (1989) 349.
[107] A. Sicre, G. Barreau, A. Boukellal, F. Caïtucoli, T. P. Doan, B. Leroux, P. Geltenbort, F. Gönnenwein, A. Oed, and M. Asghar, Radiation Effects **93:1–4** (1986) 65.
[108] K. Meierbachtol, F. Tovesson, D. Shields, C. Arnold, R. Blakeley, T. Bredeweg, M. Devlin, A. A. Hecht, L. E. Heffern, J. Jorgenson, A. Laptev, D. Mader, J. M. O'Donnell, A. J. Sierk, and M. White, Nucl. Inst. Meth. A **788** (2015) 59.
[109] E. Konecny, H. J. Specht, and J. Weber, *Proc. Third IAEA Symp. Phys. Chem. Fission Vol. II*, (International Atomic Energy Agency, Vienna, 1974), 3.
[110] U. Brosa and S. Grossmann, J. Phys. G **10** (1984) 933.
[111] U. Brosa, S. Grossmann, and A. Müller, Phys. Rep˙**197** (1990) 167.
[112] I. Stetcu, P. Talou, T. Kawano, and M. Jandel, Phys. Rev. C **88** (2013) 044603.
[113] R. Capote, Y.-J. Chen,, F.-J. Hambsch, N. V. Kornilov, J. P. Lestone, O. Litaize, B. Morillon, D. Neudecker, S. Oberstedt, T. Ohsawa, N. Otuka, V. G. Pronyaev, A. Saxena, O. Serot, O. A. Shcherbakov, N.-C. Shu, D. L. Smith, P. Talou, A. Trkov, A. C. Tudora, R. Vogt, and A. S. Vorobyev, Nucl. Data Sheets **131** (2016) 1; P. Talou (private communication).
[114] Ch. Straede, C. Budtz-Jorgensen, and H.-H. Knitter, Nucl. Phys. **A462** (1987) 85.
[115] T. R. England and B. F. Rider, LANL Report LA-UR-94-3106 (unpublished).
[116] J. P. Lestone, Nucl. Data Sheets **131** (2016) 357.
[117] D. G. Madland, Nucl. Phys. **A772** (2006) 113.
[118] J. W. Meadows and C. Budtz-Jorgensen, Argonne National Laboratory report ANL/NDM-64, (1982) (unpublished).

[119] J. P. Lestone and T. T. Strother, Nucl. Data Sheets **118** (2014) 118.
[120] D. Duke, PhD Thesis, Colorado School of Mines, Nov. 2015; LANL Report LA-UR-15-28829 (unpublished).
[121] M. E. Gooden, C. W. Arnold, J. A. Becker, C. Bhatia, M. Bhike, E. M. Bond, T. A. Bredeweg, B. Fallin, M. M. Fowler, C. R. Howell, J. H. Kelley, Krishichayan, R. Macri, G. Rusev, C. Ryan, S. A. Sheets, M. A. Stoyer, A. P. Tonchev, W. Tornow, D. J. Vieira, and J. B. Wilhelmy, Nucl. Data Sheets, **131** (2016) 319.
[122] V. Surin, et al., Sov. Jour. Nucl. Phys. **14** (1972) 523OR 40112.
[123] H. Baba,, T. Saito,, N. Takahashi,, A. Yokoyama, T. Miyauchi, S. Mori, D. Yano, T. Hakoda, K. Takamiya, K. Nakanishi, and Y. Nakagome, Jour. Nucl. Sci. Tech. **34** (1997) 871.
[124] M. Asghar, F. Caïtucoli, B. Leroux, P. Perrin, and G. Barreau, Nucl. Phys. **A368** (1981) 328.
[125] C. Wagemans, E. Allaert, A. Deruytter, R. Barthélémy, and P. Schillebeeckx, Phys. Rev. C **30** (1984) 218.
[126] N. I. Akimov, et al., Sov. J. Nucl. Phys. **13** (1971) 272.
[127] L. Dematté, C. Wagemans, R. Barthélémy, P. D'Hondt, and A. Deruytter, Nucl. Phys. **A617** (1997) 331.
[128] P. Schillebeeckx, C. Wagemans, A. J. Deruytter, and R. Barthélémy, Nucl. Phys. **A545** (1992) 623.
[129] N. Bohr and J. A. Wheeler, Phys. Rev. **56** (1939) 426.
[130] P. Möller and T. Ichikawao, Eur. Phys. J. A **51** (2015) 173.
[131] P. Möller and C. Schmitt, Eur. Phys. J. A **53**:7 (2017).